Development and Testing of a Hot Stamped Axial Crush Member with Tailored Properties

by

Kaab Omer

A thesis

presented to the University of Waterloo

in fulfillment of the

thesis requirement for the degree of

Master of Applied Science

in

Mechanical Engineering

I hereby declare that I am the sole author of this thesis. This is a true copy of the thesis, including any required final revisions, as accepted by my examiners.

I understand that my thesis may be made electronically available to the public.

Abstract

This thesis investigates the effect of tailoring the properties of a hot stamped axial crush rail consisting of a top hat cross-section on its crash response. The tailored hot stamping (THS) process is considered, in which the forming tool is partitioned into zones that are either cooled or heated. The local die temperature controls the quench rate within the part, such that the formed part will have zones of differing hardness (strength) and ductility levels.

In the current work, four configurations of THS rails were formed: a non-tailored configuration using conventional room temperature tooling and three tailored configurations in which one-half of the rail was quenched while the other half was formed in tooling that was heated at different temperatures (in the range 400-700˚C). Micro-hardness measurements confirmed that THS can be used to form an axial crush member that contains tailored properties along its length. The as-formed parts exhibited a Vickers hardness of ~475 HV in zones formed in cooled tooling, ~280 HV in zones formed in tooling that was heated to 400˚C and ~215 HV in zones that were formed when the die set was heated to 700˚C.

The formed parts were then welded in pairs along their flanges and axially crushed under dynamic and quasi-static conditions. The non-tailored, fully hardened components did absorb the highest energy (25.8 kJ), but exhibited extensive tearing and fracture. The force-displacement and energy absorption curves from the crush experiments showed that the tailored configurations absorbed less energy (21.6-25.7 kJ), but were less susceptible to buckling and had excellent repeatability in its crash response. Tailored regions with higher temperature tooling and/or graded tooling temperature distributions exhibited the least damage and absorbed the highest energy amongst the tailored configurations.

Numerical models of the THS process and subsequent crash response were developed using the Åkerström material model in LS-Dyna to model the forming and the constitutive models of Bardelcik et al. to simulate the crash behavior. The predicted micro-hardness distributions in the components with bainite or martensite as-formed phases were very accurate (usually within 10%), whereas predictions for ferrite-containing components were within 15% of the measured

hardness. The crash models were able to accurately predict the energy absorption of rails that were formed in cooled and 400˚C tooling. They were less accurate for dynamic crush of rails that contained ferrite.

Overall, tailoring was found to have a positive effect on the energy absorption of a hot stamped axial crush member. Future work should focus on improving the hot stamping and crash models so they can accurately account for the effect of ferrite. Furthermore, a non-axial, angled offset crush should also be performed to more thoroughly investigate the effects of tailoring.

Acknowledgements

Bismillahi-irrahman-irraheem (In the name of God, the most gracious, the most merciful)

I would like to begin by expressing my gratitude and thanking my supervisor, Dr. Michael Worswick, for giving me the excellent opportunity of working on this project and for providing me with support and guidance throughout.

I would also like to thank the following people for helping me throughout this project: Eckhard Budziarek, Jeff Wemp, Alexander Bardelcik, Ryan George, José Imbert and Cliff Butcher.

My expression of gratitude also goes to the following people for all the fun times that we have had: Luke ten Kortenaar, Yonathan Prajogo and Chris Kohar.

Support for this research from Honda R&D Americas, Promatek Research Center (Cosma International), ArcelorMittal, Automotive Partnership Canada, the Natural Sciences and Engineering Research Council, the Ontario Research Fund and the Canada Research Chair Secretariat is also gratefully acknowledged.

Finally, I would like to thank my parents and grandmothers for all the words of encouragement that they have provided. I would also like to thank my sisters for all the words of "discouragement" that they have provided ☺.

Table of Contents

List of Figures

List of Tables

List of Equations

1. Background

The current trend in the automotive industry to move towards lightweight materials has resulted in the development of several new fabrication processes. One such process is hot stamping, where a blank made of Boron steel is heated to a temperature high enough to austenize it. The blank is then fed into a cooled die set where it is formed and quenched. The quenching stage of this process results in a high rate of cooling in the blank, which in turn yields a phase transformation [1] from austenite to martensite. The martensitic microstructure in the formed blank exhibits tensile strengths as high as 1500 MPa. These high tensile strengths mean that the overall weight of the vehicle can be reduced because less material is needed to achieve a similar or higher amount of strength than conventional mild steels.

The martensitic microstructure in the formed part is, however, very brittle. This is not favourable for the front and rear rails in an automobile, which are expected to absorb large amounts of energy and undergo large deformation in frontal or rear crash events. Therefore, a more ductile microstructure in the formed part is preferred for these parts. To achieve a more ductile microstructure, a variant of the hot stamping process, known as tailored hot stamping (THS), was developed. In this process heaters are inserted into the die set, allowing for a slower rate of cooling of the blank, which in turn leads to a bainitic and/or ferritic microstructure in the formed blank [1]. The bainitic and/or ferritic microstructures do not exhibit as high a tensile strength as their martensitic counterpart [2], however, they do exhibit better ductility [3, 4, 5] and are still stronger than conventional mild steel, for example.

The THS process can be used to tailor the tensile properties of an axial crush member to optimize its crash performance. The purpose of the current research is to investigate the effects of forming an axial crush member using THS, by creating a component with distinct martensitic and bainitic/ferritic zone along the length of the part. Parts were formed at different tooling temperatures and subjected to impact testing over a range of impact velocities. Furthermore, the forming and impact processes were modelled using non-linear finite element analysis to ascertain the predictive capability of current simulation techniques.

1.1 Tailoring Techniques

There are several available techniques that can be used to tailor the strength distribution within a hot stamped component. Tailor-welding of blanks is one such technique in which blanks of different tensile strength, and possibly different thickness, are welded together prior to being formed [6, 7, 8, 9]. Advantages of this technique are the ability to optimize the weight of a component by varying its thickness in different regions in addition to its tensile strength. Disadvantages include the added welding cost.

Another possible technique for tailoring the properties of a part is post tempering, where a component is hot stamped to achieve a uniform fully martensitic condition after which selected regions of the component are heat treated (tempered) to tailor the property distribution [10]. This approach simplifies the forming process but adds an additional expense during the post-tempering phase.

Another technique that can be employed to tailor the properties of a part is the THS process, the focus of the current research. In the THS process, the tensile properties of the part are tailored *during* the forming process, rather than before or after it.

1.2 The Tailored Hot Stamping (THS) Process

As mentioned previously, THS involves austenizing the blank prior to the forming process. This is usually done by placing the blank in an induction oven [11]. The austenized blank is then transferred from the heated environment into the die set which is also heated, either entirely or only in certain areas. The blank is formed and then quenched in this heated die set. Figure 1 outlines the entire THS process.

The resulting properties in the formed blank are controlled by its rate of cooling. The rate of cooling will determine into which phases the austenite phase decomposes [2, 12, 13] and the resulting final hardness properties of the formed part [14, 15]. A Continuous Cooling Temperature (CCT) diagram is typically used to characterize the relationship between cooling rate and resulting microstructures. An example of a CCT diagram for Boron steel can be seen in Figure 2.

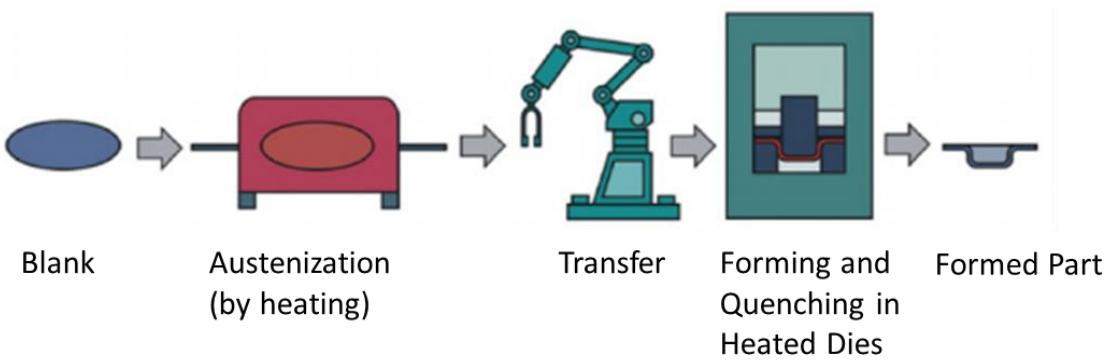

Figure 1. Schematic of the THS process, adapted from **[1]**

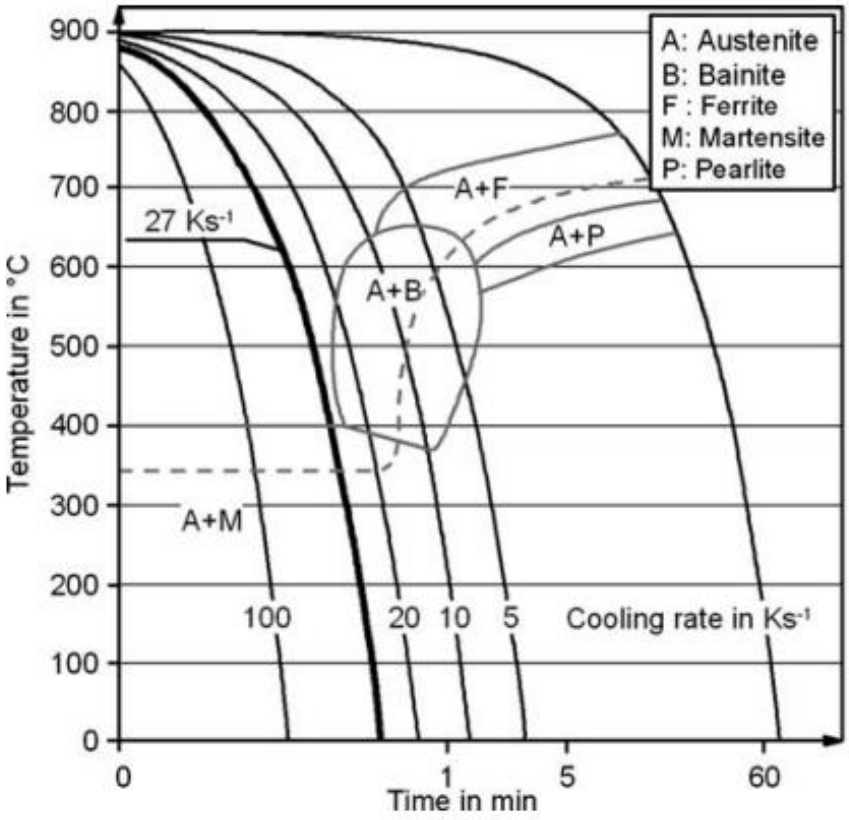

Figure 2. A CCT diagram of 22MnB5 Boron steel, adapted from **[16]**

As is evident from Figure 2, in order to control the final microstructure in the formed blank during THS, and thereby control its hardness, the cooling rate during forming and quenching must be adequately controlled. If softer and more ductile properties are required in a certain region of the formed blank, then a low rate of cooling is required. This is achieved through heating the corresponding section of the die set to a high temperature. Likewise, if a certain

region in the blank is required to be harder, then a high rate of cooling is needed. As such, the corresponding zone in the die set should either be heated to a lower temperature or not heated at all, depending on the desired properties. In many cases, a coolant is pumped through certain areas of the tooling to keep them at room temperature [17].

Various studies have been conducted on the advantages of THS over standard hot stamping. For example, it has been shown that forming and quenching blanks in heated tooling can reduce the springback of the formed part [18, 19, 20, 21]. Also, even though Boron steel generally exhibits good formability in standard hot stamping [22, 23, 24], the THS yields even better formability [25]. Stöhr et al. [13] have shown that if soft properties are desired across an entire part, only partial austenization of the blank is required before forming. However, it is very difficult to produce a martensitic zone using this technique.

Studies have also been conducted on the ability of THS to create a part with a variable hardness profile. In one instance, a B-pillar was tailored in tooling that was heated up to ~200°C by Erhardt and Böke [19] such that it contained a soft zone, a hard zone and a transition zone across its area, as depicted in Figure 3. The hard zone displayed a tensile strength of 1500 MPa (~450 HV) and the soft zone displayed a tensile strength of 600 MPa (~200 HV). Similar studies on a tailored B-pillar were done by Banik et al. [26] and Wilsius et al. [27]. In another work, by George et al. [28], a lab-scale B-pillar was tailored in tooling heated up to various temperatures ranging from 100° - 400°C. In the most extreme case (400°C) in, the Vickers hardness in the B-pillar dropped from ~460 HV in its hard zone to ~240 HV in its soft zone.

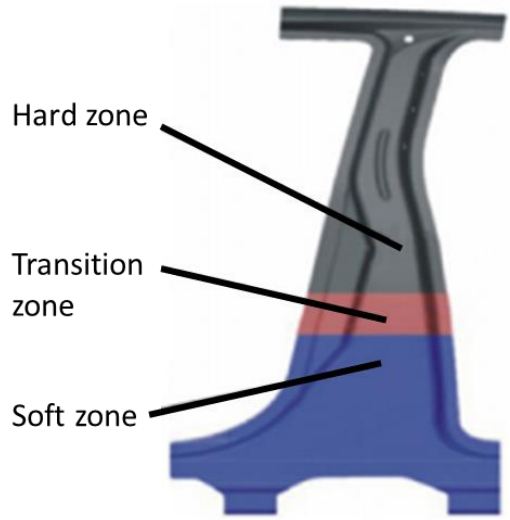

Figure 3. The hard, soft and transition zones in a tailored B-pillar, adapted from **[19]**

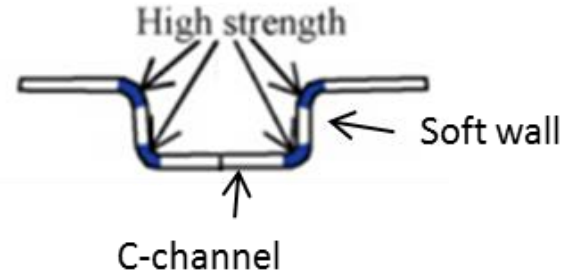

Figure 4. Top hat with hard radii and soft walls and C-channel, adapted from **[2]**

Mori and Okuda [2] have shown that a top hat shaped part with soft walls and C-channel and hard radii (shown in Figure 4) can be produced by adding insulation at certain points in a heated die. In a similar geometric configuration, Berglund et al. [29] formed a hat shaped part (which is pictured in Figure 5) with a soft zone at its centre.

More recently, Eller et al. [30] tailored a 500 mm long hat-shaped component into two zones along its length. This was accomplished by partitioning the tooling into two sets, with an air gap of 1.4 mm in between. One set of the tooling was held at 30°C by pumping chilled water through it, while the other set was heated to 530°C using cartridge heaters, as shown in Figure 6. The 30°C zone in the 1.5 mm thick blank achieved a hardness of 465 HV and the 530°C zone achieved 250 HV. The transition zone between the soft and hard zones was approximately 150 mm wide. The technique of partitioning the tooling used by Eller et al. was very similar to the

technique employed in the work described in this thesis and has already been documented by the author in [31, 32].

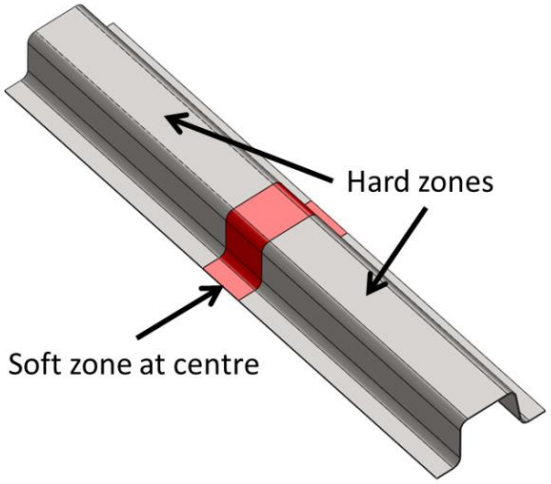

Figure 5. Hat shaped section with a soft zone at its centre, as found in **[29]**

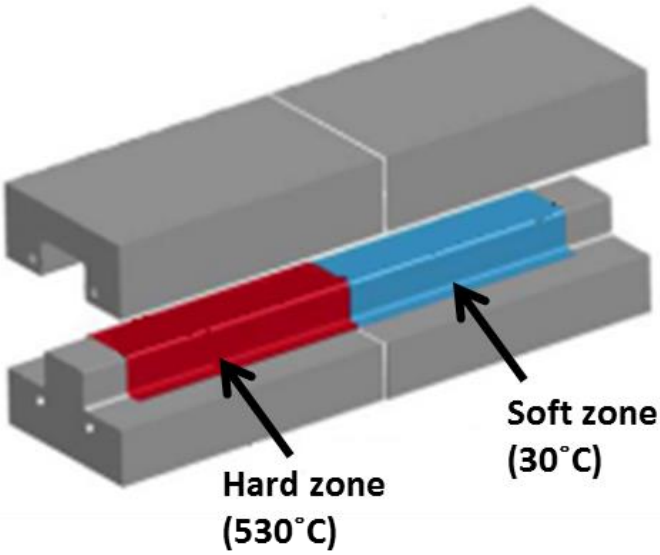

Figure 6. Axially tailored top hat, adapted from **[30]**

The aforementioned examples show that THS offers many advantages over the standard form of hot stamping, such as better ductility. They also show that it is possible to produce a part with tailored properties, which can be used to improve energy absorption in selected regions of the formed blank.

1.3 Crash Performance of Tailored Parts

There are several ways of evaluating crash performance of tailored hot stamped parts: overall energy absorption, peak-to-average load ratio and also the pattern of deformation in a part.

Eller et al. [30] performed a quasi-static 4-point bending test on the tailored top hat section (which was pictured in Figure 6) which they formed at 30˚C/530˚C (as explained in section 1.2). A backing plate was spot-welded to the top hat along its flanges with a weld spacing of 50 mm. The part was supported on two pillars, while two punches (attached to the same block) were used to impact the part: one punch on the soft zone and the other on the hard zone. The impact speed for this test was 20 mm/min. The part was able to sustain a load of 46 kN and a displacement of 17 mm before the initiation of a crack along the fillets between the flange and wall and between the C-channel and wall. The cracks formed in the hard portion of the part.

A 3-point bend test was conducted by Sato et al. [33] on several types of steels, including fully martensitic steels. The tests were done on a top hat section with a backing plate spot-welded along its flanges. A high peak load (140 kN) was achieved for the fully martensitic samples. However, the formation of cracks as well as local buckling was observed.

The focus of Sato et al. [33] was to compare the crash response of several different types of top hat-shaped steels. Likewise, the focus of Eller at al. [30] was to model the failure and plastic deformation of Boron steel. As such, no comparative study was done in either of these works between the crashworthiness of tailored and non-tailored parts, nor between the crashworthiness of blanks formed at different temperatures.

Finite element (FE) models have shown that tailored hot stamped components tend to absorb more energy and have better overall crash characteristics for certain applications than non-tailored and non-hot stamped components. FE models by both Benteler [34] and Bardelcik et al. [35] have shown that a hot stamped B-pillar exhibits lower side impact intrusion than a B-pillar made out of as-received Usibor® 1500P [36, 37]. A similar conclusion can be drawn by comparing the results from [36, 37] for the overall intrusion of a side impact beam made from as

received Usibor®1500 with the results from [32], which looked at the intrusion of a hot stamped side impact beam.

FE models by Benteler have shown that tailoring a B-pillar in a manner similar to what was shown in Figure 3, and then impacting it reduces its total side intrusion in comparison to mild steel and also increases its energy absorption [34]. Most of the deformation was concentrated in the soft zone, which would be the section placed away from the passenger in an automobile. The hard zone in close proximity to the passenger remained straight and intact, as pictured in Figure 7. A similar result was obtained by Wilsius et al. [27]. Bardelcik et al. [35] showed through FE models that impacting a tailored B-pillar reduces its energy absorption by approximately 6.7% when compared with a fully hardened B-pillar. However, the increased ductility in the soft regions did offer advantages in terms of the shape of deformation.

All the experimental and numerical studies mentioned in this section up till now have focused on side impact and intrusion resistance of hot stamped components with tailored properties, such as side impact beams. A numerical study on axial crush was conducted by Ma et al. [38] where they simulated the dynamic crash of a top hat section welded onto a backing plate. A 180 mm long specimen was used in all cases, and it was modelled using two materials (which they designated as matA and matB) in varying proportions along its length (Figure 8). The impact velocity used was 10 m/s and the part that absorbed the maximum amount of energy (9.8 kJ) was tailored along its length where matA spanned 135 mm and matB spanned the remaining 45 mm. The amount of energy absorbed by this part was a lot higher that the non-tailored part made entirely of matB (6.2 kJ) and slightly higher than the part made entirely of matA (9.3 kJ). No experimental validation was provided.

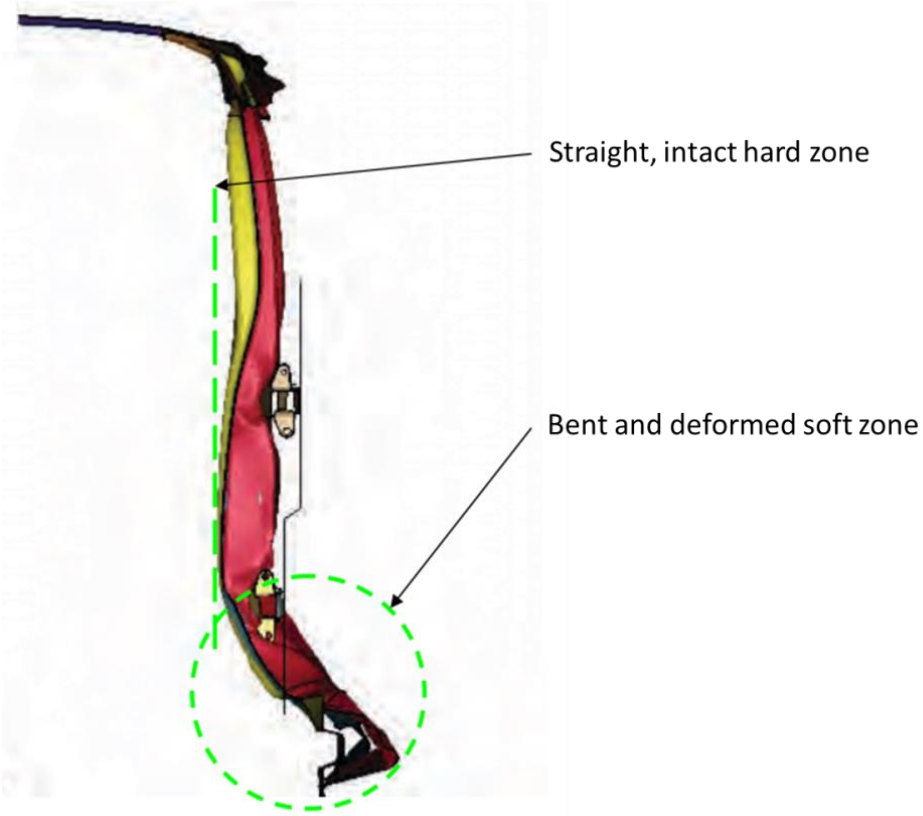

Figure 7. Final deformed shape of a tailored B-pillar, adapted from **[34]**

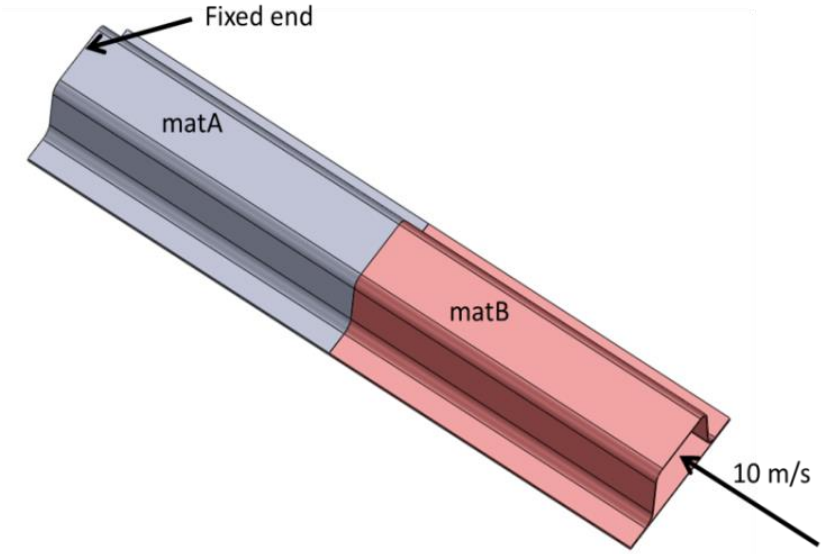

Figure 8. Numerical model setup in **[38]**

To-date, no combined experimental/numerical study has been published on the axial crush performance of hot stamped components (other than publications by the author of this thesis [32,

31]). The loads experienced during an axial crush [39, 40, 41] tend to be significantly higher than those experienced during side impact [42]. Given the brittle characteristics of martensite, hot stamped parts with significant portions of martensite present in them will most likely fracture in the event of an axial crush due to the large plastic strains occurring in fold regions and the limited ductility of martensite. This lack of prior research provides justification for the current research which investigates the viability of a tailored hot stamped axial crush member.

1.4 Numerical Modelling of the THS Process

Modelling the hot stamping process involves two aspects. The first aspect is the simulation of the THS process itself, which includes the tooling, heat transfer, contact as well as boundary conditions. The second aspect is the behavior of the blank during the process, which includes plastic deformation, blank temperature and the resulting properties of the blank.

For modelling the characteristics of the process itself, a coupled thermo-mechanical approach is usually employed [27, 32, 43-49]. A non-coupled approach is possible if computing resources are a concern, however such an approach does lose accuracy [43, 44]. The hot stamping tooling is usually modelled using rigid, non-deformable shell [45] or brick elements [32, 46].

Proper modelling of the heat transfer between the blank and tooling and between different zones of the tooling in THS is also very crucial. The rate of heat transfer between the blank and tooling and between different zones in the tooling depends on the heat transfer coefficient (HTC). For heat transfer between the tooling and blank, where the two metal surfaces are in contact, the contact pressure is the governing factor in determining the HTC [47, 48, 49]. The HTC can be inferred from experimental results using inverse analysis as was done by Salomonsson et al. [50] Salomonsson and Oldenburg [51], Svec and Merklein [14], Caron et al. [49, 52], or by using theoretical formulas [53, 54]. Of these investigators, Caron et al. [49, 52] specifically looked at how the HTC between the tooling and blank is affected by tooling temperatures during THS.

George et al. [28] used experimental values for the HTC between tooling and blank obtained from Oldenburg and Lindkvist [48] to model the hot stamping of a lab-scale B-pillar. George et

al. found, however, that their models were overestimating the Vickers hardness in the B-pillar and so they modified the experimental values found in [48] to the ones shown in Table 1.

For heat transfer between different zones in the tooling, the value of the HTC depends on the distance between two surfaces [47, 55] and the thermal conductivity of the fluid (usually air) between the zones. Heat between different zones is transferred through conduction via the fluid medium present between them (such as air).

Table 1. HTC values used in [28]

Contact Pressure between Tooling and Blank (MPa)	Heat Transfer Coefficient (W/m^2K)
0	400
5	900
10	1000
20	2200

The coefficient of friction is another important parameter when modelling THS, particularly in the surface-to-surface contact between the tooling and the blank. Yanagida and Azushima [21] conducted a study on evaluating the coefficient of friction for Boron steel. They found that under dry conditions, the coefficient of friction approach 0.6 when the blank was pre-heated to a temperature of 800˚C. When the blank was lubricated, the coefficient of friction reduced to 0.3-0.4.

For modelling the behavior of the blank during the hot stamping process, a material model was developed by Åkerström [56]. The material model captures phase transformations, latent heat, transformation induced plasticity and plastic effects. An incremental decomposition of the strain increment is adopted as described by:

$$\Delta\varepsilon_{ij} = \Delta\varepsilon_{ij}^{e} + \Delta\varepsilon_{ij}^{th} + \Delta\varepsilon_{ij}^{tr} + \Delta\varepsilon_{ij}^{p} + \Delta\varepsilon_{ij}^{tp} \quad \textbf{(1)}$$

where $\Delta\varepsilon_{ij}$ represents the total strain increment, $\Delta\varepsilon_{ij}^{e}$ represents the elastic strain increment, $\Delta\varepsilon_{ij}^{th}$ represents the thermal strain increment, $\Delta\varepsilon_{ij}^{tr}$ represents the isotropic phase transformation strain

increment, $\Delta\varepsilon_{ij}^{p}$ represents the plastic strain increment and $\Delta\varepsilon_{ij}^{tp}$ represents the transformation induced plastic strain increment. Each of these strains is calculated based on formulas developed by Åkerström [56].

The Vickers hardness in the blank is calculated by a weighted average that was originally proposed by Maynier et al. [57]. The weighted average is calculated as:

$$HV = X_b HV_b + X_f HV_f + X_p HV_p + X_m HV_m \quad \textbf{(2)}$$

where X represents the volume fraction of a particular phase, HV represents the Vickers hardness of a particular phase, and the subscripts b, p, f and m denote bainite, pearlite, ferrite and martensite, respectively. The individual Vickers hardness for each phase is calculated using formulas, which were derived by other investigators [58, 59, 60].

Olsson [61] implemented a material model for hot stamping into the commercial FE package LS-Dyna, designated as **MAT_244*. It was based primarily on the work of Åkerström et al. [62] and Åkerström and Oldenburg [46], but contained modifications made by Li et al. [63] to predict the microstructural composition in the blank. Since its initial implementation, several revisions have been made to **MAT_244*, such as the ability to scale the activation energies of each phase based on the amount of plastic strain in an element [64]. The ability to manually input the Vickers hardness of the martensite and bainite phases as a function of temperature, instead of using the formulas proposed by Åkerström, has also been added [64].

1.5 Numerical Modelling of the Crash of THS Components

Crash experiments, whether they are axial crash or side-impact, are usually modelled with a rigid, non-deformable impactor [26, 30-32, 35, 38]. The impactor is either given a prescribed velocity or an initial velocity and inertia (i.e., mass). Contact is defined between the impactor and crash specimen. In axial crash modelling, nodes on one end of the specimen are usually constrained from moving [38, 65]. The resulting force-displacement curves from the model can be obtained by either the contact force between the impactor and crash specimen, or in an axial crush, by the reaction forces at the fixed nodes.

These aforementioned points describe the general approach to modelling crash experiments. One concern, specifically pertaining to the crash of tailored hot stamped components, is how to accurately map the flow stress properties onto the as-formed blank from the THS model. To address this concern, Bardelcik et al. [66] developed a model that predicts the flow stress properties of Boron steel as a function of effective plastic strain, strain rate and Vickers hardness. The model is based on a modified version of the Voce [67] hardening model:

$$\sigma = \left(A + \left((B - A)e^{-\frac{\varepsilon}{C}}\right)\right)(1 + \dot{\varepsilon})^D \tag{3}$$

Bardelcik et al. [66] defined the parameters A, B, C and D in (3) as functions of the as-hot stamped Vickers hardness:

$$A = 0.005318HV^2 - 0.7902HV + 699.49 \tag{4}$$

$$B = 2.499HV - 71.24 \tag{5}$$

$$C = \begin{cases} -7.747 \times 10^{-9}HV^3 + 9.222 \times 10^{-6}HV^2 - 0.003652HV + 0.4884, & 266 < HV < 375 \\ 0.0072, & HV > 375 \end{cases} \tag{6}$$

$$D = 0.018 \tag{7}$$

The above set of equations constitutes the Tailored Crash Model (TCM) [66], which was calibrated using specimens exhibiting a martensitic and/or bainitic microstructure only. Bardelcik et al. [68] devised another model called the Tailored Crash Model II (TCM II), which accounts for the presence of ferrite in the microstructure, which the TCM did not. Bardelcik et al. [68] recommend the TCM II for Vickers hardness values less than 466 HV. For values greater than 466 HV, the original TCM is recommended.

The TCM II is based on the same modified Voce hardening formula shown in (3). The parameters A, B, C and D, however, are functions of the area fraction of bainite, martensite and ferrite, instead of the Vickers hardness. All four parameters can be determined by the following polynomial form:

$$\boldsymbol{A, B, C, D} = \beta_1 + \beta_2\left(\frac{M}{M+B}\right) + \beta_3 F + \beta_4\left(\frac{M}{M+B}\right)^2 + \beta_5 F\left(\frac{M}{M+B}\right) + \beta_6 F^2 \quad \textbf{(8)}$$

And the values to be used for the coefficients, β_n, are given in Table 2. The TCM II model was calibrated using specimens containing 20% volume fraction ferrite and exhibiting hardness values as low as 240 HV.

Table 2. Coefficient values for the TCM II model **[68]**

	$\boldsymbol{\beta_1}$	$\boldsymbol{\beta_2}$	$\boldsymbol{\beta_3}$	$\boldsymbol{\beta_4}$	$\boldsymbol{\beta_5}$	$\boldsymbol{\beta_6}$
A	853.0	809.3	3050.0	-152.9	2.016	-2.051 x 10^4
B	602.7	631.8	1438.0	-98.36	980.5	-1.599 x 10^4
C	0.01875	-0.03875	0.16570	-0.03009	-0.2300	0.24470
D	0.018	-	-	-	-	-

The combined TCM and TCM II models can be used in crash simulations of tailored hot stamped parts. The predicted hardness values and area fractions of bainite, martensite and ferrite at the end of a hot stamping simulation can be used to generate flow stress curves to be used in crash models. This approach can be applied for each element in the blank; however, this would require considerable computing resources for large models with many elements. A more efficient technique would be to sort the elements into bins of elements with similar as-formed hardness or predicted phases, with each bin being assigned one set of flow stress data. This technique was employed by Bardelcik et al. [35] to model the 3-point impact of a B-pillar. The B-pillar was sorted into eight bins. A failure criterion to model crack propagation in the B-pillar was not included in that work.

1.6 Current Work

As mentioned at the end of section 1.3, no study currently exists investigating the effect that tailoring a hot stamped axial crush member exerts on its crash behavior. While there have been some numerical studies done on this topic, which have been discussed, no detailed experimental work has been carried out. The absence of experimental work means there is no definitive way to validate the numerical studies and numerical models that already exist. It also means that there is no quantitative measure on the effect of tailoring an axial crush member.

Therefore, there exists a need to conduct an experimental study on the crash response of tailoring the properties of a hot stamped axial crush member. There also exists a need to be able to validate the numerical models in existence, particularly the TCM I and TCM II constitutive models describing the crash response of tailored hot stamped components that were discussed in section 1.5. The work described in this thesis attempts to fill this gap in the literature.

This thesis is part of a broader project sponsored by Honda R&D Americas, Promatek Research Centre and ArcelorMittal Dofasco. The goal of this project is to investigate the crash response of tailored hot stamped components and to more accurately model the THS and crash processes, focusing primarily on Usibor® 1500P, a hot stamping alloy produced by ArcelorMittal.

There were four tasks in this project. Task 1 focused on investigating and modelling the crash response of a tailored side impact beam. Task 2 focused on investigating and modelling the crash response of a tailored axial crush member. Task 3 was to characterize the effect of heating on the HTC between the blank and tooling, and was conducted by Caron et al. [49, 52], as explained in section 1.4. Task 4 was to experimentally determine a failure criterion for Usibor® 1500P at different micro-hardness levels, which was to be used in crash models.

The work highlighted in this thesis pertains to Task 2 of the overall hot stamping project. Specifically, an axial crush member consisting of a double top hat cross-section was analyzed. Blanks made out of Usibor® 1500P were hot stamped in a die set that allowed for up to three distinct temperature zones during the forming process. The blanks were formed at different

temperatures in the die, and micro-hardness measurements were conducted in the formed part to map the Vickers hardness profile along its lateral axis.

The hot stamping process was also modelled using the material model developed by Åkerström [56], and by using many of the techniques described in section 1.4. The predicted Vickers hardness distributions were then compared against the measured results. The formed parts were then crashed axially at different velocities and the crash process was modelled. The force displacement curves obtained numerically and experimentally were analyzed and compared.

The remainder of this thesis describes the experimental and numerical analysis conducted for this work. Chapter 2 details the experimental approach used in this work and describes the setup for the THS, micro-hardness and crash experiments. Chapter 3 describes the THS and crash numerical model setups. Chapter 4 discusses results obtained from the THS and micro-hardness experiments and compares them with the results from the THS models. Chapter 5 discusses results obtained from the crash experiments and compares them with the results from the crash models. Chapter 6 draws conclusions and makes recommendations for future work.

2. Experiments

2.1 Overview of Experimental Programme

The focus of this work was to investigate the crashworthiness of an axial crush member incorporating tailored properties along its length and to validate the THS and crash numerical models. A key objective of this thesis is to determine if tailoring the hardness properties of a part at different temperatures improved its energy absorption and overall deformation pattern compared to a non-tailored, fully martensitic part.

To achieve this objective, a non-tailored, fully martensitic part and three configurations of tailored parts were investigated, as illustrated in Figure 9. The parts were tailored such that they contained a distinct martensitic zone and up to two bainitic/ferritic zones. The shape and dimensions of the as-formed hot stamped parts that were investigated in this work are shown in Figure 10. All formed parts were made out of Boron steel (Usibor® 1500P) and had a top hat cross-section consisting of flanges on both sides and a C-channel consisting of walls and a top section. The total length of each formed part was 590 mm, and total width was 125 mm. The width of the top section of the C-channel was 60 mm.

The non-tailored, fully martensitic part was formed in tooling that was not heated and is referred to herein as *fully cooled*. The three tailored configurations were subdivided into two categories: those containing only one bainitic/ferritic zone, called *single soft* zone parts and those containing two bainitic/ferritic zones, called *graded soft zone parts*. For the *single soft zone* parts, the entire tooling was heated to 400˚C in one case and to 700˚C in another case, resulting in two configurations of *single soft zone* parts. For the *graded soft zone*, a portion of the tooling along the length of the part was heated to 400˚C while the remaining portion was heated to 700˚C. A description of the tooling is given in section 2.2.

The THS process was divided into four stages: Transfer, Forming, Quenching and Cooling. In the transfer stage, the pre-heated blank was transferred from the furnace into the die-set. The forming stage of the process consisted of the descent of the tooling onto the blank and the die close to form the geometry. The quenching stage occurred subsequently in which the formed

blank was held in the tooling for a certain time period at a certain tonnage. The final stage, which was the cooling stage, was when the blank was removed from the tooling and allowed to cool in air until it reached room temperature. Details of the forming process are given in section 2.3.

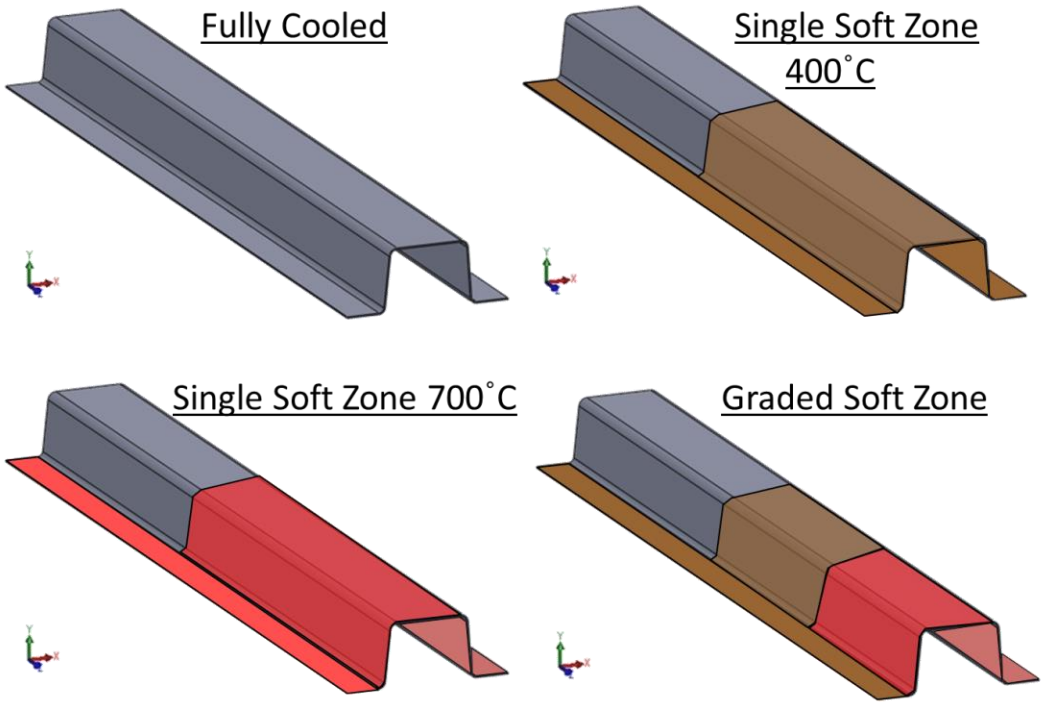

Figure 9. The types of tailored and non-tailored parts investigated in this work

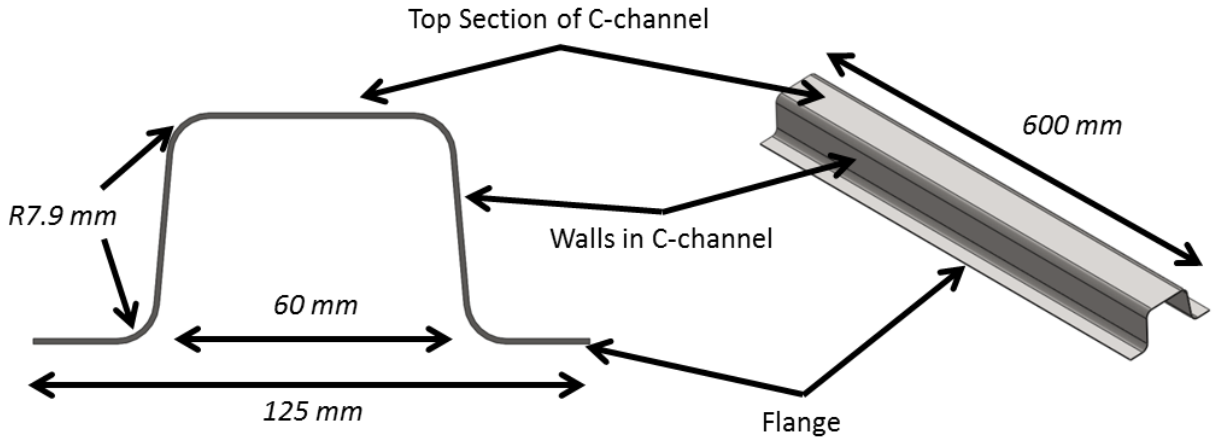

Figure 10. Shape and dimensions of the specimens investigated in this work

After the blanks were formed, the as-formed parts were welded in pairs along their flanges and prepared for axial crush. The preparation process is described in section 2.5. Two types of axial

crush experiments were performed in this work: dynamic and quasi-static. The dynamic crush setup is discussed in section 2.6 and the quasi-static crush setup is discussed in section 2.7. Force-displacement curves were extracted from these crash experiments and analyzed. These curves also served as a validation tool to assess the numerical crush models.

2.2 Description of Forming Tooling

The tooling used to form the axial crush members was designed by George [31] as part of the broader scope of the hot stamping project, which was described in section 1.6. The axial crush tooling was divided into two sections: a water-cooled section corresponding to the hardened martensitic zone in the formed parts and a heated section corresponding to the soft zone(s) of the formed parts. The female die and flange and the male punch and binder are shown in Figure 11. The two sections in the tooling were separated by an air gap of 3.2 mm. Water coolant was pumped through the cooled punch and die and was able to maintain a steady state temperature of 12˚C.

The heated section in the tooling was subdivided into two zones separated by an air gap of 2 mm. The two heated zones enabled fabrication of the *graded soft zone* part shown in Figure 10. The temperature in the heated section of the tooling was held constant using PID controllers, and the heat was provided by 550W cartridge heaters at 600V, which were 3/4” in diameter.

Forty-four heaters were inserted in the tooling: two in each of the heated punches, four in each side of each heated die and flange, four in each side of the flange in the cooled section of the tooling and eight in each side of the binder. This is illustrated in Figure 12. The heaters in the flanges on the cooled section of the tooling and in the heated punches were 3” in length, while the heaters in the heated die were 6” in length. All remaining cartridge heaters (in the binder, and flanges on the heated section of the tooling) were 4” in length.

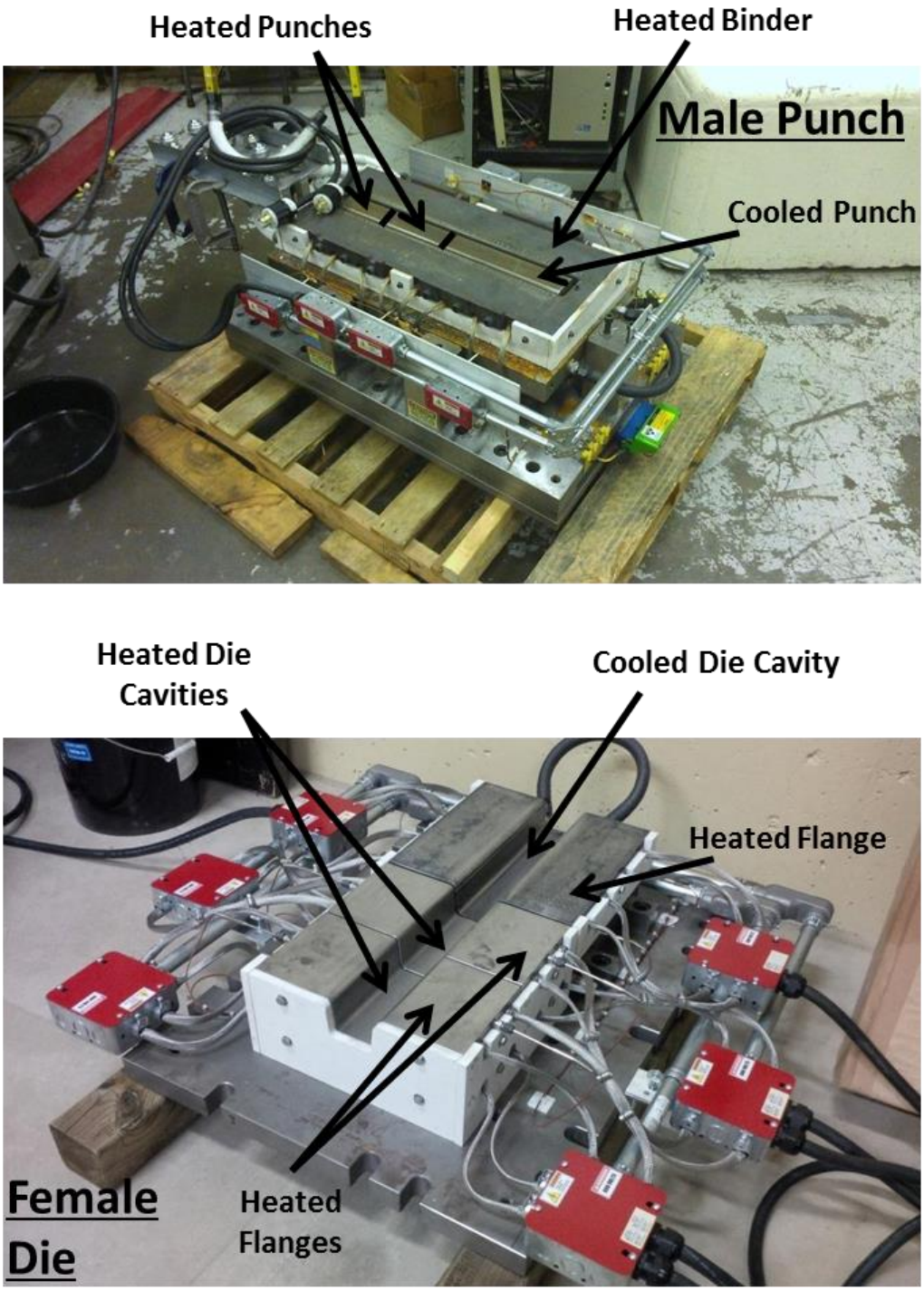

Figure 11. Tooling used to form the axial crush members.

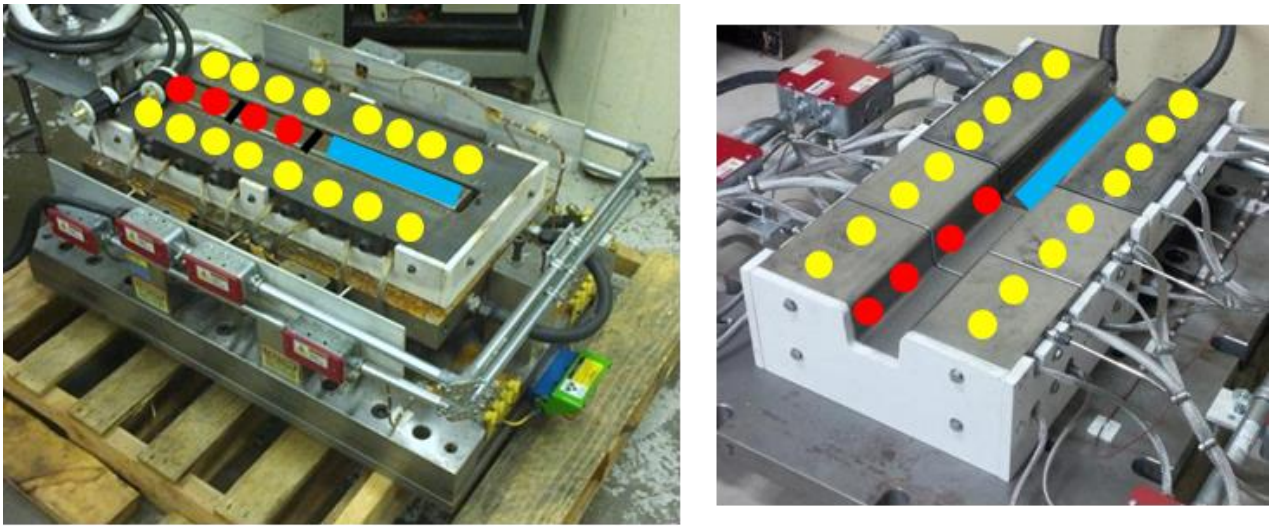

Figure 12. Locations where cartridge heaters were inserted in the axial crush tooling. The blue line indicates water-cooled regions. The yellow dots indicate heaters in the binder (male) and flange (female). The red dots indicate heaters in the punch (male) and dies (female)

The heated sections of the tooling were surrounded by a 0.5”-thick layer of ZIRCAL-95 insulation. The thermal conductivity of this material was 0.31 W/mK at 200˚C, 0.29 W/mK at 400˚C and 0.27 W/mK at 600˚C [69]. This white coloured insulation can be seen in Figure 11 and Figure 12 around the tooling. The layer of insulation prevented heat loss to the outer surroundings when the tooling was heated to 400˚C and 700˚C. It also prevented heat loss to the press.

The heating circuits were set up such that there were twelve control zones, which are illustrated in Figure 13. The tooling was heated using a ramp function. Each zone had one or two thermocouples placed inside to monitor temperature.

The final aspect of the axial crush tooling was the inclusion of shims to account for thermal expansion at elevated temperatures. At room temperature, both the cooled and heated punch/die were levelled with each other. However, as shown in Figure 14, at elevated temperatures, the heated punch and die expanded, which created a ridge between the two sections of the tooling. To rectify this, shims were inserted in the cooled tooling for the *single soft zone* and *graded soft zone* cases. The height of the ridge was measured using feeler gauges and was found to be 0.016”

in the die and 0.006” in the punch for the *single soft zone 400˚C* case. For the *single soft zone 700˚C* case, the height was measured to be 0.023” in the die and 0.026” in the punch.

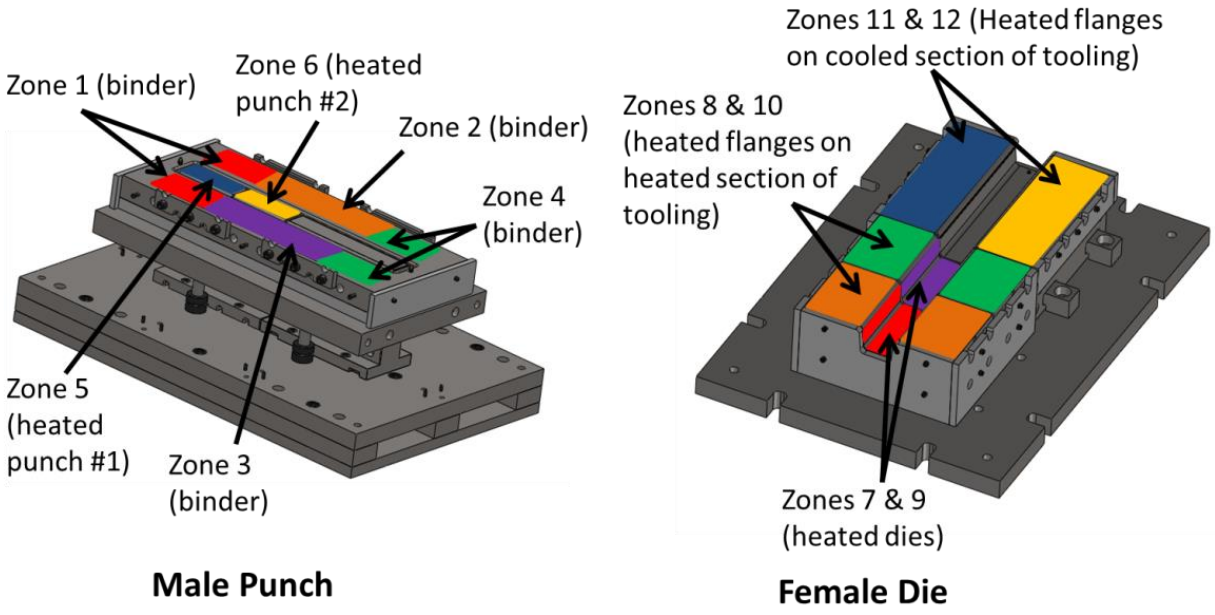

Figure 13. The control zones for heating the axial crush tooling

For the *graded soft zone* case, two ridges were created: one between the cooled section of the tooling and the first heated zone (at 400˚C), and another between the two heated zones. Due to the fact that the two heated punches were connected to a single layer of insulation and a single block of steel (as shown in Figure 14), the heated zone at 400˚C could not be shimmed. Likewise, the 400˚C zone die was dowelled against the mounting plate and had a thermocouple connected through it, making it very difficult to shim. Therefore, only the cooled punch and die were shimmed and levelled relative to the 700˚C zone (see Figure 15). The ramification of the inability to shim the 400 and 700˚C zones separately is addressed in section 4.1.1 where the resulting micro-hardness measurements are presented.

The cooled punch and die were designed to allow for easy insertion of shims, by being attached to the top and bottom plates using four screws. The screws were inserted from the “visible” side of the tooling as shown in Figure 16 and Figure 17. Furthermore, the cooled punch contained four cutouts where levers could be inserted to lift the punch to allow insertion of the shims (Figure 16).

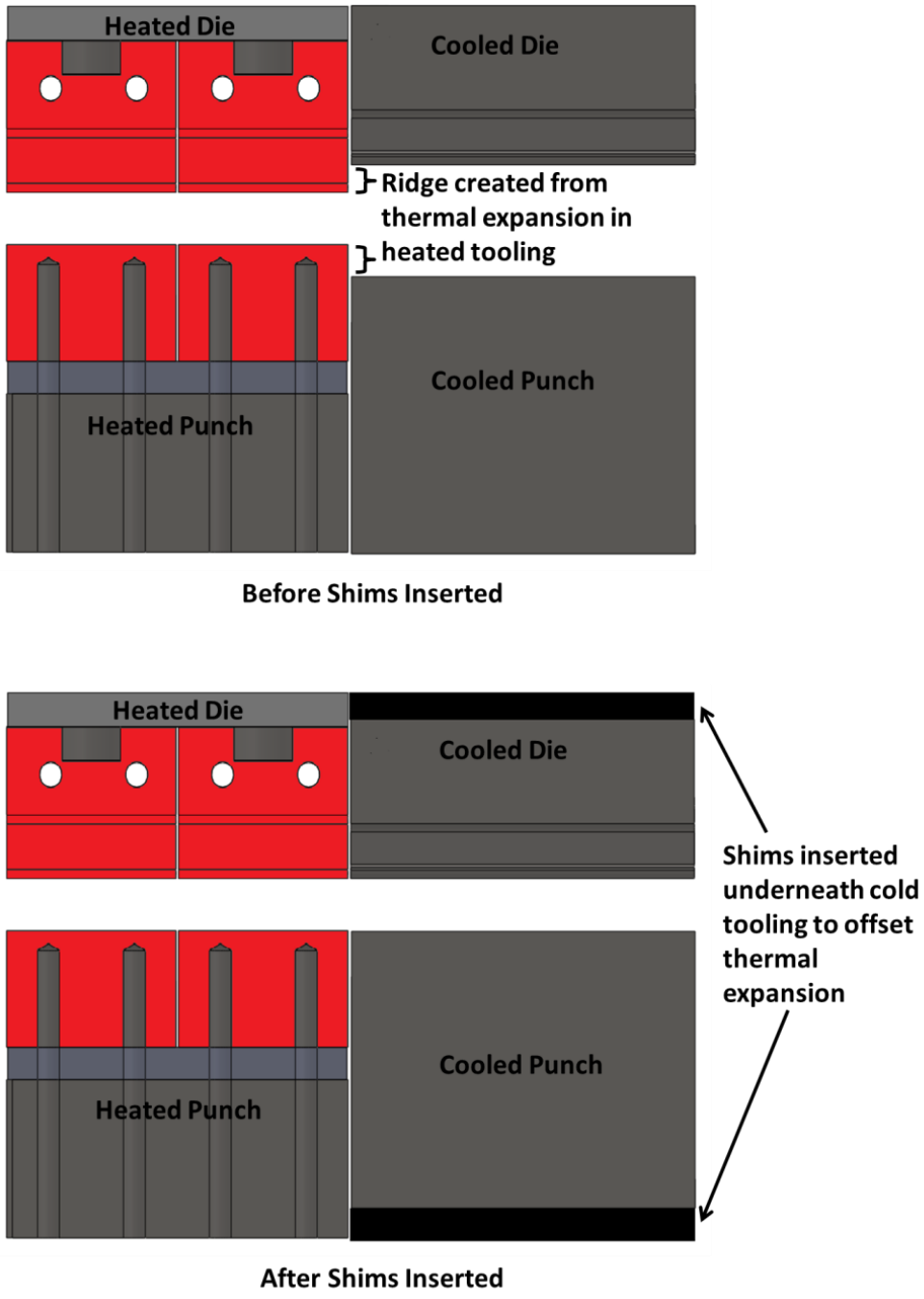

Figure 14. Diagram outlining the thermal expansion in tooling and the insertion of shims to counteract this

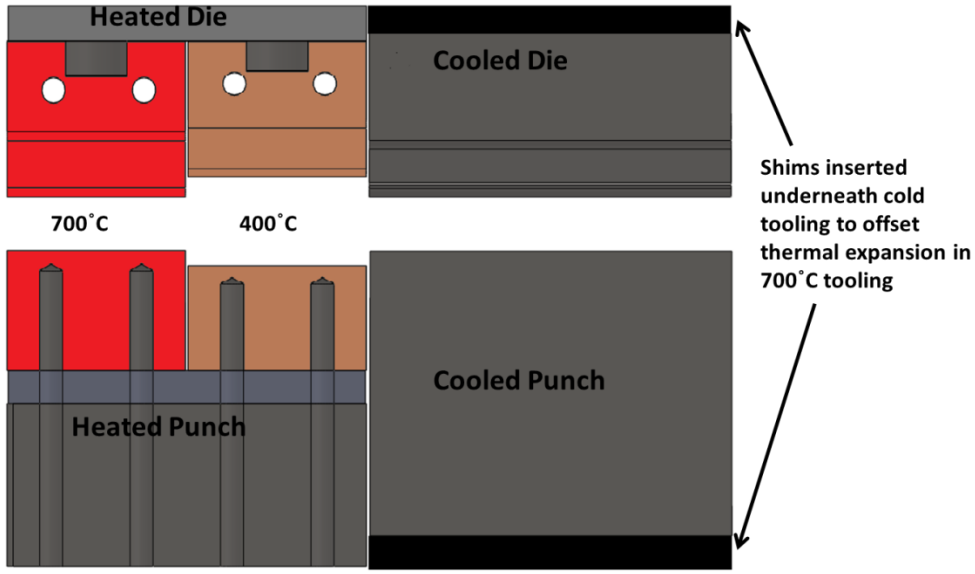

Figure 15. Diagram outlining the shimming of the tooling for the *graded soft zone* case

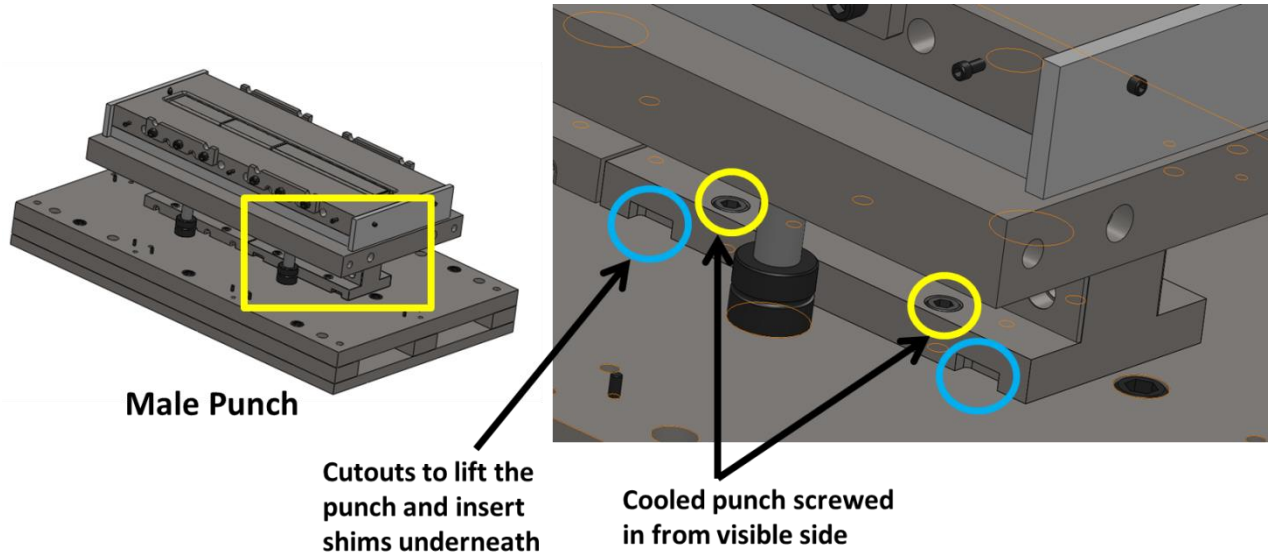

Figure 16. Mounting of the cooled punch

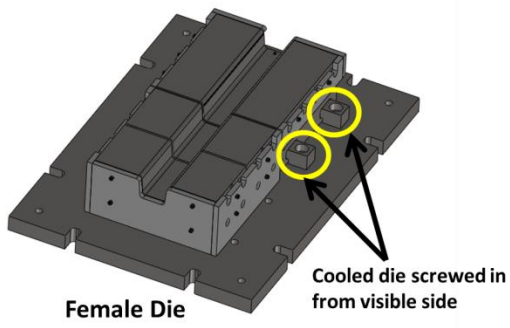

Figure 17. Mounting of the cooled die

2.3 THS Process Parameters

The THS process in this work was performed on a hydraulic forming press manufactured by Macrodyne Technologies Inc, which is pictured in Figure 18. The press was capable of exerting up to 900 tons of force using a main cylindrical actuator. The press also contained four smaller cylinders, called kickers, which were capable of generating 60 tons of force and higher speeds as well.

Ideally, the THS process in this work would have employed the kickers for the initial descent of the press and switched over to the main cylinder when contact with the blank was made. However, due to technical difficulties with the press, it took too much time to switch between the main cylinder and kickers. The blank would have cooled down too much in this switchover time and therefore the austenite decomposition would have started before the blank was formed. Using only the main cylinder for the entire press cycle was also not feasible since it would have taken too long for the press to descend onto the blank. In light of these technical problems, only the smaller kickers were used for the entire THS process in this work. As such, a total tonnage of only 60 tons could be achieved during the forming cycle.

The tooling described in section 2.2 was mounted inside the press as shown in Figure 18. An oven in which the blank was pre-austenized before forming was located behind the press. The oven was manufactured by Deltech, Inc. and contained three control zones: one at the front, one at the back and one in the middle. The three control zones ensured that the blank was evenly heated throughout its length.

An automated pneumatic-powered transfer mechanism moved the heated blank from the oven into the press where it was formed and quenched. The transfer mechanism consisted of a rail that moved along guides from the press to the oven, and a grip that clamped the heated blank and pulled it into the press. The transfer mechanism is illustrated in Figure 19. To minimize heat lost from the blank due to contact with the grips within the transfer mechanism, the grips clamped onto the tab at the edge of the preformed blank. In addition, the grip surface in contact with the blank was an insulator so as to limit heat transfer from the blank. With these precautions, the temperature in the main portion of the blank was unaffected.

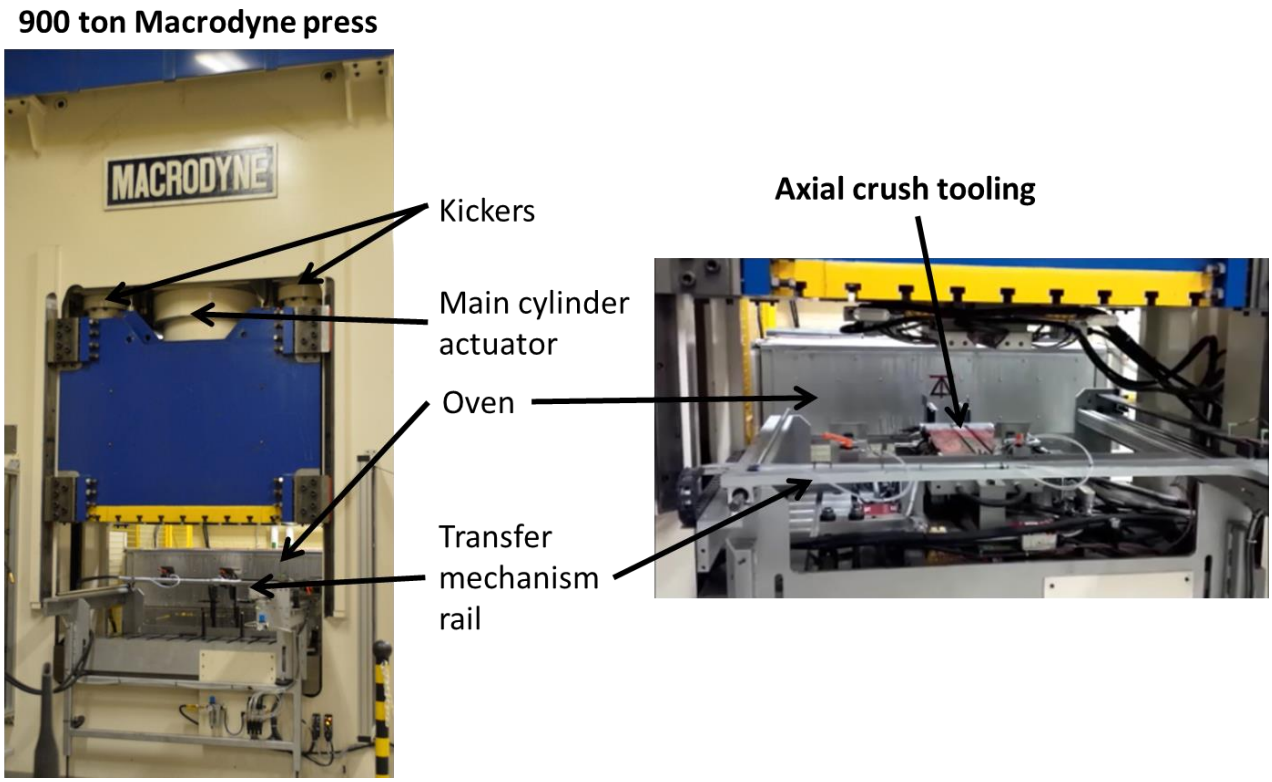

Figure 18. Press and oven setup for the THS process in this work

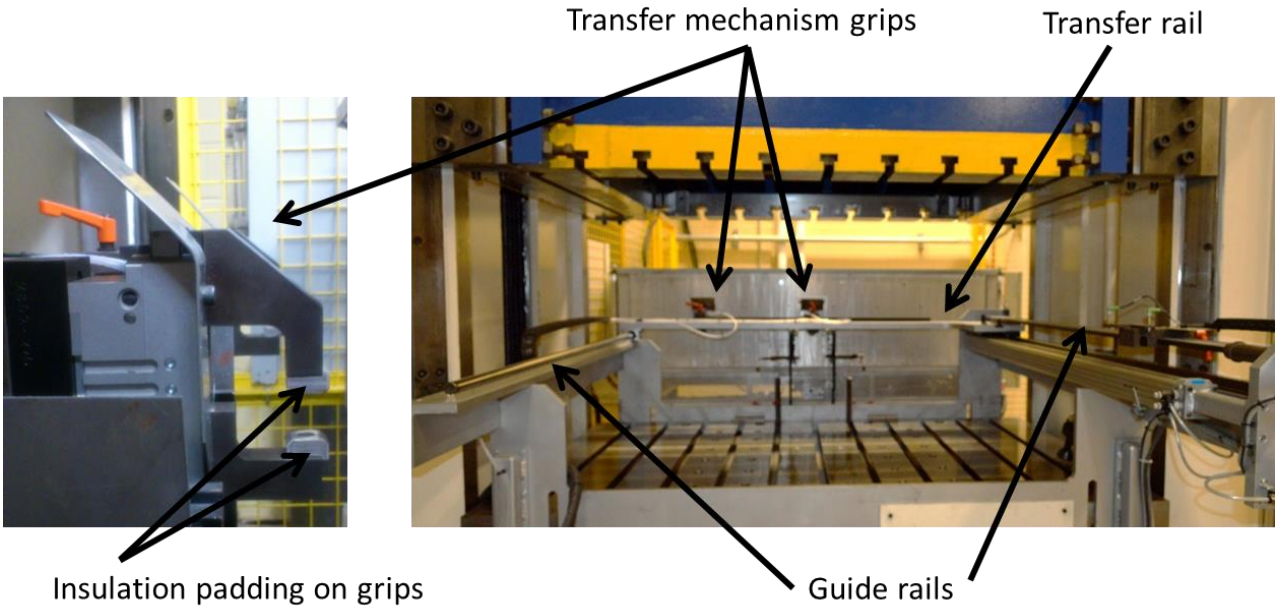

Figure 19. The transfer mechanism used to move the blank from the oven to the press

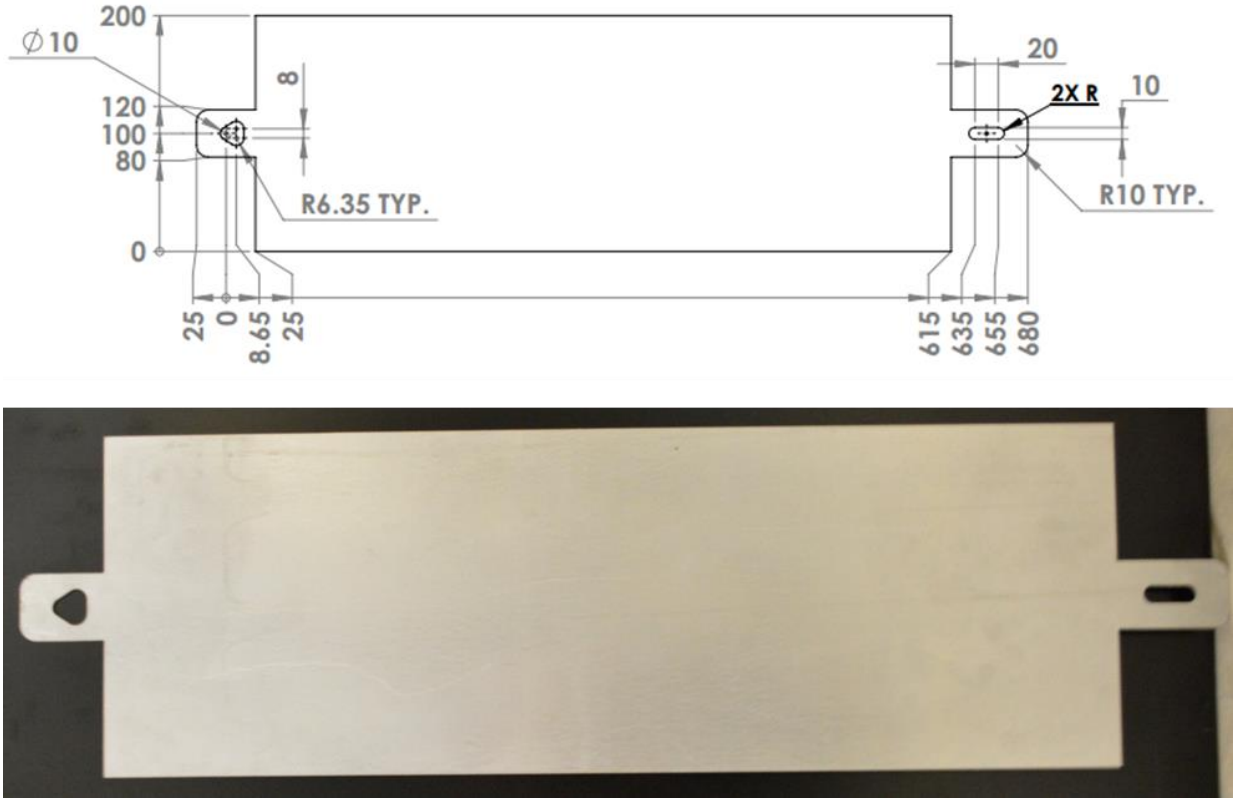

Figure 20. Shape and dimensions (in mm) of the pre-formed blank

The dimensions of the pre-formed blank were 590mm x 200mm. In addition to this, the blank incorporated of two tabs on both of its ends (Figure 20). One tab contained a triangular slot while the other contained an obround slot. The slots were used to align the blank in the tooling. Also, on some occasions, the blank became wedged in the female die after the THS process was complete and the tabs allowed for an easy removal of the blank from the tooling.

During the THS process, the male punch remained stationary while the female die descended and formed the blank. The binder surrounding the punch was mounted on a series of twelve nitrogen cylinders that exerted a constant pressure of 6.895 MPa (1000 psi). The diameter of the face of these cylinders was 23 mm, resulting in a total force of 34.4 kN that the binder exerted against the die.

The specific stages of the THS process were as follows (Figure 21):

a) The blank was placed in a 930˚C oven for six minutes, allowing it to austenize
b) The blank was then transferred into the die set using the pneumatic transfer mechanism, and aligned using two alignment pins located in the tooling (transfer step is approximately 10.5 s in duration)
c) The blank was then formed, and quenched in the tooling for 4s at a force of 60 tons
d) The formed blank was removed from the tooling and cooled in air

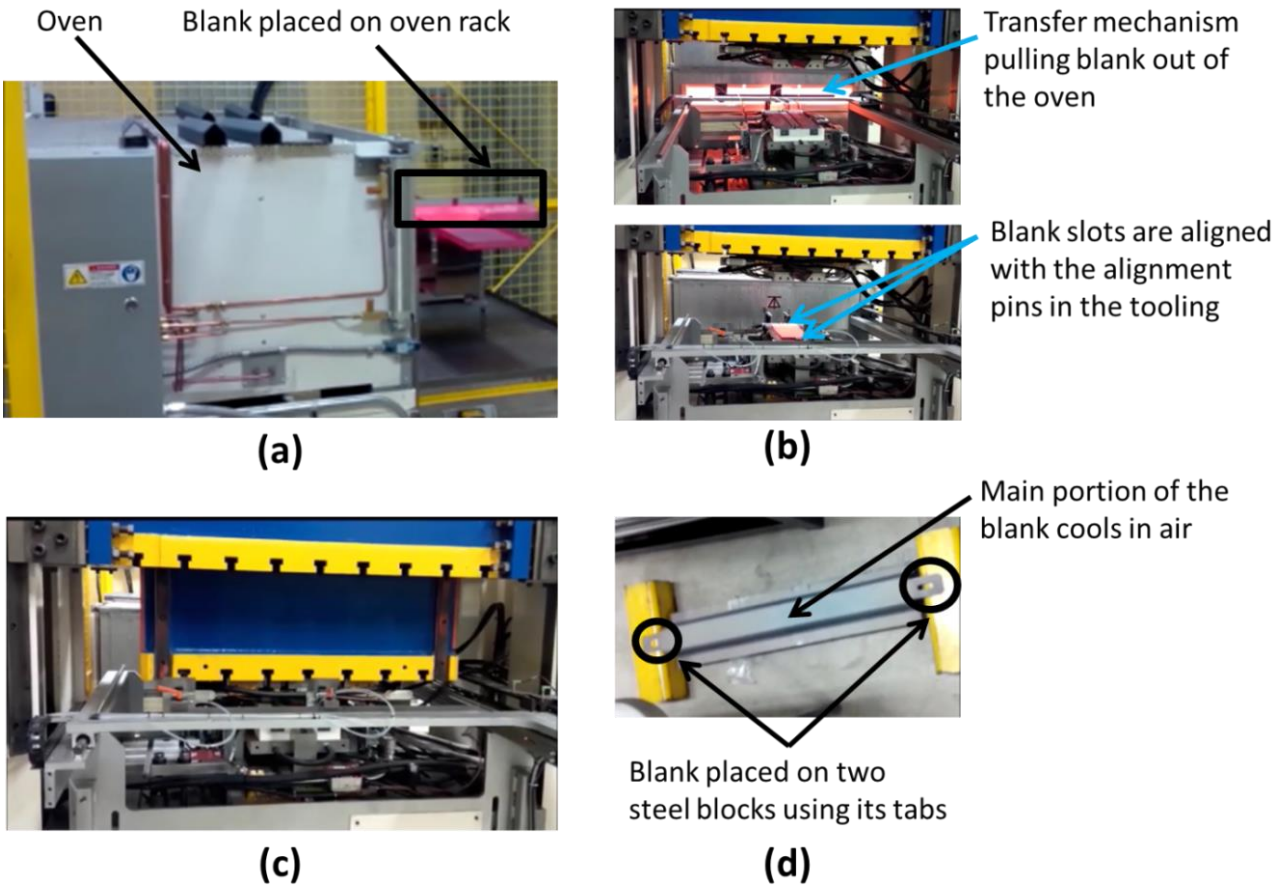

Figure 21. Each stage of the THS process: (a) Blank is placed in oven, (b) Blank is moved from the oven into the press, (c) Blank is formed and quenched and (d) Blank is cooled in air

2.4 Micro-Hardness Measurements on as-Formed Parts

After the blanks were formed, micro-hardness measurements were taken along the flanges, walls and top sections of the formed parts. Laser cutting (performed by Promatek Research Centre) was used to extract sample blanks from the as-formed parts, shown in Figure 22, from which hardness and tensile samples could be fabricated. The laser cut blanks were further cut down to hardness samples measuring 20 mm in length using a wet saw. The 20 mm hardness samples were mounted into pucks that were made of a mixture of epoxy resin and hardener (ten pieces were mounted in each puck). The pucks (shown in Figure 23) were polished using grit SiC paper in the following order: 220/320, 500, 800, 1200 and 2400.

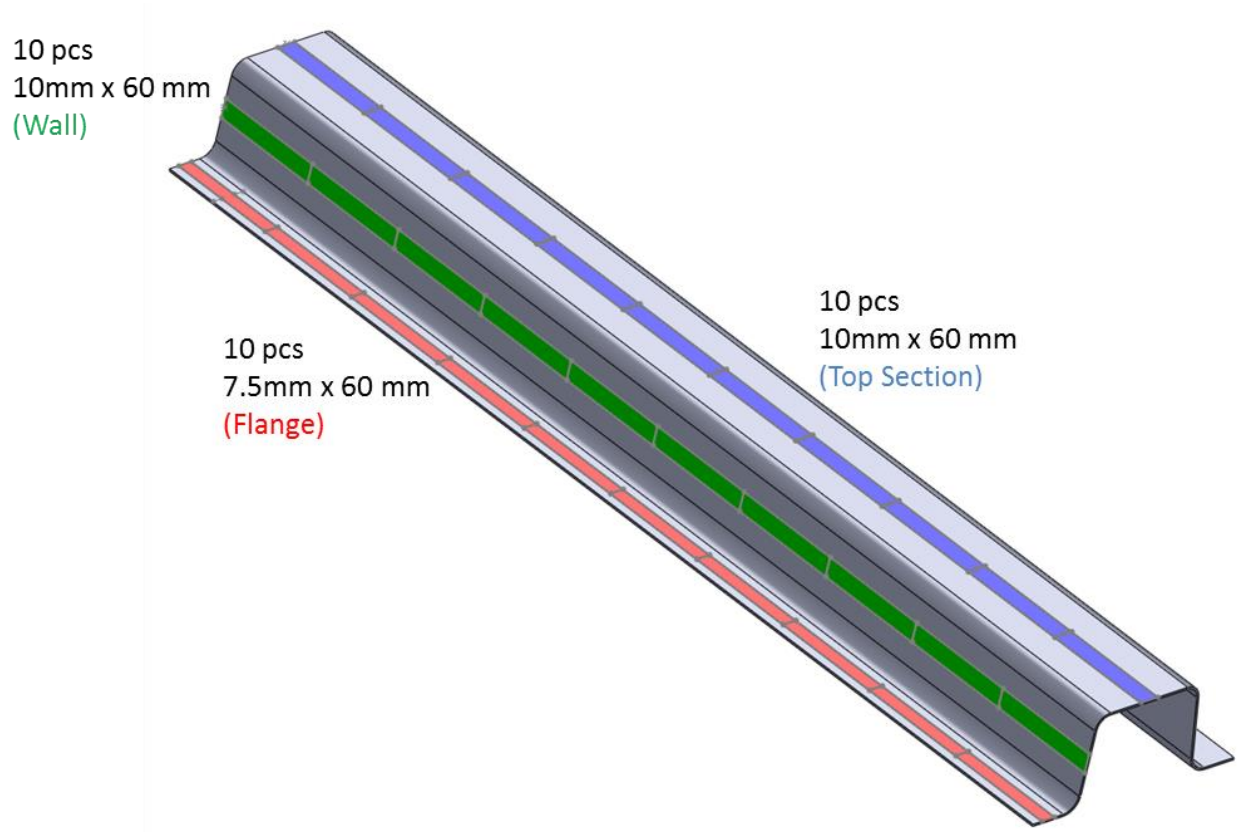

Figure 22. Laser cutouts from the formed parts

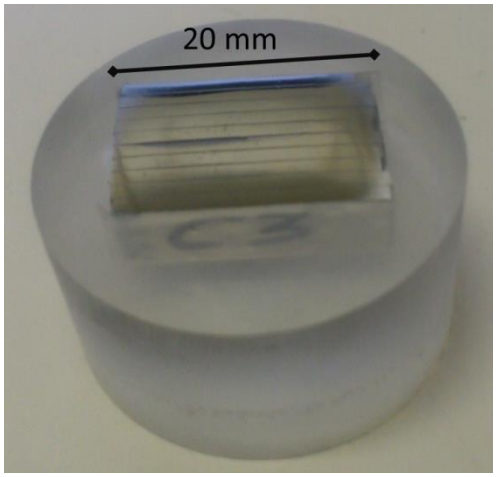

Figure 23. Image of an epoxy resin puck with ten 20 mm pieces mounted for micro-hardness measurements

Vickers hardness measurements were taken every 10 mm along the length of the as-formed parts, except in the transition zone(s), where it was measured every 5 mm. The transition zone in each formed part was assumed to be 80 mm in length, located at the halfway mark in the axial direction (pictured in Figure 24). In addition to this, the *graded soft zone* parts had a second transition zone located 150 mm from the soft end, corresponding to the different heated zones in the tooling (also pictured in Figure 24).

A LECO MHT Series 2000 hardness tester was used to make pyramid indents into the metal specimens with a load of 1000g. A MicroPublisher 5.0 RTV microscope was used in conjunction with the ImagePro 5.1 software package to measure the length of the diagonals of the pyramid indents and to calculate Vickers hardness using these lengths. This software package was also used to measure the thickness of the material at the same locations as the Vickers hardness.

The Vickers hardness measurements served as a method to confirm that the as-formed parts did, in fact, have the type of axial tailoring that was desired for crash experiments. The hardness measurements and the material thickness measurements also provided a method of validating the results of the THS models.

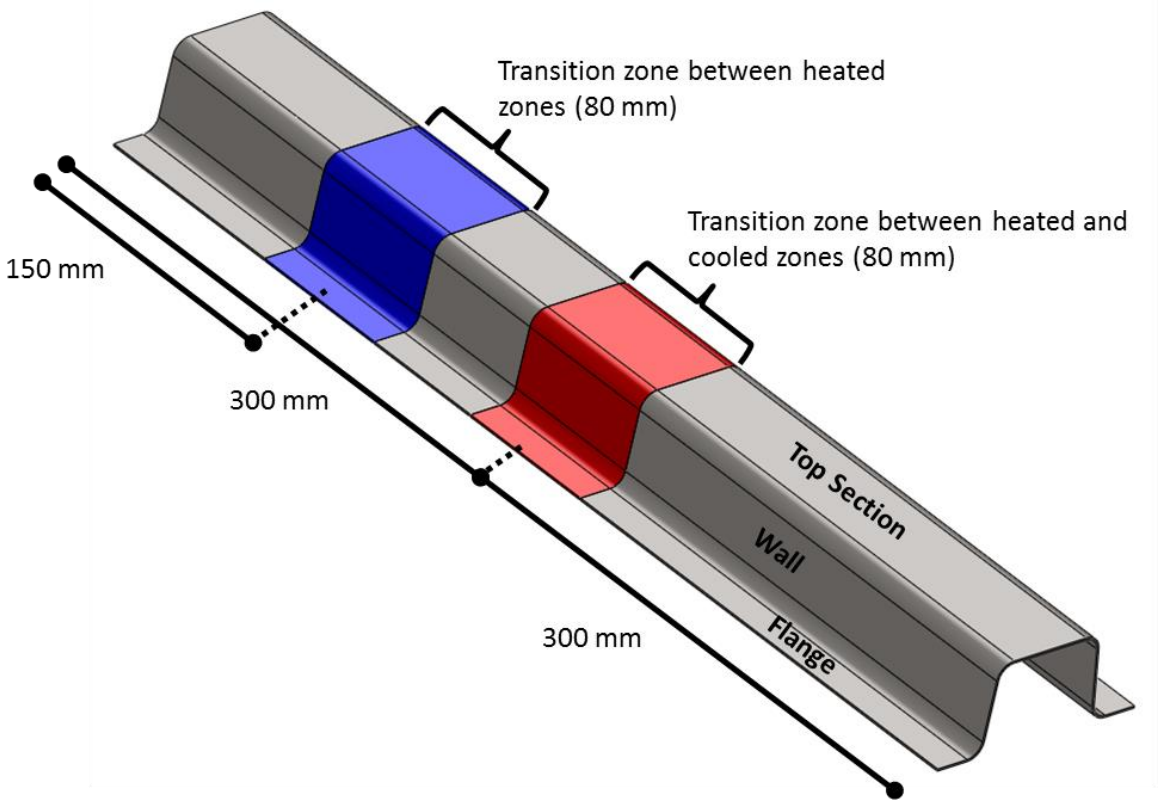

Figure 24. The transition zones in the formed part where hardness measurements were taken every 5 mm

2.5 Preparation of Formed Parts for Crash Experiments

To prepare the formed parts for crash testing, two parts were spotwelded every 25 mm along their flanges (shown in Figure 25). The spotwelding was performed by Promatek Research Centre. The tabs on both ends (which can be seen in Figure 20) of the parts were cut off using an abrasive saw.

To control the initiation of folding in the specimens during crash, a dimple was inserted 65 mm from the soft end of the part (i.e., the end corresponding to the heated section of the tooling). Figure 25 shows the location of the dimple in one crush specimen. The dimple was formed on a hand press using a punch measuring 25 mm x 10 mm in size and incorporating a fillet of radius 5 mm on all its edges. The punch is shown in Figure 26. The loads used to form the dimple in each part were: 450N for the *graded soft zone* and *single soft zone 700˚C* parts, 630N for the *single soft zone 400˚C* parts and 850N for the *fully martensitic* parts.

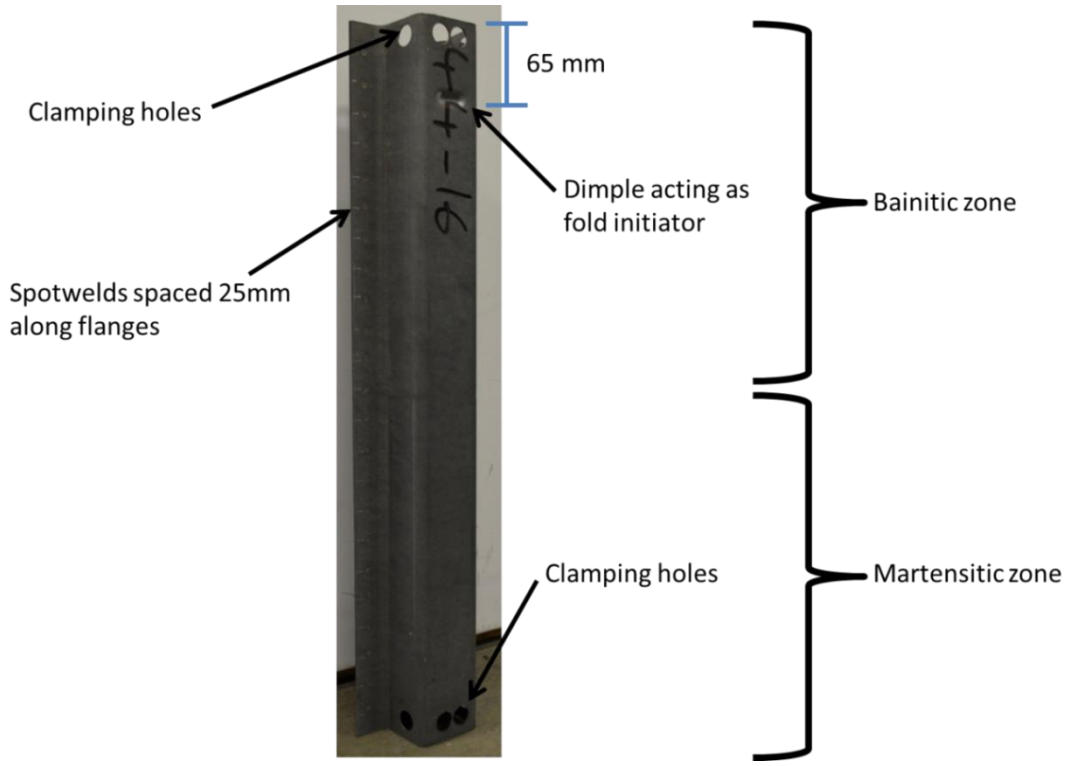

Figure 25. Two formed parts welded together to be crushed

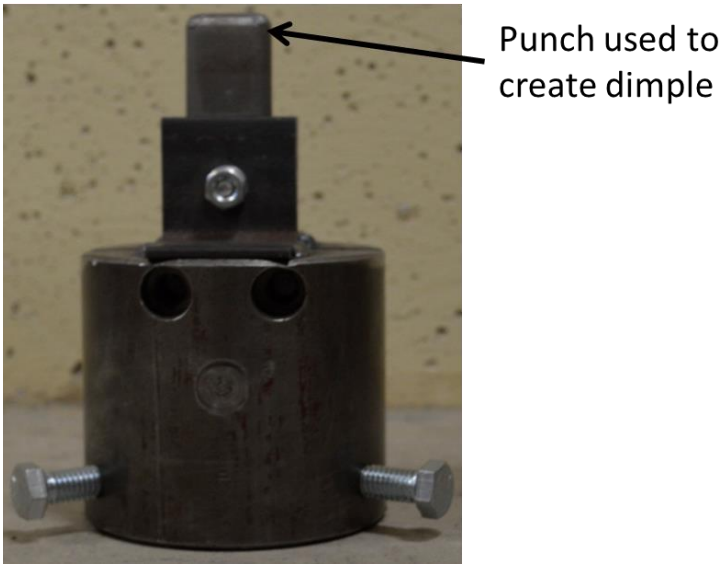

Figure 26. Punch used to insert dimple into the crash specimens

These loads were selected based on the measured micro-hardness in each type of part. A load of 450N was selected for the *graded soft zone* and *single soft zone 700˚C* part and scaled accordingly to attain the same dimple penetration for the *single soft zone 400˚C*. Ideally, a forming load of 1100N would have been used for the *fully cooled* parts, however forming loads

higher than 850N caused cracking in these martensitic parts, which would have affected the failure response during crash. Therefore, a load of 850N was selected in these parts, resulting in a dimple that did not penetrate as deeply as it did in the other types of parts. The shallower dimple in the *fully cooled* specimens did affect their load-displacement behavior during crash. This will be discussed in greater detail in section 5.1.1.

For the dynamic tests on the crash sled, the specimens were cut down by a length of 100mm along their martensitic zones to reduce the likelihood of global buckling. The final length of the dynamic crush specimens, therefore, was 490 mm instead of 590 mm.

2.6 Dynamic Crash Setup

Figure 27 shows the setup for the dynamic tests conducted using the University of Waterloo crash sled. The crush specimen was mounted 220 mm above the base of the sled. The specimen was clamped at both ends using a central boss and four outer clamps. A CAD drawing of these clamps is shown in Figure 28.

The clamps and boss used to mount the martensitic end of each specimen (mounted at the fixed impact wall) were 50 mm thick while those used to mount the bainitic end were 25 mm thick (the free end). This meant that the unclamped length of the specimen was 415 mm. All outer clamps and the bosses were mounted to a plate using two UNC 5/16-18 screws. Furthermore, each outer clamp was bolted onto the internal boss using two UNC 5/16-18 screws through holes that were laser cut at the appropriate locations in the crush specimens. The clamping holes in the specimens are shown in Figure 25. The clamping holes on the martensitic end were located 25 mm from the end of the specimen, while the clamping holes on the bainitic end were located 12.5 mm from the end of the specimen.

A 0.75” thick piece of plywood was mounted on the free end of the crush specimen to act as a damper between the sled and mounting plate and reduce ringing in the load cells. The total mass of the sled was 855 kg and an initial velocity of 10.6 m/s (38.2 km/h) was employed for all dynamic tests.

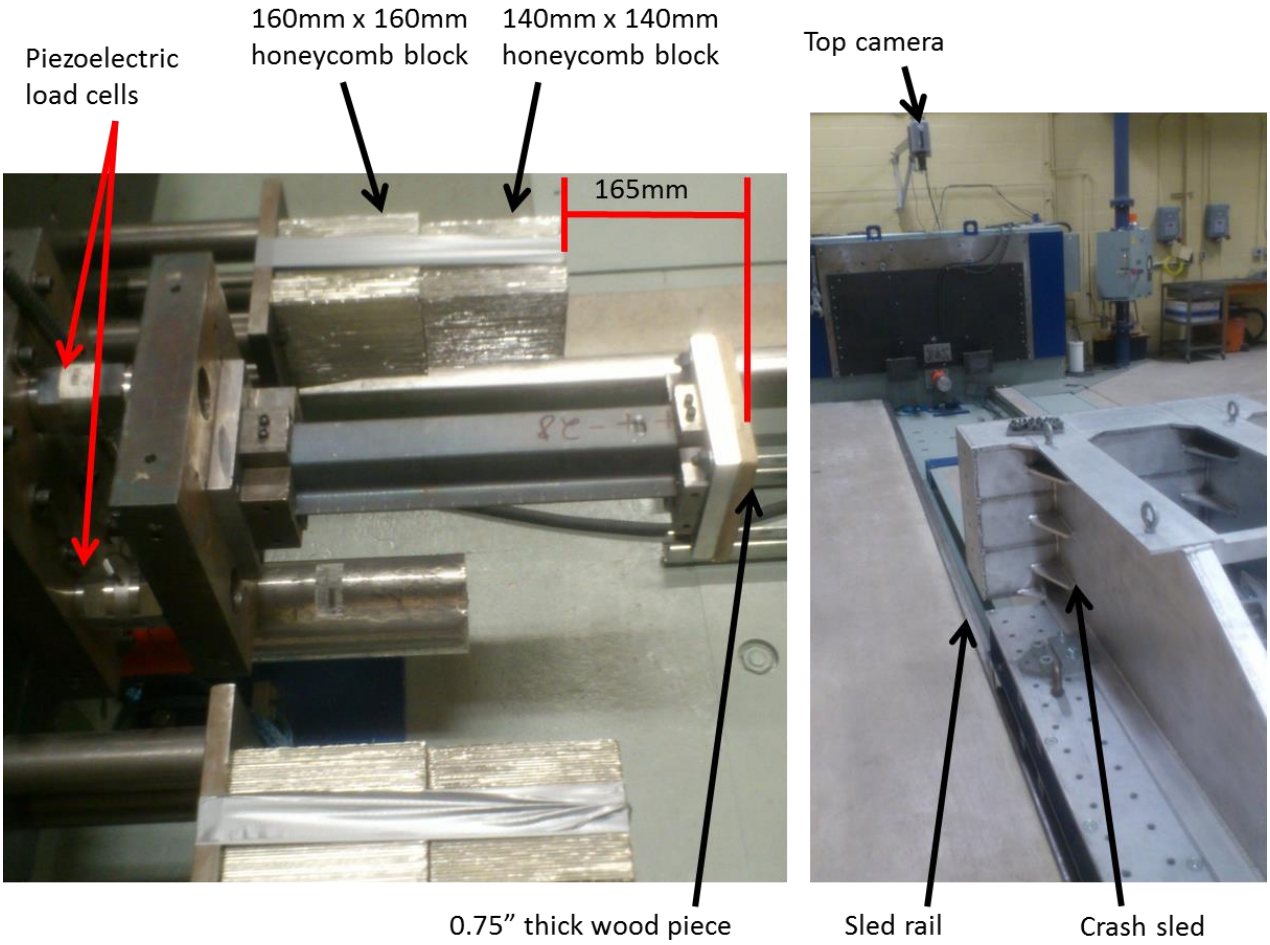

Figure 27. Setup for the dynamic crush tests

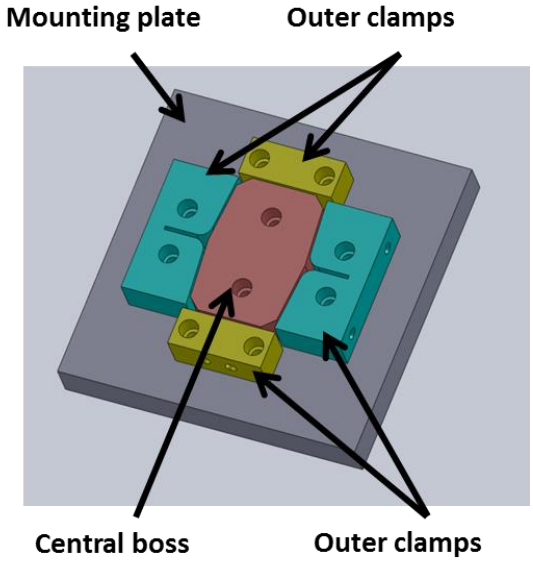

Figure 28. The clamps and boss that were used to mount the crush specimens

Plascore 5052 honeycomb with a crush strength of 3.69 MPa (535 psi) [70] was mounted on both sides of the crush specimen to stop the sled after the majority of the crush distance was consumed (shown in Figure 27). The pre-honeycomb crush distance for all dynamic tests was 165 mm.

Two stacks of honeycomb were mounted 70 mm above the base of the sled; one on each side of the crush specimen. Each stack contained two blocks of honeycomb, configured in a pyramid-like pattern. The first block in the stack measured 140 mm x 140 mm, with a length of 200 mm. The second block measured 160 mm x 160 mm with a length of 200 mm. The pyramid pattern was employed to ensure that the two blocks engaged with each other during impact, instead of buckling against each other.

Three 120 kN capacity piezoelectric load cells, mounted behind the supporting plate of the crush specimen, measured the force exerted onto the specimen by the sled. The total force applied by the sled onto the parts was equal to the sum of the forces measured by each individual cell. The load cells were placed in a triangular pattern, 233 mm away from each other (also seen in Figure 27). The sampling rate used to acquire the load cell data was 10,000 data points per second.

The crash sled contained two accelerometers mounted on it, one on each side. The accelerometers measured the deceleration experienced by the sled during crash. The sampling rate for these accelerometers was the same as the piezoelectric load cells, which was 10,000 data points per second. The displacement of the sled was calculated by double-integrating the deceleration data obtained from the accelerometers.

The crush experiment was recorded using two high-speed Photron SA4/5 digital cameras, with a frame rate of 7500 frames per second. The first of these cameras was mounted above the specimen (shown in Figure 27) and the second was mounted on the side. Snapshots taken from each camera can be seen in Figure 29. The two data acquisition systems (the piezoelectric load cells and the accelerometers) as well as the high-speed cameras were activated by a laser trigger that was located on the rails of the sled (shown in Figure 30). During a dynamic crush test, once

the sled crossed the trigger, the data acquisition was turned on for two seconds, which was sufficient to capture the experimental event.

Figure 29. Views from both cameras shown prior to a dynamic crush experiment

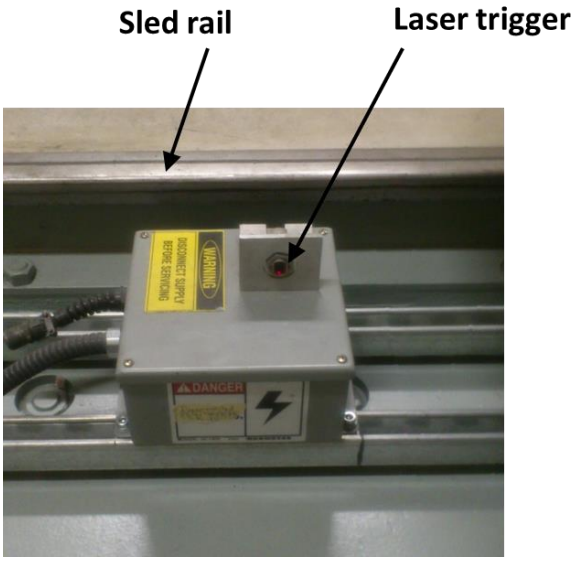

Figure 30. The data acquisition trigger, located on the rails of the sled

2.7 Quasi-Static Crush Setup

The setup for the quasi-static experiments in this work is shown in Figure 31. A hydraulic actuator applied force to the end of the axial crush specimen. The actuator was operated under closed-loop displacement control, imposing a constant velocity of 0.508 mm/s (0.02 in/s) onto

the end of specimen for a total stroke of 190 mm. The velocity of 0.508 mm/s corresponded to a nominal strain rate of one thousandth (0.001 s^{-1}).

The specimen was mounted using the same clamp and boss design as in the dynamic crush experiments. The plate on the top of the crush specimens was bolted directly to an adapter which was attached to the hydraulic actuator. The plate on the bottom of the crush specimens was clamped down onto the base of the frame where the hydraulic arm was mounted. The force and displacement data were obtained from the load cell using a Labview program that had a sampling rate of 4 points per second. The entire quasi-static test took 6 minutes, 14 seconds to complete, and therefore this sampling rate was sufficient for the experiment. The experiment was recorded using a Nikon D3200 digital camera mounted onto a tripod.

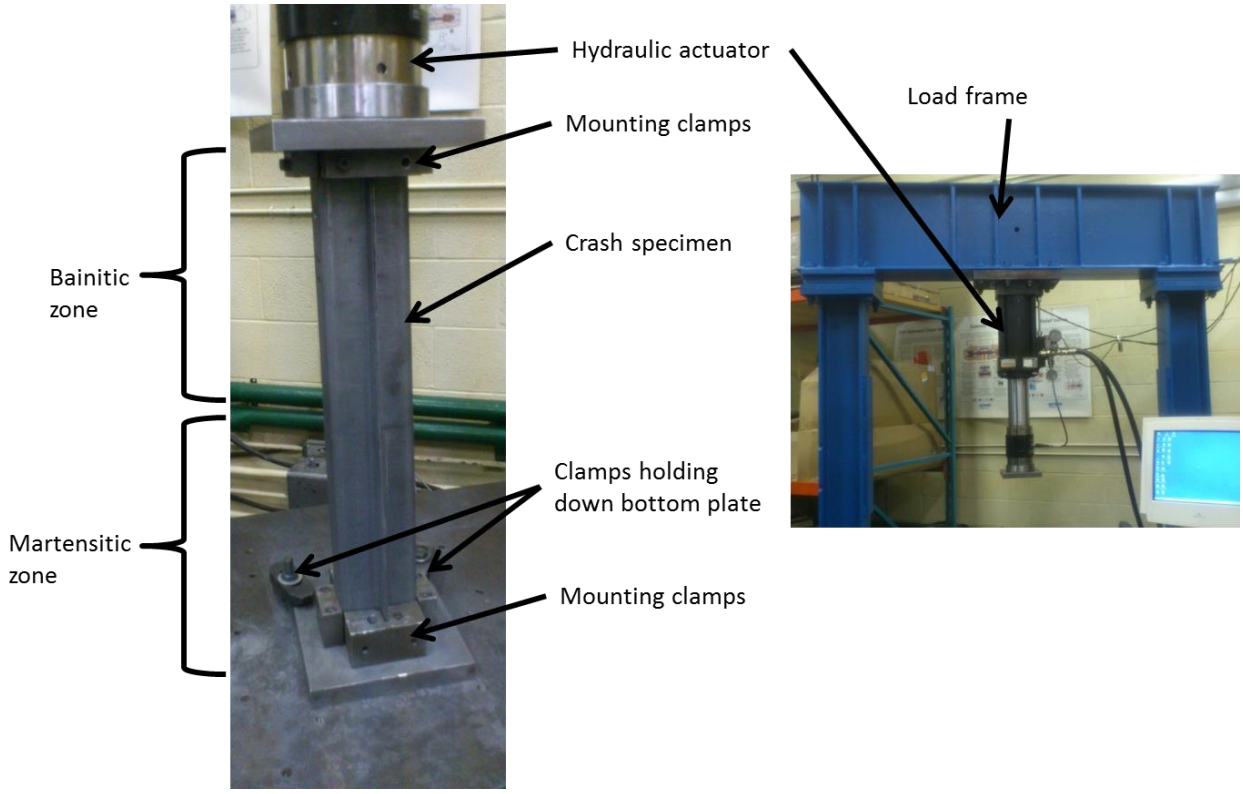

Figure 31. Setup for the quasi-static tests

3. Numerical Models – THS and Crash

All numerical modelling in this work was performed using the commercial LS-Dyna R7.0 software package, which is very commonly adopted by industry to model hot stamping vehicle crashworthiness. The subsequent sections in this chapter will describe the approach taken in this thesis to model the THS and crash (both quasi-static and dynamic) experiments. Section 3.1 describes the THS models, while section 3.2 describes the crash models.

3.1 Modelling the THS Process

3.1.1 Overview of THS Modelling Strategy

The THS model was broken into four separate stages: Transfer; Forming; Quenching; and Cooling, all of which are modelled in order to capture the material response. These stages are outlined in sections 3.1.4 to 3.1.7.

A coupled thermo-mechanical solver, in which both a mechanical and thermal solver run in parallel, was utilized for each of the four stages. The mechanical solver determined strains, stresses and deformations in each element. The thermal solver determined temperature profiles and heat flow in each node and element. The thermal properties determined by the thermal solver were passed on to the mechanical solver, which used them to generate thermal stresses and strains, as well as to predict micro-hardness in the blank based on cooling rates.

The THS process in this work was modelled using a half-symmetry assumption. Dividing the THS process into stages allowed for different levels of mass scaling in each stage, which in turn optimized the total run-time of the full THS process simulation (further discussion on mass scaling is provided in section 3.1.5). Furthermore, the subdivision of the THS into stages allowed some simulations to run explicit solvers while others ran implicit solvers, which also allowed for the optimization of the run-time. The resulting strains, stresses, hardness values and micro-structural compositions in each of these stages were input as starting conditions for the subsequent stage, using the “dynain” file outputted by LS-Dyna.

The final as-formed condition in the THS model was used as the initial condition for the crash model, described in the next section.

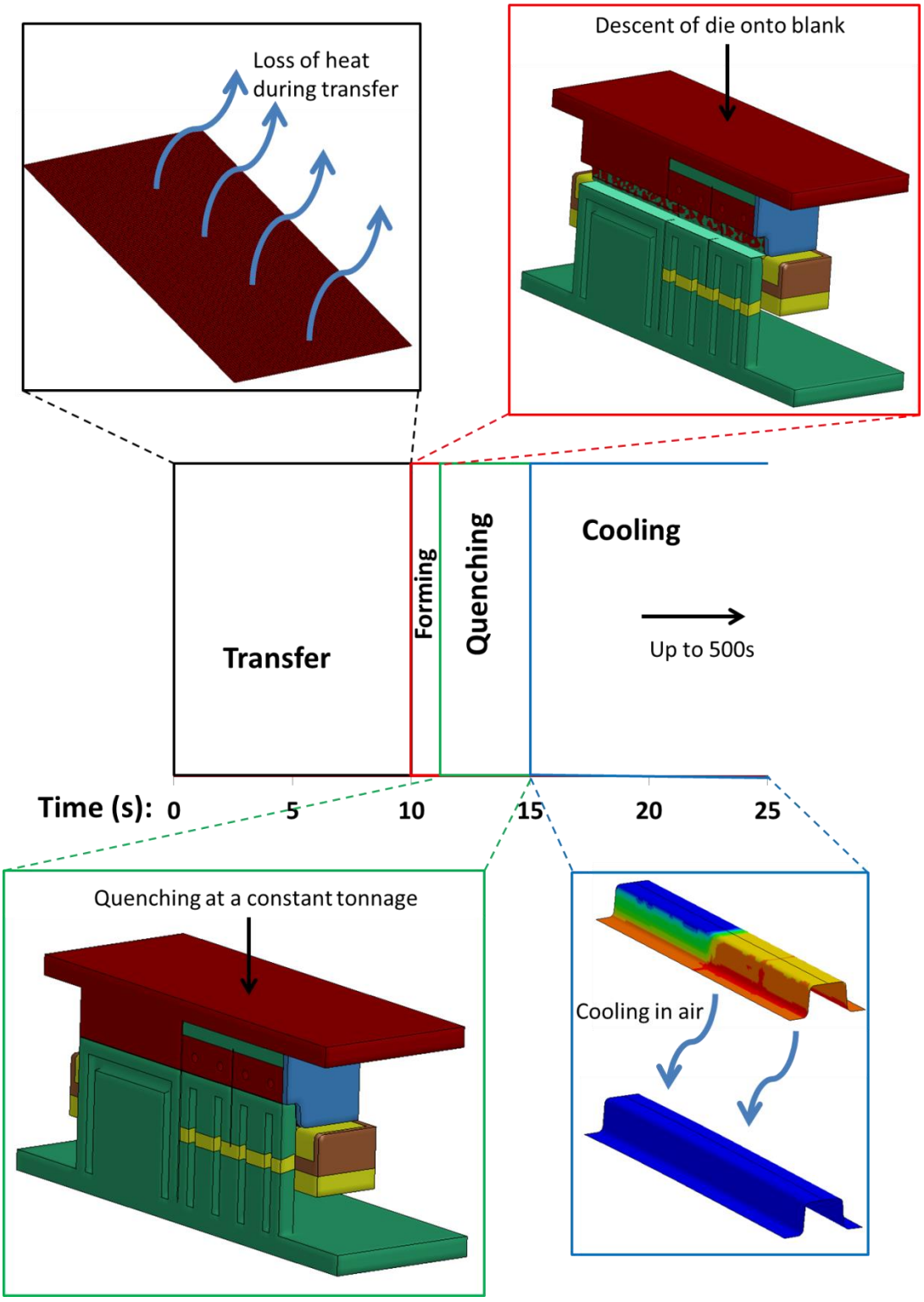

Figure 32. Overview of each stage of the THS model

3.1.2 Mesh, Element Formulations and Material Models for the Tooling Components

The axial crush tooling was modelled using a rigid, non-deformable mechanical material model and an isotropic thermal model, with standard properties of steel shown in Table 3 and the properties of ZIRCAL-95 insulation shown in Table 4. The tooling used a combination of brick and tetrahedron elements with a mesh size of 10 mm, which is shown in Figure 33. The element formulation used for the tooling in the thermal solver was a fully integrated quadratic scheme.

Table 3. Properties of steel used in this work, taken from **[71]** and **[72]**

Property	Value
Density	7890 kg/m^3
Young's Modulus	200 GPa
Poisson's Ratio	0.3
Specific Heat	0.519 kJ/kg-K
Thermal Conductivity	37.7 W/m-K

Table 4. Properties of ZIRCA-95 insulation used in this work, taken from **[69]**

Property	Value
Density	1400 kg/m^3
Specific Heat	11.72 kJ/kg-K
Thermal Conductivity	0.6 W/m-K

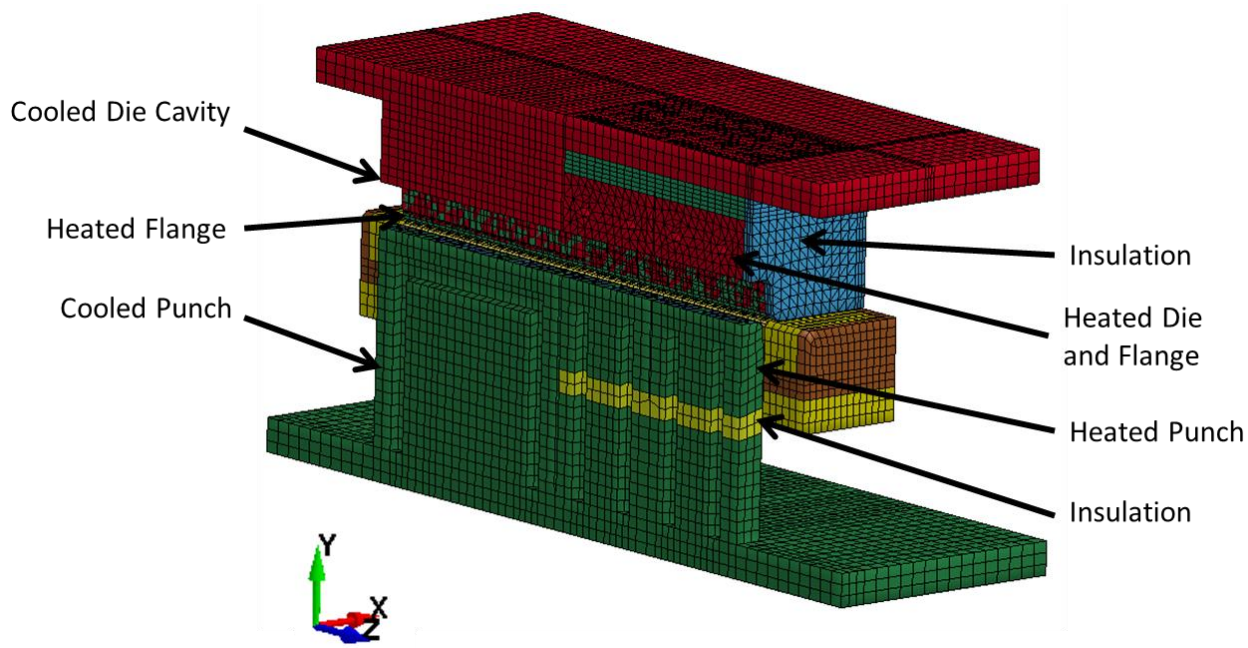

Figure 33. Mesh pattern used for to model the axial crush tooling

3.1.3 Mesh, Element Formulations and Material Models in Blank

Due to the half symmetry employed in the forming models, the dimensions of the blank were 100 mm x 590 mm (instead of 200 mm x 590 mm), with a constant mesh size of 2.5 mm. The blank was modelled using 2-point quadrature (in-plane) shell elements (also called fully integrated shell elements). Both the mechanical and thermal solvers used this formulation with seven integration points through the shell thickness.

In all stages of the THS model, the blank was modelled using an isotropic thermal material model for the thermal aspect of the simulation. The properties used in this model were identical to those of the tooling, which are outlined in Table 3. For the mechanical aspect of the simulation, the Åkerström material model [62] described in section 1.4 was used. A Young's modulus of 100 GPa was specified and a Poisson's ratio of 0.3. The density varied in each stage, depending on the level of mass scaling employed. Details on the mass scaling approach will be given in section 3.1.5.

As mentioned in section 1.4, the Åkerström model predicts the phase compositions in each element, which it then uses to determine Vickers hardness. To be able to determine these phase compositions, LS-Dyna requires activation energies for each phase. These activation energies are

used by the model to determine the temperatures at which each phase will begin to form (called "start temperatures"). As long as an element remains above the start temperature for a respective phase, LS-Dyna will set the percent volumetric fraction of that phase to zero. It will only include the calculation for the phase once the temperature in an element has decreased below the start temperature for that particular phase.

The activation energies for ferrite, pearlite and bainite were set to 94.1 kJ, 143.8 kJ and 125.0 kJ, respectively, as determined by George et al. [73] to best match Vickers hardness data on as-quenched Usibor® 1500P published by Bardelcik et al. [68]. Using these activation energies, LS-Dyna calculated the start temperatures for ferrite, pearlite, bainite and martensite to be 822˚C, 720˚C, 573˚C and 404˚C, respectively.

In addition to start temperatures for each phase, the Åkerström model is able to theoretically predict the Vickers hardness for each phase using formulas provided in [59, 60, 74]. It was determined in this work, however, that the Vickers hardness obtained by these formulas did not match the measured values of hardness. Therefore, a customized option available in LS-Dyna, called the "TEMPER option" was activated. This option allowed for the manual definition of Vickers hardness in the bainite and martensite phases as a function of temperature, overriding the formulas provided in [59, 60, 74]. The final Vickers hardness was then calculated using the same weighted average shown in eq. (2) in section 1.4:

$$HV = X_b HV_b + X_f HV_f + X_p HV_p + X_m HV_m \tag{2}$$

where X represents the volume fraction of a particular phase, HV represents the Vickers hardness of a particular phase, and the subscripts b, p, f and m denote bainite, pearlite, ferrite and martensite, respectively.

The hardness vs. temperature curves input to the numerical model are shown in Figure 34 and Figure 35 for bainite and martensite, respectively. LS-Dyna does not have an option to enter a hardness vs. temperature curve for ferrite. These curves were provided by the Livermore

Software Technology Corporation [75]. The critical cooling rate was set to 2.0s and the sampling rate for temperature rate monitoring was set to 0.5s.

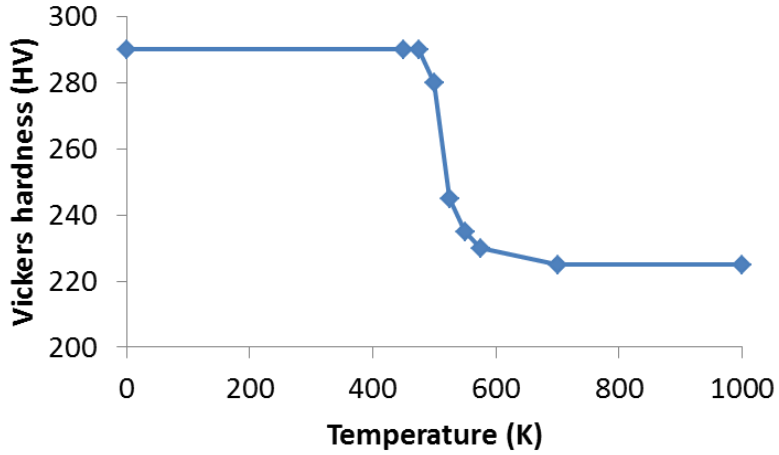

Figure 34. Vickers hardness vs. temperature curve for bainite

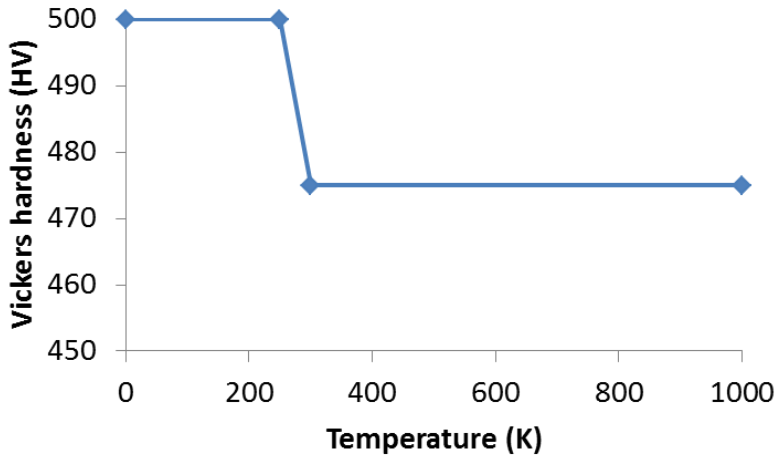

Figure 35. Vickers hardness vs. temperature curve for martensite

The final, critical aspect of the Åkerström model, as implemented in LS-Dyna, was the ability to scale the abovementioned activation energies as a function of effective plastic strain. As Bardelcik et al. [68] observed, the CCT diagram for Usibor® 1500P (shown in Figure 2 in section 1.2) "shifts" to the left proportionally to the amount of plastic strain in the material. In other words, higher plastic strain means that ferrite, pearlite and bainite form more easily (i.e., at lower activation energies). To account for this, the activation energies were scaled as a function of plastic strain, using the scaling factors determined by George et al. [73] for the material

considered in the current research. Table 5 and Table 6 show the activation energy scaling factors uses for ferrite/pearlite and bainite, respectively.

Table 5. Scaling factors used for the activation energy of ferrite/pearlite

Effective Plastic Strain	Scaling Factor
0	1
0.2	0.491
0.5	0.491

Table 6. Scaling factors used for the activation energy of bainite

Effective Plastic Strain	Scaling Factor
0	1
0.2	0.958
0.5	0.958

3.1.4 Model Parameters – Transfer Stage

The first stage of the THS mode, the transfer stage, modelled the heat loss experienced by the blank while being moved from the oven into the press, for a duration of 10s. The goal of this stage was to obtain the temperature distribution in the blank at the start of the forming process, and also to determine any changes in phase composition during this time.

3.1.4.1 Mechanical Formulation

An implicit solving scheme with a maximum allowable time step of 0.5s was used for the mechanical solver in this stage. No mechanical loads or boundary conditions were imposed, other than those resulting from the half symmetry assumption. No mass scaling was employed for this stage either (i.e., a density of 7830 kg/m^3 was specified).

3.1.4.2 Thermal Formulation

The thermal formulation adopted a symmetric direct solver with a relative convergence tolerance of 10^{-4}. A Crank-Nicolson scheme (implicit with respect to time and explicit with respect to space) was employed by the solver, using a thermal time step of 0.5s. In terms of thermal boundary conditions, an initial temperature of 930˚C was specified for all nodes in the blank.

Heat loss due to convection and radiation were modelled. The heat transfer coefficients (HTCs) and radiation factors used in the model are shown in Table 7 and Table 8, respectively, as a function of temperature. The HTCs and radiation factors were obtained from George [76], who obtained them through a numerical fit.

Due to the fact that both the HTCs and radiation factors were approximations, and not based on any experimental work, they added a high level of uncertainty in the THS models. The ramifications of this were not very significant in the transfer stage of the THS model, since the primary goal of this stage was to determine the actual temperature in the blank at the start of forming. As long as the austenite phase in the pre-formed blank did not begin to decompose during this stage, the approximations in the thermal boundary conditions were assumed to not profoundly affect the THS model.

Table 7. HTC as a function of temperature, obtained from **[76]**

Temperature (K)	HTC (W/m^2-K)
100	4.93
302	4.93
502	12.23
702	13.38
1102	13.70
1502	13.37

Table 8. Radiation factor as a function of temperature, obtained from **[76]**

Temperature (K)	Radiation Factor (W/m^2K^4)
0	0
100	0.5
373	0.5
648	0.65
873	0.7
1200	0.7
1300	0.7

3.1.5 Model Parameters - Forming Stage

The forming stage modelled the descent of the die onto the punch, forming the blank between the tooling surfaces (i.e., the main forming process). The duration of the forming stage was 1s. This stage of the model was critical since this is where most of the plastic strain in the blank was induced. The plastic strain is a key parameter in determining the final micro-hardness values in the part (explained in section 1.4).

3.1.5.1 Mechanical Formulation

An explicit solver was used for the mechanical portion of the forming simulation. The explicit solver in LS-Dyna uses the Courant stability criterion to determine the maximum allowable time step size in the simulation. The Courant stability criterion states that the maximum allowable time step must be no greater than the time it takes for a sound wave to travel through the smallest element in the FEM. This stability criterion results in very small time steps, which are often on the order of magnitude of 10^{-9}s. The simulation runtime, therefore, tends to be very high.

In order to reduce the total runtime of the simulation, a technique called mass scaling was employed. In this technique, the density of the material in the model is scaled up. Since sound waves travel faster through denser materials, the maximum allowable time step as determine by the Courant criterion increases substantially when mass scaling is employed. For this reason, the density of the Usibor® 1500P was scaled up in the forming and subsequent stages of the THS model.

There is, however, an upper limit to the amount of scaling that can be applied to the density of a material. If a scaling factor that is too large is applied, inertial effects due to the added mass can become significant in the simulation, and they can significantly alter the results of the model. This scaling factor can be very high in problems that involve negligible movement, since inertial effects are almost non-existent in such cases. However, for problems where dynamic effects must be considered, inertial effects can be very significant. Therefore, in such problems, a scaling factor that speeds simulation runtime without adding undesired physical effect must be applied.

Due to the fact that the blank moved at a fairly rapid speed in the forming stage, a high mass scaling factor could not be applied to speed up the simulation in the forming stage of the THS models since inertial effects of the blank would become significant. Therefore, a scaling factor of only 100 (i.e., a material density of 783,000 kg/m^3) was applied. This resulted in a time step 5.4 μs instead of 540 ns.

In terms of mechanical boundary conditions, the punch was constrained from moving in all directions. An upper limit on velocity was imposed for the binder limit of 110 mm/s and the die motion was prescribed in terms of a sinusoidal variation in velocity with respect to time, as is plotted in Figure 36. The sinusoidal variation was applied to allow for a gradual build-up in the speed of the blank, and thereby reduce inertial effects.

A penalty function-based surface-to-surface contact algorithm [64] was defined between the blank and binder, the blank and punch, and the blank and die. In all cases, a coefficient of friction of 0.4 was used, based on experiments done by Yanagida and Azushima [21].

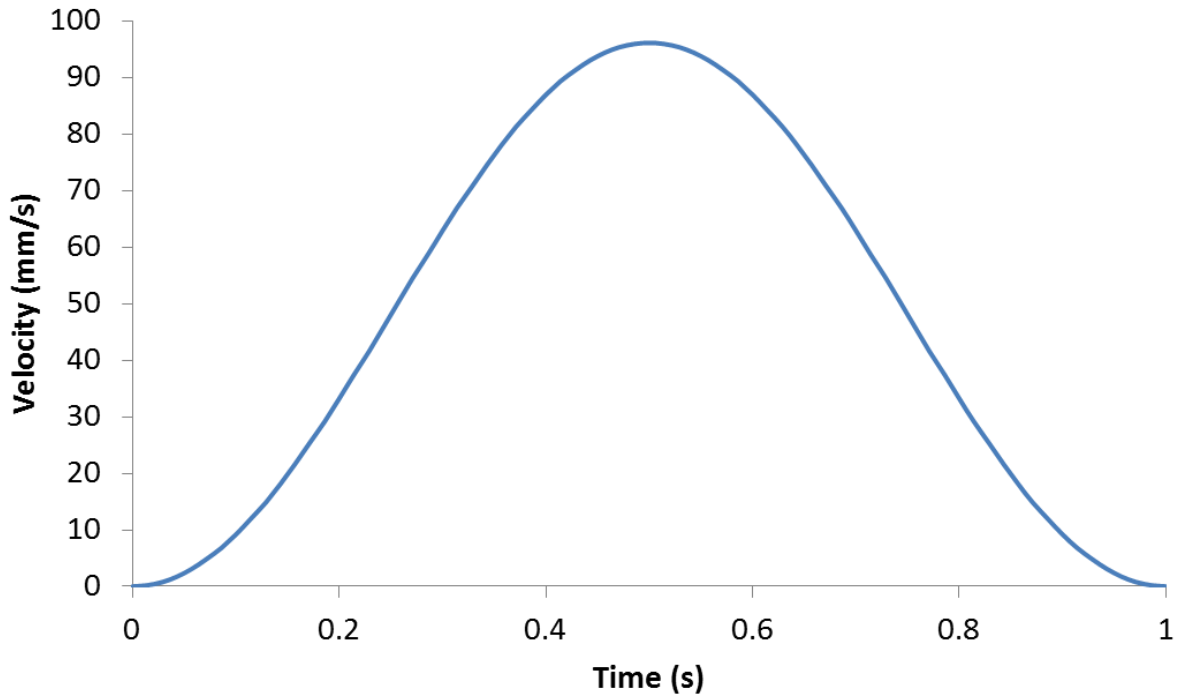

Figure 36. Sinusoidal velocity profile imposed onto the punch in the forming stage of the model

3.1.5.2 Thermal Formulation

The thermal solving scheme used in the forming stage was the same as the transfer stage. The only difference was that a maximum thermal time step of 0.02s was used instead of 0.5s. To model the temperature distribution in the tooling of the blank, heat fluxes were defined in the areas of the tooling where cartridge heaters were inserted in the actual die.

The heat fluxes used in different zones of the tooling to achieve the desired steady state temperatures are shown in Table 9 for all four types of parts. Note that the zone numbers used in Table 9 correspond to the zone numbers that were outlined in Figure 13 in section 2.2. These values were determined by running a steady state thermal analysis in LS-Dyna. A trial and error approach was taken until the combination of heat fluxes inputted into the model yielded the desired temperature in the tooling.

To model the flow of chilled water through the cooled section of the tooling, a temperature boundary condition of 12˚C was imposed on the nodes where water coolant flowed. Convection and radiation boundary conditions were applied on the outer surface of the tooling components to model heat loss to the outer surroundings of the tooling. The HTC and radiation factors used here are shown in Table 7 and Table 8.

Table 9. Heat fluxes (W/m^2) in the tooling for each type of part

Zone(s)	Fully Cooled	Single Soft Zone 400˚C	Single Soft Zone 700˚C	Graded Soft Zone
1 & 2	0	13.5	28	27
3 & 4	0	20	28	35
5	0	13.7	25.6	5
6	0	15.1	25.2	25
7	0	16.2	26	8
8	0	12	24.1	22.5
9	0	9.4	26	8
10	0	11	12	8
11 & 12	0	11	30	15

The final aspect of modelling the forming stage of the THS process was the definition of thermal contact between the blank and tooling, and between different zones of the tooling. Thermal contact was activated if the gap between the blank and tooling was less than 0.3 mm. Conduction was assumed to be the primary mode of heat transfer. The HTC between the tooling and blank was defined as a function of pressure, according to the numbers presented in Table 1 in section 1.4, as was done in [28].

Between different zones of the tooling, conduction via the air gap was assumed to be the primary mode of heat transfer. The HTC between different sections of the tooling was calculated by dividing the thermal conductivity of air by the gap between the two zones of the tooling. Since thermal conductivity depends significantly on the temperature of the medium, the temperature of the air gap between different zones of the tooling was assumed to be the average temperature between the temperatures in the two zones.

For example, in the *graded soft zone* scenario, the two heated punches had a temperature of 400˚C and 700˚C. The temperature in the air gap between these two zones was assumed to be 550˚C, which is the average. The thermal conductivity of air was, therefore, assumed to be 0.059 W/mK in this zone for the *graded soft zone* scenario. The thermal conductivities of air as a function of temperature were obtained from [72].

Using this approach, the HTC was calculated between the two heated zones of the punch and die, between the heated and cooled sections of the punch and die, and between the cooled die and heated flanges. The calculated HTC values, which were used in the THS models, are shown in Table 10.

Table 10. HTC values (underlined) between different zones of the tooling

Zone	**Air Gap**	***Fully Cooled***		***Single Soft Zone 400˚C***		***Single Soft Zone 700˚C***		***Graded Soft Zone***	
		Avg. Temp (˚C)	***HTC (W/m^2K)***	***Avg. Temp (˚C)***	***HTC (W/m^2K)***	***Avg. Temp (˚C)***	***HTC (W/m^2K)***	***Avg. Temp (˚C)***	***HTC (W/m^2K)***
B/w heated and cooled punch/die	3.5 mm	25	7.44	212	11.23	362	13.88	212	11.23
B/w heated zones of punch/die	2 mm	25	13.02	400	25.39	700	33.36	550	29.50
B/w heated and cooled flanges	2.5 mm	25	10.42	212	15.72	362	19.43	212	15.72

3.1.6 Model Parameters - Quenching Stage

The quenching stage modelled the four second duration in which the blank was held inside the die set at a certain tonnage. The thermal parameters in the quenching stage of the model were identical to the forming stage. Mechanically, both stages were also very similar, with only three differences.

The first difference was that, since the blank was not subjected to motion, inertial effects were not as prevalent here and therefore a mass scaling factor of 10^6 was applied to the blank. This resulted in a material density of 7.83×10^9 kg/m^3 in the blank and a time step of 0.525 ms instead of 525 μs. The second difference between the forming and quenching stages of the model was that instead of the die having a prescribed sinusoidal velocity, a prescribed load was applied onto the die. A load of 30 tons was applied (which was one-half of the actual 60 tons exerted by the press, due to half-symmetry employed in the models)

The third and final difference between the forming and quenching stages was that instead of having a maximum velocity imposed on it, the binder had a load of 17.2kN imposed on it, to model the effects of the nitrogen cylinders in the actual tooling. This load was equal to one-half of the actual load that the nitrogen cylinders applied, due to half-symmetry.

3.1.7 Model Parameters - Cooling Stage

The final stage of the THS model, the cooling stage, modelled the heat loss in the formed blank as it cooled in air (for a duration of 500s). The convective and radiative properties used here were the same as the Transfer stage (presented in Table 7 and Table 8). Furthermore, at the end of this stage of the model, the resulting Vickers hardness and final microstructural composition in the formed blank are predicted. An explicit mechanical solver, with mass scaling of 10^8 was used in conjunction with the same thermal solver as the previous stages.

A degree of uncertainty was present in this stage of the THS model, which was caused by the approximated HTC and radiation factors. In particular, the uncertainty around the HTC values meant that the rate of cooling experienced by the blank may not have been fully accurate. The inaccurate rate of cooling would have had an effect on the phase composition in the formed part, and consequentially, the micro-hardness as well.

3.2 Modelling the Crash Experiments

3.2.1 Overview of Crash Models

The process of transferring the forming simulation results into a crash simulation consisted of four steps:

1. "Reflect" the half-symmetry model from the final stage of the THS model to attain fully symmetry and assign material properties;
2. Introduce the fold initiator;
3. Mesh the spotwelds as beams and assign contact between spotwelds and the crush specimen;
4. Impose boundary conditions and initial or prescribed velocities, as required for the dynamic or quasi-static experiments.

The steps outlined above are detailed in sections 3.2.2 to 3.2.6. All elements in the crash simulations were modelled using the Belytschko-Tsay shell formulation with seven integration points through-thickness. Unlike the THS models, which used a coupled thermo-mechanical approach, the crash models only employed an explicit dynamic mechanical solver.

3.2.2 Step 1: Mapping from THS Models to Crash Models (Binning)

The basic approach in modelling both the dynamic and quasi-static crash tests was to take the output from the cooling stage of the THS model and use it as an input for the crash models. Since the THS models employed half-symmetry, the output from the THS models had to be "reflected" in the yz-plane to attain full symmetry (depicted in Figure 37). Furthermore, since the crash models required two formed parts that were joined together, the reflected part had to be reflected once more, in the *xz*-plane. This is also shown in Figure 37. The final meshed specimens in shown in Figure 38.

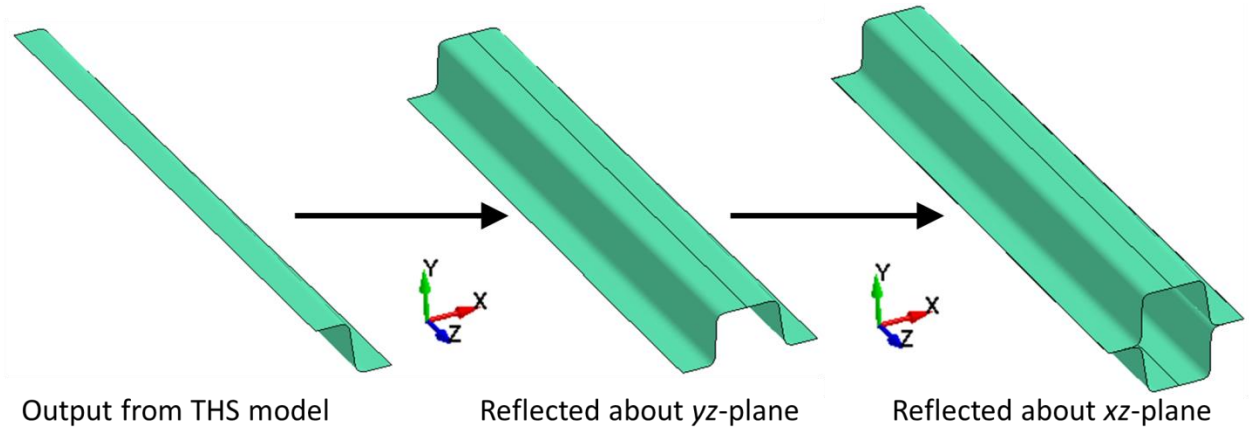

Figure 37. Setup of axial crush model from the THS model output

Once full symmetry was attained, the material properties in the crash specimen needed to be defined. This was done using the binning technique discussed in section 1.5. The stress, strain, microstructural composition and Vickers hardness predicted for each element in the THS simulation are output by LS-Dyna in a file called "dynain". A "re-mapping" program, developed by George [35], was used to read in the elemental properties from the dynain file output after the cooling stage of the THS model, and to sort each element into a bin based on its hardness value. Flow stress curves were generated at the weighted average Vickers hardness value.

Figure 38. Final mesh in the axial crush specimen

For the crash simulations, the three tailored parts were sorted into ten bins, while the *fully cooled* part was sorted into five bins. The range of micro-hardness for each bin for each type of part is shown in Table 11. The weighted average value of Vickers hardness is also shown and the material properties for the crash simulations were assigned based on this weighted average for all elements in each bin.

For the majority of the elements (bins), the TCM I model (section 1.5) [35] was used to assign the material stress strain response and strain rate sensitivity based upon the predicted hardness after forming. For elements within bins that contained more than 1% ferrite in volume fraction, the TCM II model (section 1.5) was used since it provides superior stress-strain predictions for softer, ferrite containing material, as shown by Bardelcik et al. [68]. Table 11 shows which bins used the TCM II constitutive model. Figure 39 shows three representative flow stress curves that

were obtained from the TCM I (bin 1 from the *fully cooled* and *single soft zone 400˚C* configurations) and TCM II (bin 2 from the *graded soft zone* configuration) constitutive models.

The element material property assignments or bins are shown for all four test cases in Figure 40, with each colour representing its own bin.

Table 11. Hardness range and average hardness (in parentheses) for each bin in the crash models. Bins using the TCM II model are bolded

Bin Number	Fully Cooled	Single Soft Zone 400˚C	Single Soft Zone 700˚C	Graded Soft Zone
1	456-462 (459.4)	252-275 (266.8)	**192-221 (203.7)**	**182-213 (199.5)**
2	463-468 (465.5)	276-299 (288.5)	**222-250 (243.7)**	**214-244 (227.0)**
3	469-474 (471.6)	300-322 (308.3)	251-279 (258.5)	245-275 (250.6)
4	475-480 (477.6)	323-345 (333.4)	280-309 (290.9)	276-306 (285.6)
5	481-487 (483.7)	346-368 (355.1)	310-338 (328.1)	307-337 (319.8)
6		369-391 (378.9)	339-367 (354.1)	338-368 (353.2)
7		392-415 (402.9)	368-396 (383.2)	369-399 (386.4)
8		416-438 (426.6)	397-425 (413.7)	400-430 (415.8)
9		439-461 (448.3)	426-455 (442.0)	431-461 (448.4)
10		462-485 (477.3)	456-484 (477.7)	462-492 (477.6)

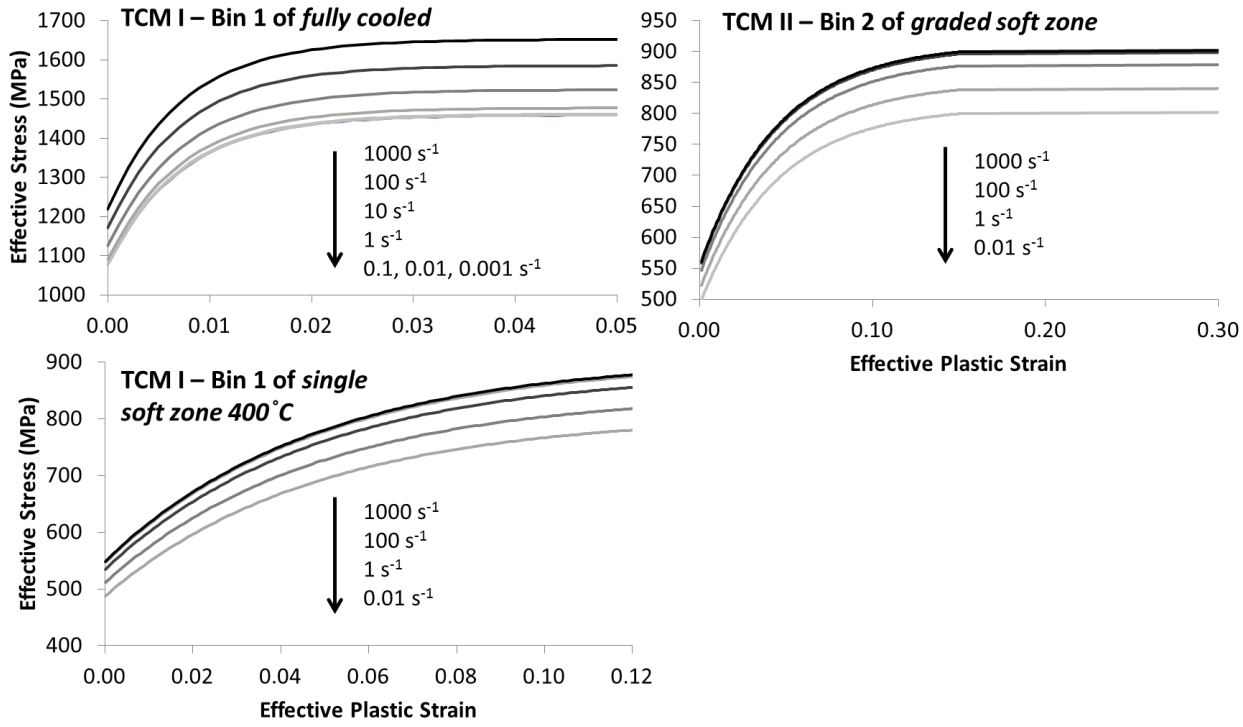

Figure 39. Flow stress curves obtained from the TCM I and TCM II models for two bins

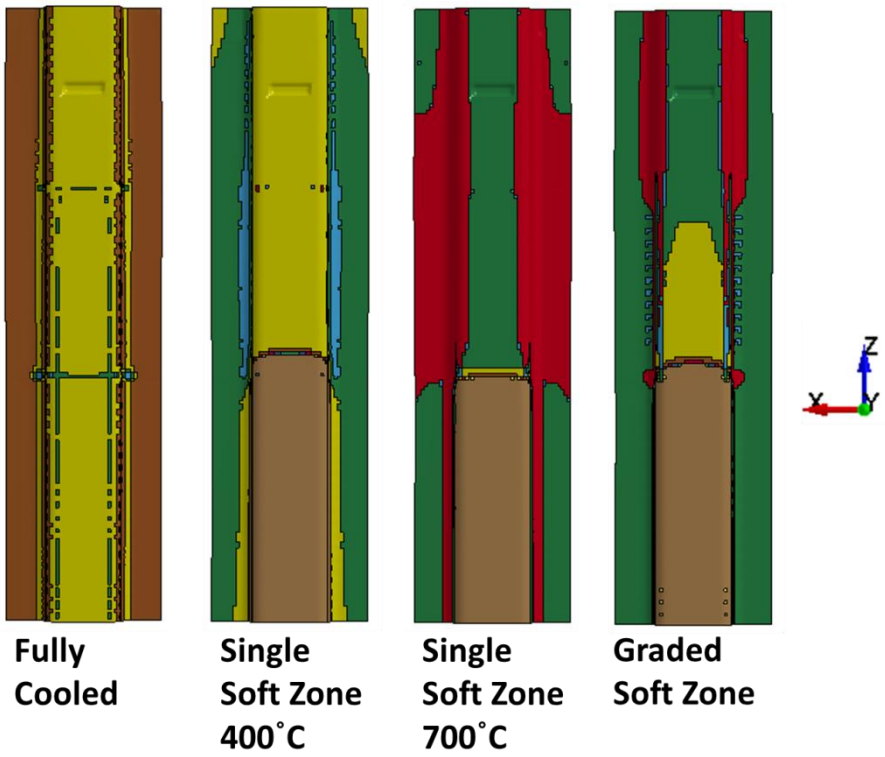

Figure 40. Final binned crash specimens for each of the four types of parts

3.2.3 Step 2: Inserting the Fold Initiator

Rather than simulating the forming of the dimpled fold initiators, the fold initiator in each crash specimen was simply introduced by displacing the nodes in the dimpled region, as shown in Figure 41. A total of twenty six (two rows of thirteen) nodes in total were displaced 4 mm in the *y*-direction. The initiator was placed 70 mm from the end of the specimen. This approach is approximate and fails to consider local work hardening and thinning in the fold initiator, but simplifies the model creation and does provide the necessary geometric discontinuity needed to control initiation of folding.

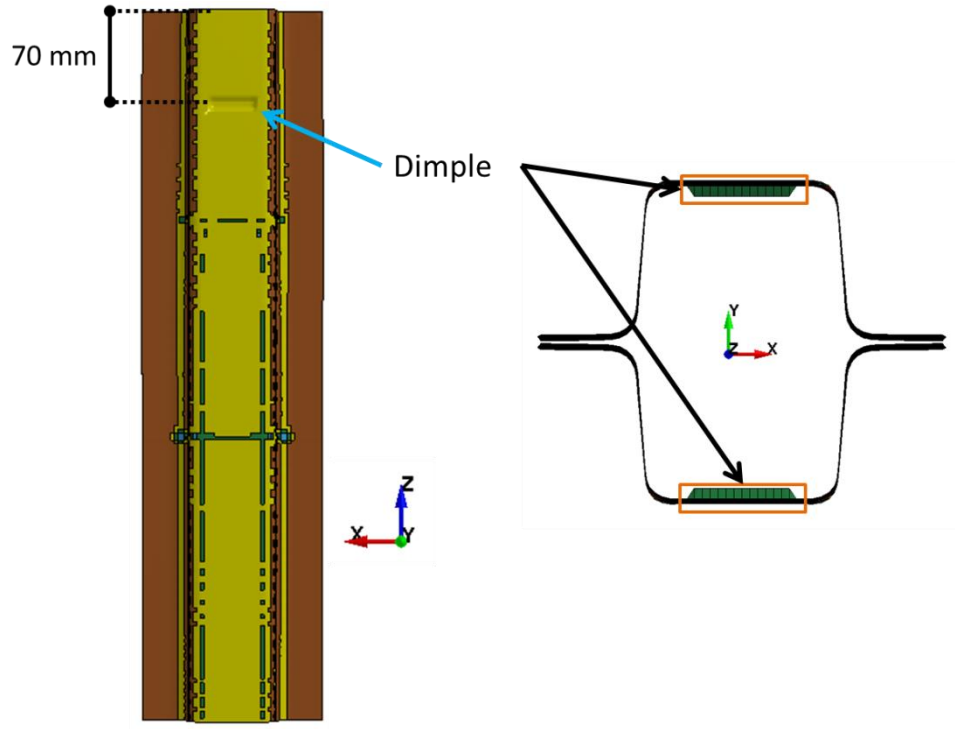

Figure 41. The modelling of the fold initiator

3.2.4 Step 3: Modelling the Spotwelds

Spotwelds were modelled as beam elements using the standard elastic properties of steel listed in Table 3. The spotwelds were connected to the formed specimens using the tied contact algorithm in LS-Dyna [64]. Just as with the experimental parts, welds were defined along the flanges at intervals of every 25mm (every one in ten elements). A failure criterion for the spotwelds was not included in this work, the ramifications of which are discussed in section 5.4. A visualization of the spotwelds in the crash models is shown in Figure 42.

3.2.5 Step 4: Boundary Conditions – Dynamic

To model the reduced length of the specimen during the dynamic test, 100 mm of elements were deleted from the model (or 40 rows of elements). The fixed end of the crash specimen was modelled by constraining a total length of 50 mm (twenty rows of elements) in all six degrees of freedom. No kinematic boundary conditions were defined on the bainitic/ferritic end of the part. Instead, the boss, outer clamps and mounting plate were modelled as rigid parts. This was done to allow for lateral movements and twisting in the specimen. The tied surface-to-surface contact algorithm in LS-Dyna was defined between the crash specimen and the boss and clamps. The defined boundary conditions as well as the boss and clamps around the crash specimen can be seen in Figure 43.

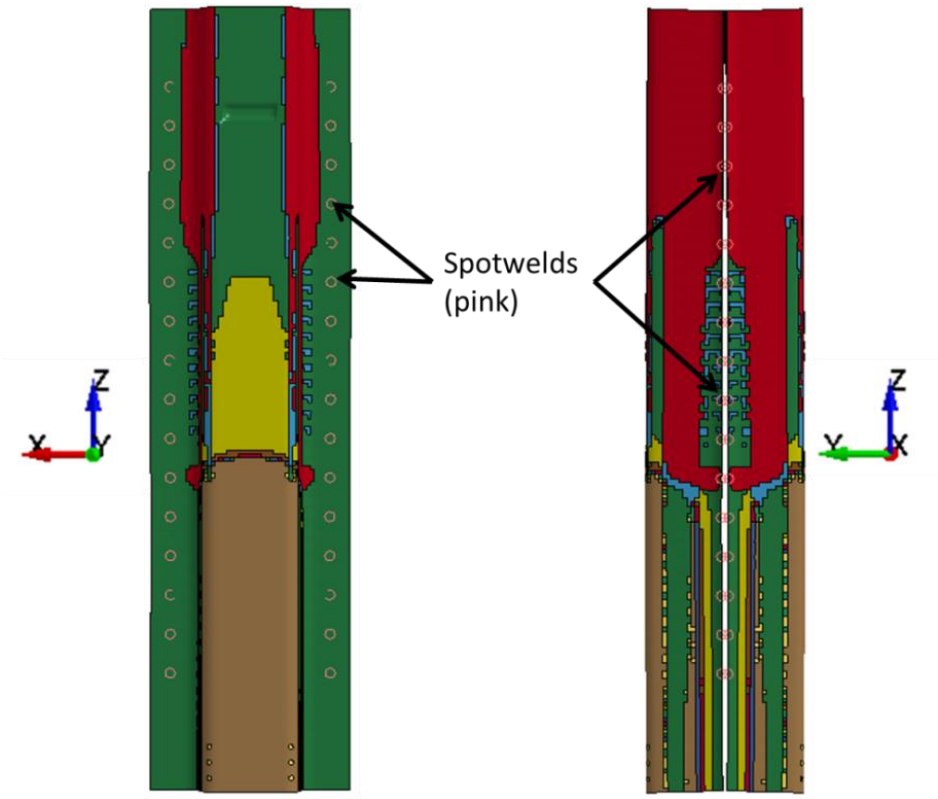

Figure 42. Diagram showing the spotwelds modelled along the flanges of the crash specimen

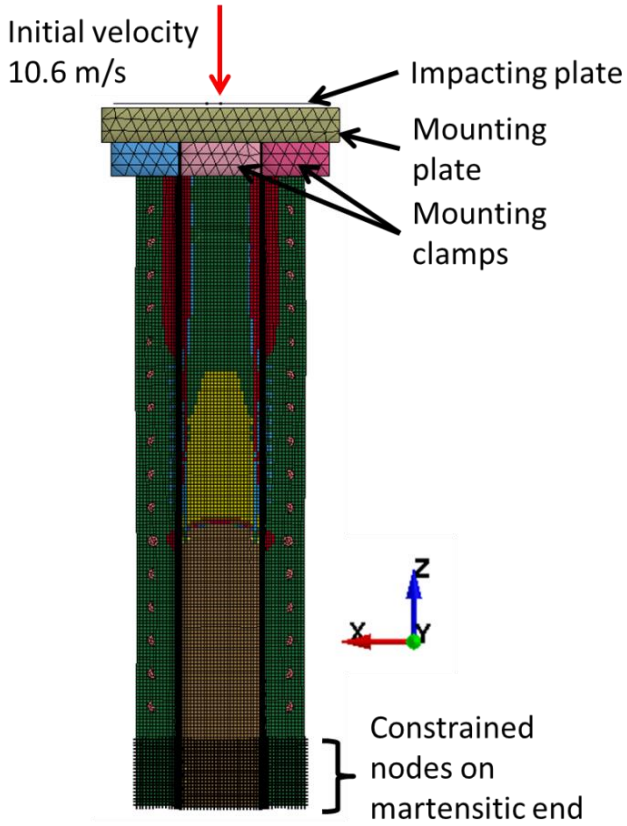

Figure 43. Setup of the dynamic crash model

The crash sled was modelled as a rigid impacting plate made of shell elements (also shown in Figure 43). A mass of 855 kg assigned to the impacting plate along with an initial velocity of 10.6 m/s to match the experimental conditions. The dynamic crash simulation was run for 0.03s. It should be noted that the honeycomb used in the actual experiments to stop the sled was not modelled.

3.2.6 Step 4: Boundary Conditions – Quasi-Static

The boundary conditions on the quasi-static models were the same as in the dynamic crash models, with only three differences. The first difference was that 100 mm of elements were not deleted from the crash specimen. The second difference was that the impacting plate had a constant prescribed velocity of 0.508 mm/s, instead of an initial velocity. The prescribed velocity more accurately modelled the hydraulic arm in the quasi-static tests.

The third difference between the quasi-static and dynamic crush model setups was that the quasi-static models employed time scaling. The prescribed velocity on the impacting plate was scaled

by a factor of 1000 to attain a value of 508 mm/s. To offset the strain rate effects that would arise from this, the strain rates on the flow stress diagram were also scaled by a factor of 1000. The time scaling on the prescribed velocity was imposed to speed up the total run-time of the quasi-static models.

3.2.7 Failure Criterion in the *Fully Cooled* specimens

A Generalized Incremental Stress-Strain Model (GISSMO) [64] was applied to the models of the *fully cooled* specimens to predict the significant amounts of failure that was observed in them. A failure criterion was not judged necessary for the other three rail configurations which did not exhibit significant cracking. The GISSMO model utilizes a curve of effective plastic strain at failure vs. stress triaxiality; this curve is shown in Figure 43. This failure data was obtained from experiments conducted by Ten Kortenaar [77], as part of task 4 of the broader Honda project that was outlined in section 1.6.

The curve shown in Figure 44 is a preliminary version of what will be a final failure criterion in the Honda project. Specifically, the magnitudes of failure strains at the plane-strain point (triaxiality = 0.58) are subject to change. Furthermore, the curve needs to be smoothed between the discrete points plotted in Figure 44. These changes to the curve will be made in the future and incorporated into the work outlined in this thesis.

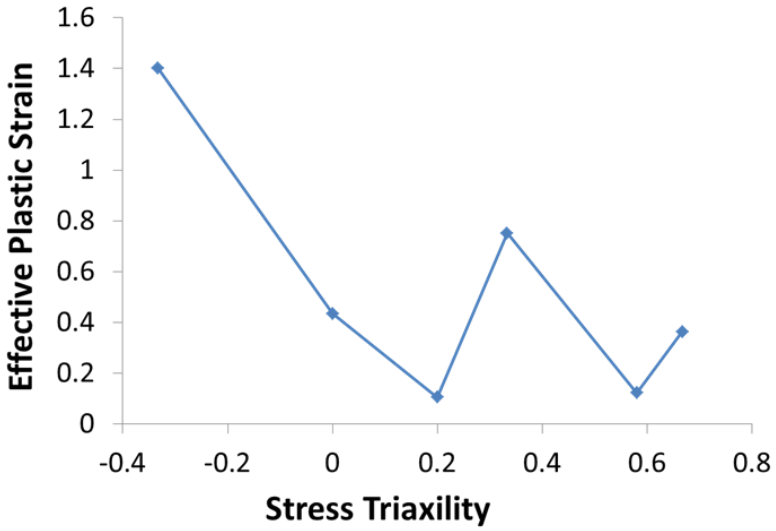

Figure 44. Failure curve used in the *fully cooled* crash model; failure data obtained from Ten Kortenaar **[77]**

4. THS and Micro-Hardness Results – Experimental and Numerical

This chapter presents the results obtained from the micro-hardness and material thickness measurements conducted on the as-formed parts and results from the THS models as well. To this effect, the measured hardness and material thickness values are presented and discussed first. Afterwards, the simulated temperature-time and effective plastic strain-time histories are analyzed and compared against the measured micro-hardness values. Next, the final, simulated material thickness in the as-formed blanks is shown and compared against measured thickness. Finally, the predicted Vickers hardness is shown and compared against the measured values.

4.1 Micro-Hardness and Material Thickness Measurements on as-Formed Parts

Figure 45 shows the average hardness profiles measured in the flange, wall and top section for each of the four types of parts formed (resulting in twelve plots). Hardness measurements were conducted on three parts from each of the four categories, at the same locations. Figure 45 also shows the material thickness measured in the part at the same location as the hardness measurement. In each plot, the solid lines represent Vickers hardness, plotted against the left axis, while the dashed lines represent material thickness, plotted against the right axis. The thick lines represent the average value of Vickers hardness (between the three measurements performed), while the thin lines represent the maximum and minimum values measured in the Vickers hardness at each location.

Section 4.1.1 discusses overall trends in the micro-hardness measurements. Section 4.1.2 talks about the variance in these measurements. Section 4.1.3 discusses the material thickness measurements.

4.1.1 Overall trends in Micro-Hardness Measurements

The curves depicting the average Vickers hardness in each of the twelve plots in Figure 45 clearly show that the formed parts exhibited tailored properties along their lengths. All three types of tailored parts were found to have a transition zone spanning approximately 70 mm.

Overall, these results in micro-hardness show that the forming technique and tooling design employed in this work were able to produce a formed rail that contained tailored properties across its length. Likewise, the results also show that the tooling was able to produce a part with no soft zone if the cartridge heaters in it were not turned on.

The micro-hardness measurements also establish that a part formed at a higher temperature will have softer micro-hardness properties. Based on Figure 45, the four types of parts can be ranked from hardest to softest as follows: *fully cooled, single soft zone 400˚C, graded soft zone* and *single soft zone 700˚C.*

The hardness profile in the side-wall and top section of the *fully cooled* part was uniform along its length. The Vickers hardness in the top section of the *fully cooled* part remained in the expected range for martensite throughout its entire length (ranging from 450 to 510 HV). The only exception occurred in the transition zone between the heated and cooled sections of the tooling, where the Vickers hardness dipped to 400-430 HV.

A similar trend was observed in the side-wall of the *fully cooled* part, which also remained in the martensitic range, except in the transition zone between the cooled and heated tooling. The flange in the *fully cooled* parts, however, exhibited hardness values corresponding to a mixed martensitic/bainitic microstructure.

In both *single soft zone* parts, the cooled region in the top section exhibited micro-hardness values in the expected range for martensite, while the heated region of the top section exhibited values corresponding to the bainitic (around 280 HV at 400˚C) and bainitic/ferritic (around 210 HV at 700˚C) range. Furthermore, the top section in the *single soft zone 700˚C* part was found to have softer properties in its heated zone than the heated zone in the top section of the *single soft zone 400˚C* part. This was the anticipated trend in the as-formed parts.

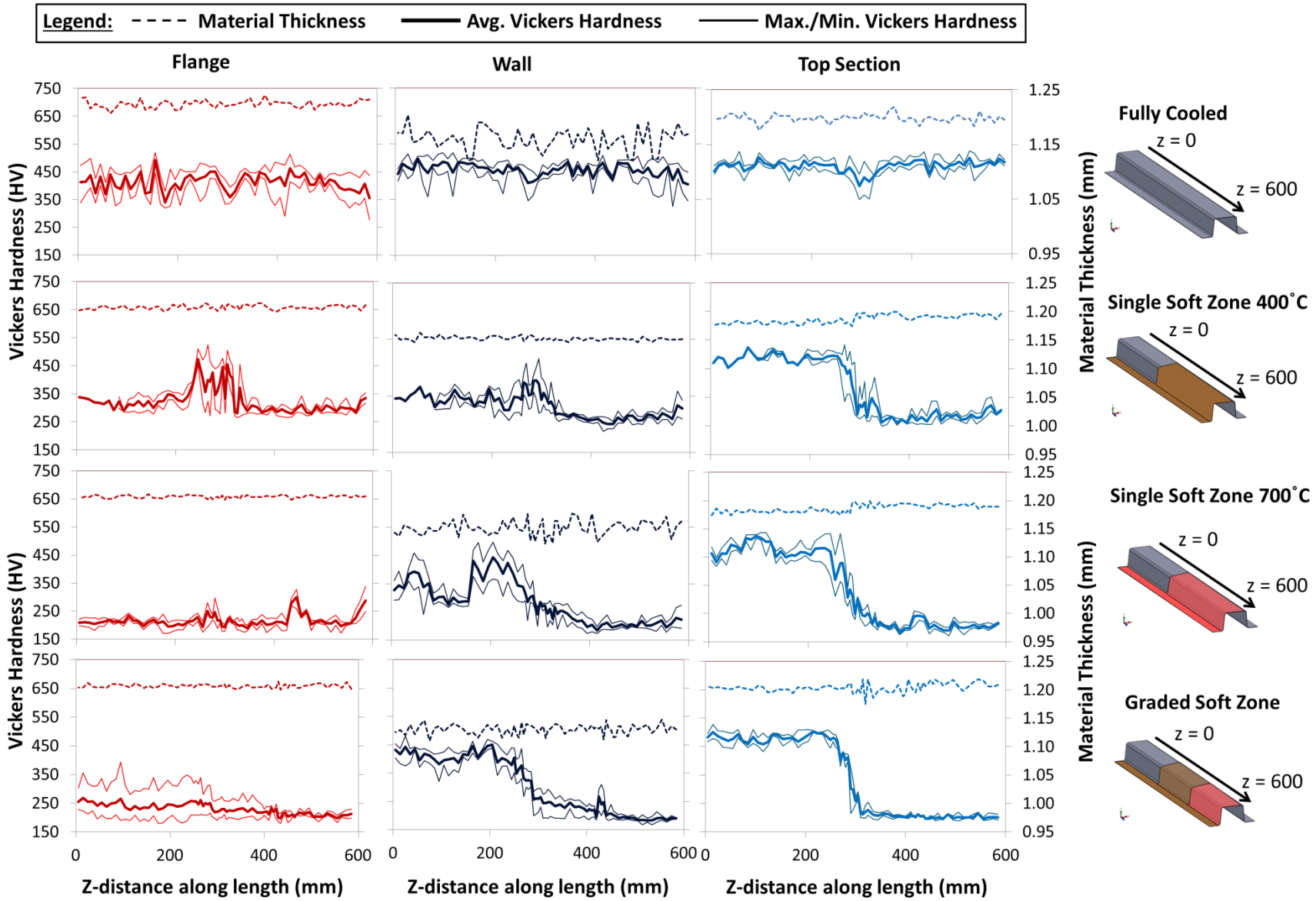

Figure 45. Hardness profiles along the axial direction of each hot stamped part in the flange, wall and top section

This tailoring trend observed in the top section of the *single soft zone* parts was also replicated in the *graded soft zone* part. However, the measured hardness profile in the top section of the *graded soft zone* part turned out to be very similar to that of the top section in the *single soft zone 700˚C* part. Only two zones of hardness were observed, instead of the expected three. This was most likely caused by the uneven shimming in the tooling for the *graded soft zone* configuration, as explained in section 2.2.

Similar to the top-sections, the side-walls in the *single soft zone* and *graded soft zone* parts also exhibited tailored properties, though they were not as pronounced as they were in the top section. The cooled region of the side-wall in the *single soft zone 400˚C* parts exhibited a hardness level of around 350 HV while the heated region exhibited around 260 HV.

The cooled region of the side-wall in the *single soft zone 700˚C* part exhibited a hardness of around 400 HV near the centre of the part and around 280 HV near the cooled edge of parts. The heated section exhibited a Vickers hardness of around 195 HV. The side-wall for the *graded soft zone* part contained three zones of Vickers hardness (430 HV, 230 HV and 185 HV), a result which ideally should have been observed in the top section as well.

The flanges in each of the three tailored types of parts exhibited soft properties throughout their entire length. This result is expected since the flange was formed at an elevated temperature across its entire length for the three tailored types of parts. Nevertheless, there was a slight dip in Vickers hardness when comparing the cooled half of the part to the heated half of the part, which can be attributed to the slight difference in cooling rates between the heated and cooled "halves" of the part. An interesting and more unexpected result was the fact that the flange in the *single soft zone 400˚C* parts experienced a large spike in Vickers hardness in and around the transition zone.

The significance of the tailored properties discussed thus far in the as-formed parts will be made apparent in Chapter 5, where the crash response of these parts is investigated.

4.1.2 Variance in the Micro-Hardness Measurements

In addition to the average Vickers hardness, Figure 45 also shows the scatter in hardness values in each of the twelve plots (i.e., the maximum and minimum values of Vickers hardness measured at each point). It is evident from these plots that the transition zone in the top sections of each of the four types of parts had much more scatter than the cooled and heated regions of the top section. The top sections were, nevertheless, the most consistent region of each part when compared against the side-wall and flanges. The average percent difference between the average hardness value and the scatter bands for the heated, cooled and transition regions in the flanges, walls and top sections of all four types of parts is presented in Table 12.

Table 12. Average percent difference between the average Vickers hardness and its scatter in the cooled (C), transition (T) and heated (H) zones of the flange, wall and top section regions of each type of part

Part Type	**Flange**			**Wall**			**Top Section**		
	C	T	H	C	T	H	C	T	H
Fully Cooled	8.49%	7.65%	8.34%	5.29%	5.17%	5.54%	3.01%	6.78%	3.52%
Single Soft Zone 400˚C	6.02	14.26	5.35	5.81	11.43	5.16	2.31	11.36	5.38
Single Soft Zone 700˚C	5.87	7.34	6.57	10.46	9.98	8.25	5.17	10.54	5.01
Graded Soft Zone	21.50	15.19	6.45	5.76	12.10	7.71	2.98	6.15	2.90

The side-walls in all four types of parts exhibited a lot of scatter. These large scatter bands in the can be attributed to uneven contact that the wall experienced during THS. There was no definitive way to control the contact pressure between the tooling and the side-wall, nor was there an accommodation in the tooling that allowed for the proper shimming of the side wall when the tooling was heated. These two factors combined made it difficult to accurately control the THS process parameters in the side-wall, which most likely resulted in uneven contact between the side-wall and tooling, leading to a large variance in properties in the side-wall, between each individual part and even axially in an individual part.

Likewise, the tooling also provided no way to shim the flange section of the tooling separately from the top section. This likely resulted in uneven contact between the flange and tooling, thereby causing a large scatter in its properties between different parts.

4.1.3 Trends in the Material Thickness Measurements

The dashed lines depicting material thickness in Figure 45 show that the material thickness in the top section of each type of part was always lower in the cooled sections of the parts than the heated sections of the parts. These trends observed in the thickness of the as-formed parts will be used to validate the THS numerical model results in section 4.5, in addition to the micro-hardness measurements.

The material thickness in the side-walls of all parts was very variable and inconsistent in the axial direction, similar to the micro-hardness. And just as with the micro-hardness, the high variability in the material thickness can likely be attributed to the uneven contact pressure between the side-wall in the formed part and the tooling. The material thickness in the flange displayed a fair level of consistency, between parts and in each individual part, except in the *fully cooled* parts. The variance in the material thickness in the *fully cooled* parts is, however, consistent with the level of variance observed in the Vickers hardness in the same parts.

4.2 Simulated Results - Temperature Profiles in Blank

Figure 46 shows the contour plots of the temperature distribution in the blank during different stages of the THS simulation. All four types of parts are shown at t=0s (beginning of transfer), t=10s (beginning of forming), t=11s (end of forming), t=15s (end of quenching) and t=515s (end of cooling).

By comparing the contour plots at t=11s and t=15s, one can conclude that the temperature histories of each type of part are very different from each other. This is confirmed in Figure 47, which plots the temperature-time histories of elements 271789 and 267069 (which are labelled in Figure 47) for the *fully cooled* and *single soft zone* parts. Since all types of parts have the same temperature at the start of the forming stage, the temperature history in the transfer stage was not plotted and t=0 in Figure 47 refers to the start of the forming stage.

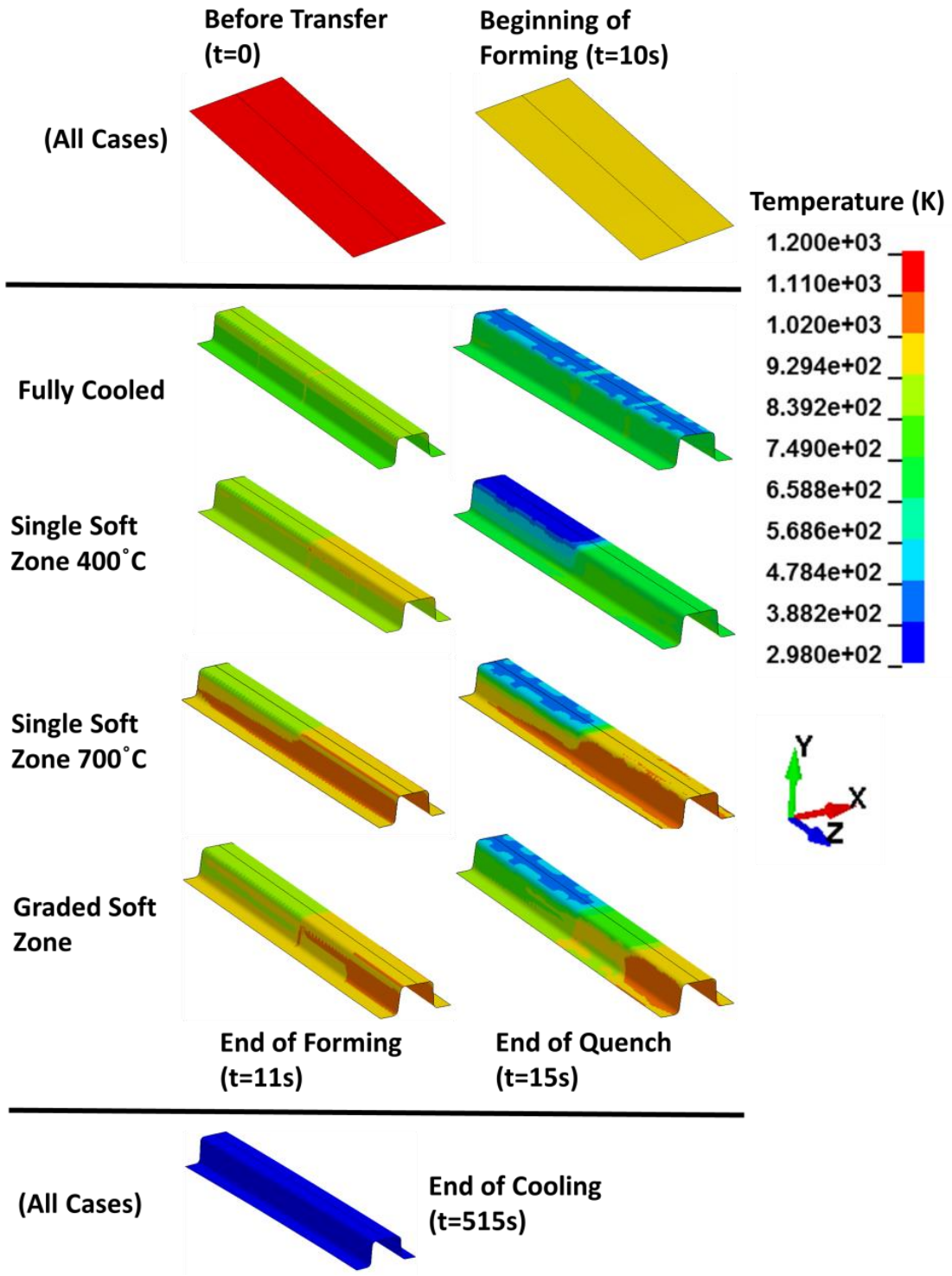

Figure 46. Contour plots showing temperature distribution in the blank during the THS simulation

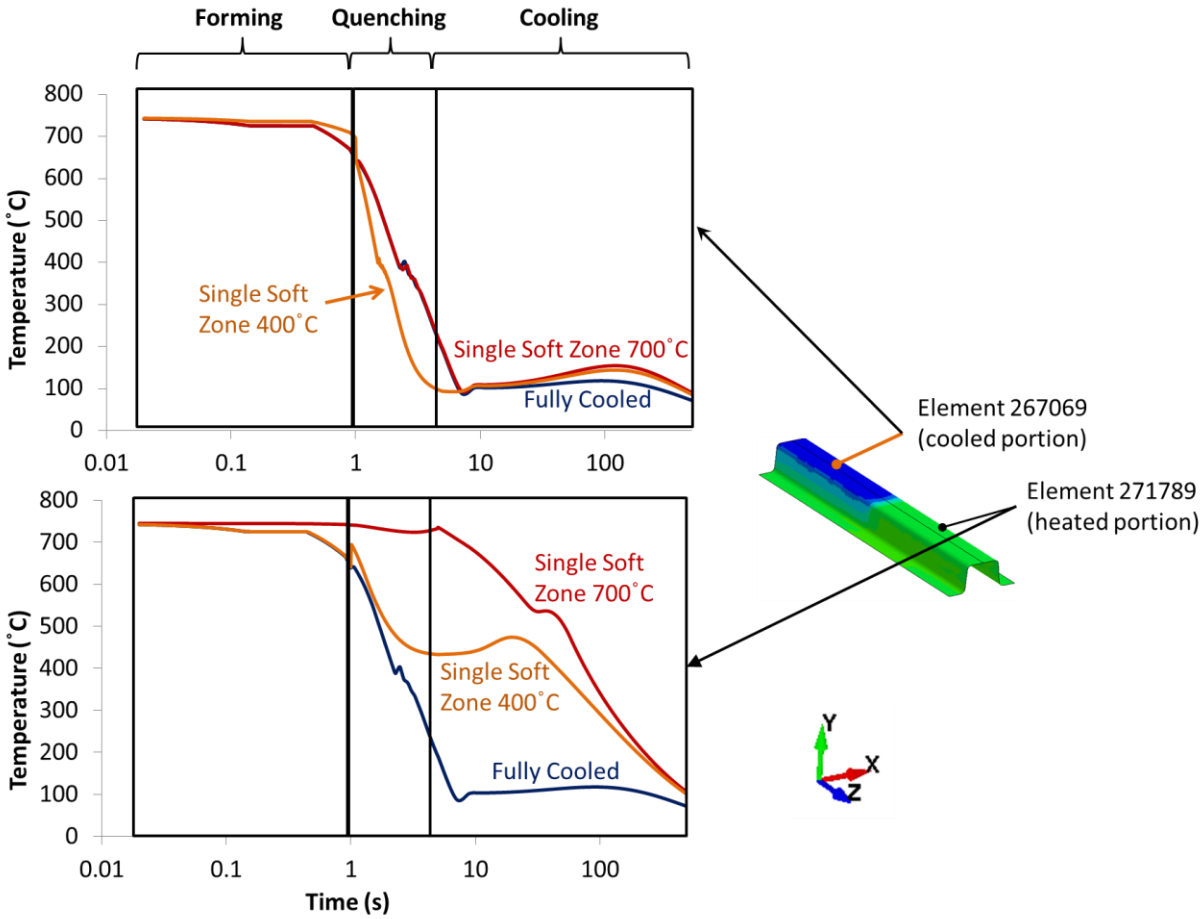

Figure 47. Temperature-time history of selected elements in blank

The considerably different temperature-time histories shown in Figure 47 indicate that the rate of cooling varied considerably between different types of parts. These differing levels of cooling indicate that the predicted levels of Vickers hardness in each type of part will also vary significantly, as they did on the actual as-formed parts. The predicted Vickers hardness results are discussed in section 4.5.

The temperature-time histories also provide an insight into what likely happened to the Usibor® 1500P blank during the actual THS cycle. The THS model predicted that the heated portion of the *fully cooled* part experiences a low rate of cooling during the forming stage, but a very high rate during the quenching stage. This rapid rate of cooling predicted by the model likely also occurred in the actual *fully cooled* part during the THS process, and resulted in a fully or mostly martensitic microstructure and high Vickers hardness.

In the *single soft zone 400˚C* part, the THS model predicted an almost zero cooling rate in the latter half of the quenching stage and into the first few seconds of the cooling stage. Subsequent to the first few seconds, the heated portion of the *single soft zone 400˚C* part actually increased in temperature, before finally decreasing again. The increase in temperature was likely caused by latent heat release resulting from a phase transformation. The fact that the *single soft zone 400˚C* part experienced a slower rate of cooling than the *fully cooled* part helps justify the lower values of Vickers hardness measured in this part.

The heated portion of the *single soft zone 700˚C* part seemed to experience negligible heat loss in the forming or quenching stages. This makes sense because during these stages, the part was held in tooling that was heated to 700°C. The rate of cooling did increase in the cooling stage, bit it was still lower than the rate of cooling predicted for the *fully cooled* and *single soft zone 400˚C* parts. This slow rate of cooling in the initial stages of the THS process explains the low values of Vickers hardness measured in these parts.

The cooled portion of all three types of parts experienced a very quick reduction in temperature, as shown in the first graph in Figure 47. This indicates the formation of martensite in the cooled region, which is consistent with what was observed in the micro-hardness measurements. Therefore, the temperature trends predicted by the THS model agree with the measured Vickers hardness values shown in Figure 45.

4.3 Simulated Results – Plastic Strain in Blank

As explained in section Numerical Modelling of the Crash of THS Components, inducing plastic strain during forming in Usibor® 1500P tends to "shift" the CCT diagram to the left (refer to Figure 2 in section 1.2). In other words, it tends to make the material softer (i.e., a lower Vickers hardness). Therefore, analyzing the predicted plastic strain in the blank is crucial in understanding its final strength distribution.

Figure 48 shows contour plots of effective plastic strain in all four types of blanks. The contour plots were taken from different points in the forming and quenching stages of the THS model (t=0.5s, t=1s and t=5s). As is evident from Figure 48, and expected as well, the flange and top

section contained little to no plastic strain, while the side-wall in all four types of parts contained significant amounts of plastic strain. The side-wall in the heated portion of the part experienced higher levels of effective plastic strain than in the cooled portion of the part.

Figure 49 shows the time history of the effective plastic strain in two elements for the *fully cooled* and the *single soft zone* parts. In all three types of parts, the majority of the plastic strain is induced during the forming stage. However, some strain evolution does occur in the quenching phase as well.

The micro-hardness measurements on the as-formed blanks indicated that there was generally a drop of approximately 15-20HV from the top section to the side-wall in the heated portion of the same part. While this can be partially attributed to a lower rate of cooling in the side-wall, the effect of effective plastic strain must also be considered, since more plastic strain scales down the activation energy for a phase (as shown in Table 5 and Table 6).

An interesting trend that can be observed from Figure 48 and Figure 49 is that the effective plastic strain in the side-walls was proportional to the temperature at which the part was formed. As such, the parts can be ranked by the amount of plastic strain induced in the wall, from lowest to highest, as follows: *fully cooled*, *single soft zone 400˚C, graded soft zone* and *single soft zone 700˚C*. This ranking is the same as the one obtained when ordering the parts from "hardest" to "softest" in section 4.1. Therefore, the effective plastic strains obtained by the model are consistent with the measured values of Vickers hardness in Figure 45.

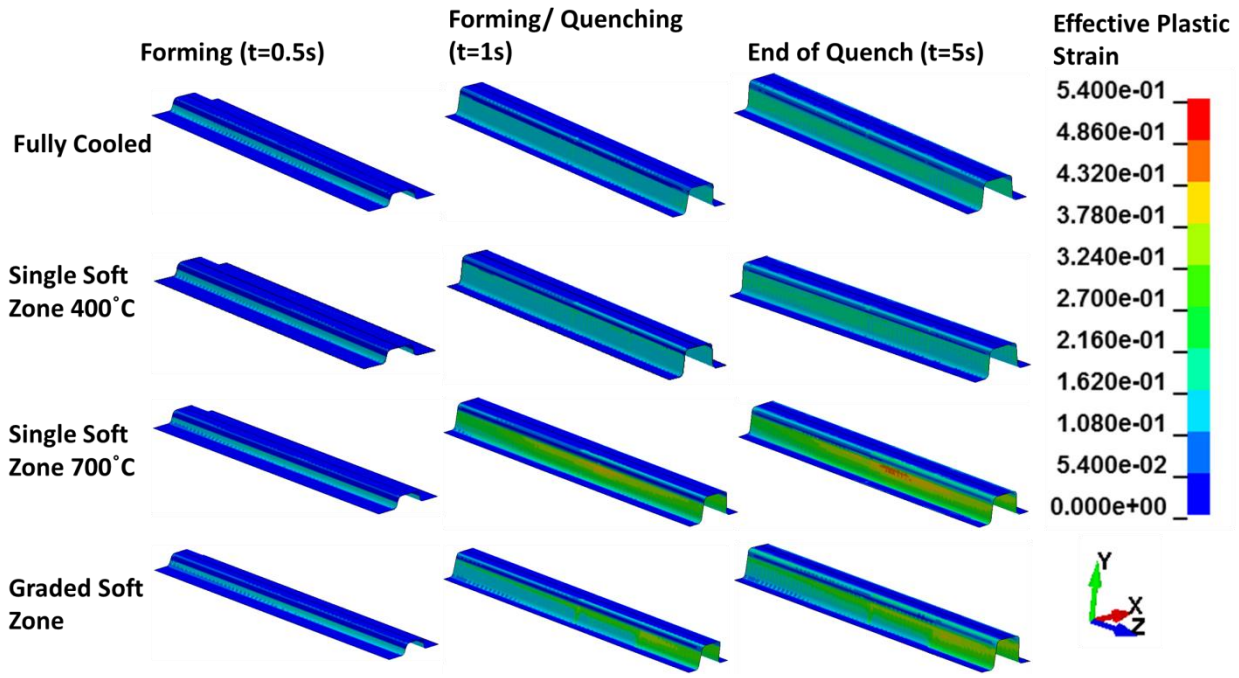

Figure 48. Contour plots of effective plastic strain in the blank during the THS simulation

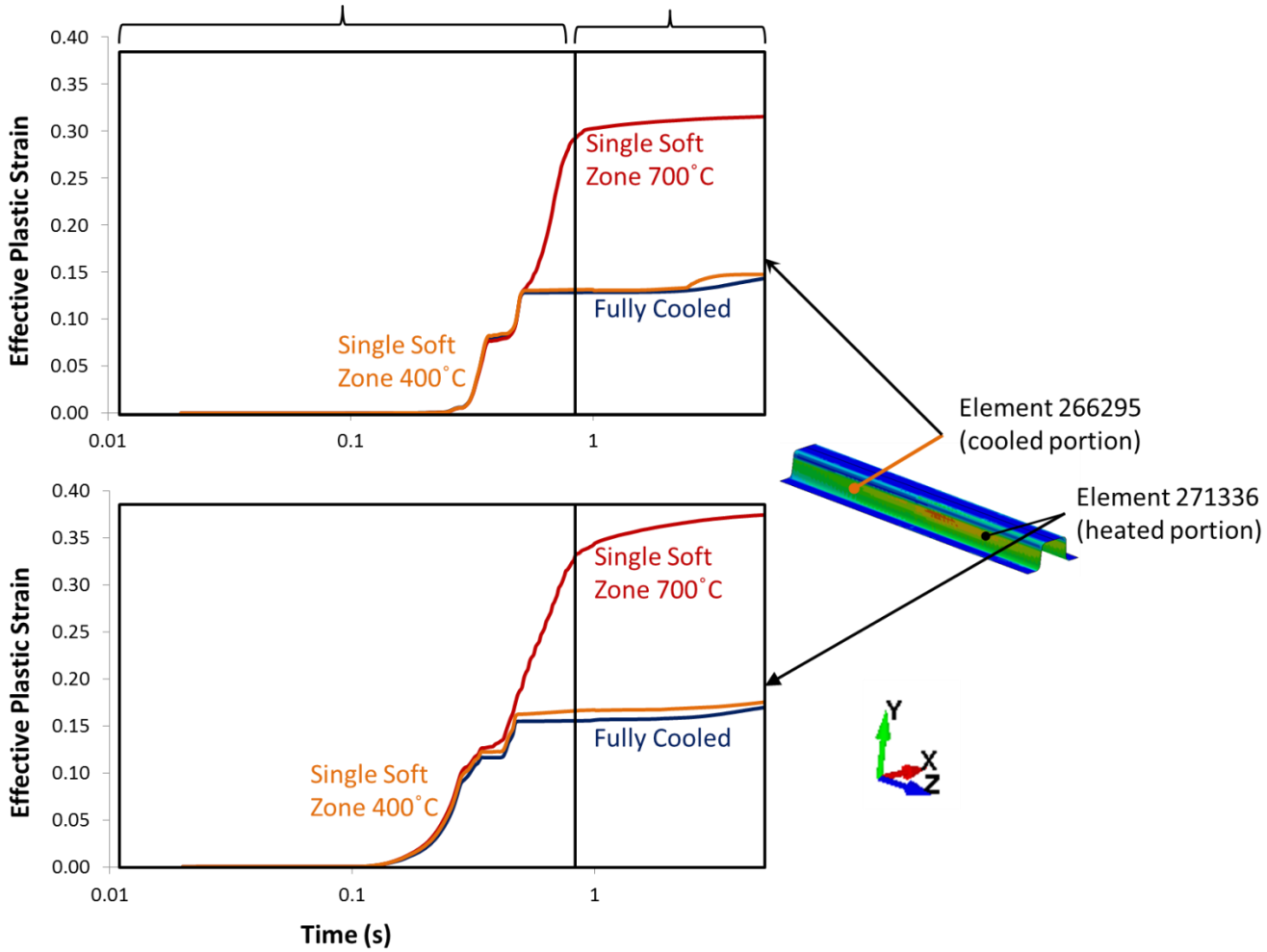

Figure 49. Effective plastic strain vs. time history of selected elements in blank

4.4 Simulated vs. Experimental Results – Sheet Thickness

The predicted values of sheet thickness do not provide any insight into the evolution of the Vickers hardness in a part during THS. Nevertheless, sheet thickness is useful to look at since it is one of only two metrics by which the THS models can be validated in this thesis (the other metric being Vickers hardness).

4.4.1 Simulated Results

Figure 50 shows contour plots displaying the sheet thickness at the end of the THS model for all four types of parts. The general trend in these contour plots was that a higher forming temperature led to higher sheet thickness in the top section and flange. This is evidenced by the fact that the thinnest flange existed in the *fully cooled* part and the thinnest *top section* existed in

the cooled portion of all four types of parts. The thickest top section existed in the heated portion of the *single soft zone 700˚C* part as well as the 700˚C zone of the *graded soft zone* part.

In the side-wall, more thinning was predicted in the heated portion of the part than the cooled portion. This is consistent with the effective plastic strain contours in Figure 48, which showed that the side-wall in the heated portion of any part experienced higher levels of plastic strain than in the cooled portion of the same part. Unlike in the flange and top section, no apparent trend can be observed when comparing the side-walls of different types of parts.

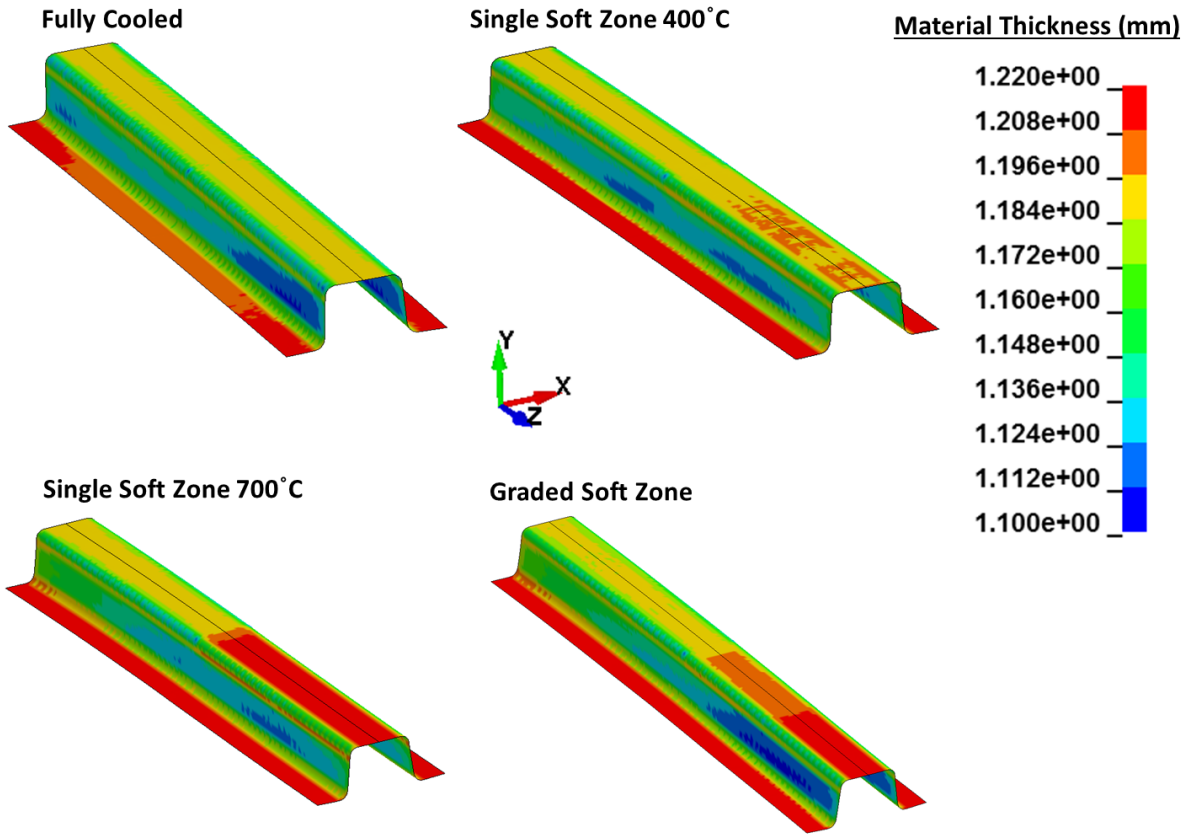

Figure 50. Contour plots showing the predicted material thickness for each of the four types of parts investigated

4.4.2 Simulated Results vs. Experimental Results

Figure 51 plots the predicted profiles of sheet thickness in the axial direction alongside the measured values of material thickness. Plots for the flange, wall and top section of all four types of parts are presented.

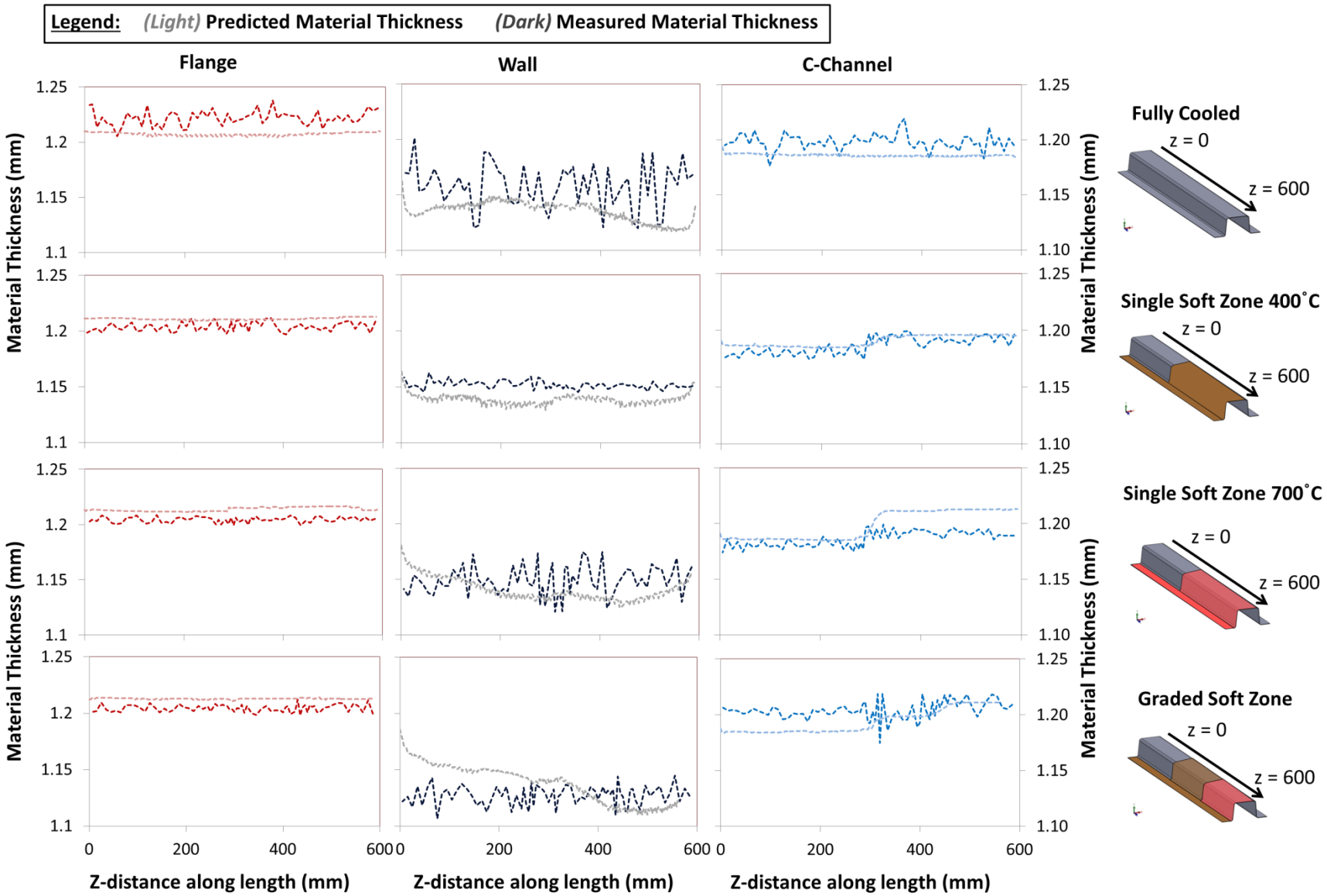

Figure 51. Measured (dark) and predicted (light) profiles of material thickness (dashed) along the axial direction of each part

The predicted thickness and measured thickness agree well with each other in the flanges of all four types of parts. The model slightly over-predicted the thickness in the tailored parts and under-predicted the thickness in the *fully cooled* parts. There was also good agreement in the top sections of the *fully cooled* and *single soft zone 400˚C* parts, the cooled portion of the *single soft zone 700˚C* part and the heated portion of the *graded soft zone* part. The model over-predicted the thickness in the heated portion of the top section of the *single soft zone 700˚C* part and the cooled portion of the top section of the *graded soft zone* part.

The discrepancy between the model and experimental values of thickness is quantified in Table 13, in the form of a percent difference. The percent difference was highest in the side-walls of each type of part. This result is somewhat expected, since the measured values of thickness in the wall contained a lot of noise, which was likely caused by uneven contact with the tooling. The THS models, however, had perfectly even contact between the side-wall and tooling. Therefore, it is not appropriate to compare the measured thickness in the side-wall against the predicted thickness.

Overall, the THS models were able to predict the correct trends in material thickness in the top section and flange. Also, the magnitudes of predicted thickness were generally not too different from the measured thickness in the top section and flange. Therefore, the THS models do have a certain level of correctness in them, based on this text metric.

Table 13. Percent difference between measured and predicted sheet thickness

	Flange		**Side-Wall**		**Top Section**	
	Cooled	Heated	Cooled	Heated	Cooled	Heated
Fully Cooled	1.08%	1.26%	1.79%	2.33%	0.95%	1.07%
Single Soft Zone 400˚C	0.62	0.55	1.30	1.06	0.50	0.36
Single Soft Zone 700˚C	0.64	0.94	1.75	1.15	0.42	1.75
Graded Soft Zone	0.67	0.73	2.19	0.34	1.51	0.08

4.5 Experimental vs. Numerical Comparison – Micro-Hardness

The micro-hardness measurements conducted on the as-formed parts serve as the second metric by which to validate the THS models in this thesis. They also serve as the primary way to validate the Åkerström material model that was used to model the blank.

4.5.1 Simulated Results

Contour plots showing the predicted micro-hardness for all four categories of parts can be seen in Figure 52. Based on these contour plots, the simulated models can be ranked, from hardest to softest, in the following order: *fully cooled*, *single soft zone 400°C*, *graded soft zone* and *single soft zone 700°C*. In all three tailored cases, the model was able to predict two or three distinct zones of hardness in the top section along the axis of the part.

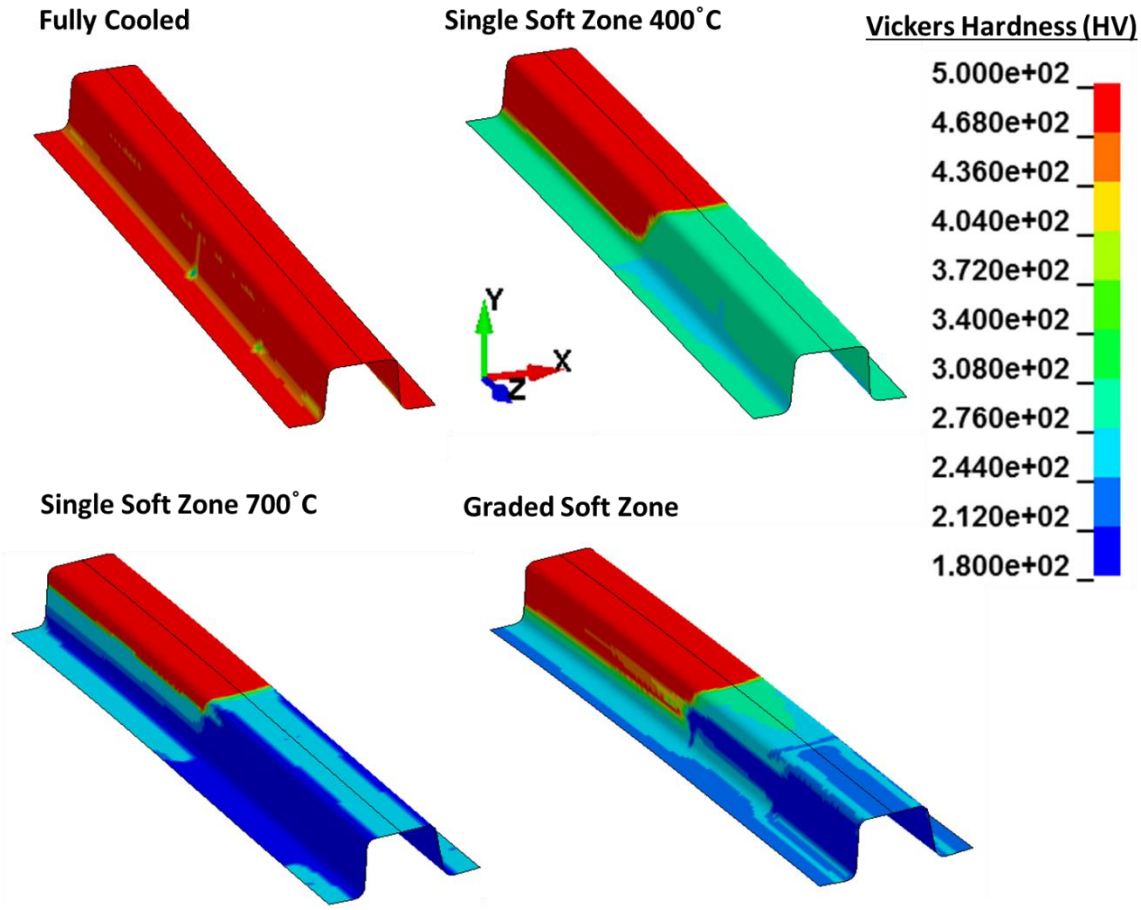

Figure 52. Contour plots showing the predicted Vickers hardness for each of the four types of parts investigated

The micro-hardness predicted in the *fully cooled* part corresponds to the martensitic range (465-486 HV) in all regions of the part except near in the transition zone in the fillets of the part. In these areas, the THS models predicted a micro-hardness corresponding to a mixed bainitic/martensitic microstructure (~370 HV).

In the *single soft zone* parts, the THS model predicted a hard, martensitic zone in half the length of the top section and a soft zone in the remaining half. The micro-hardness was predicted to be 278 HV in the soft zone of the top section of the *single soft zone 400°C* part. The same region in the *single soft zone 700°C* contained a micro-hardness of 246 HV. This same trend was replicated in the walls of both *single soft zone* parts, as seen in Figure 52. The micro-hardness along the flange of the *single soft zone* parts did not vary significantly.

The top section of the *graded soft zone* parts contained three distinct zones of hardness, while the side-wall contained only two. The flange was fairly uniform throughout its entire length, with the micro-hardness ranging from 240-250 HV.

4.5.2 Simulated Results vs. Experimental Results

Figure 53 plots the measured and predicted Vickers hardness, in a format similar to Figure 51. The "hardest to softest" trend observed in the simulated models is the same as that seen in the measured hardness values.

In terms of accuracy of the THS models, the numerical THS model was able to predict the Vickers hardness in the flange region with reasonable accuracy for all part configurations except in the *fully cooled* part where the Vickers hardness was over-predicted, and in the transition zone of the *single soft zone 400˚C* part, where the spike in hardness was not captured by the model. The percent difference between the measured and predicted values of micro-hardness in all parts is given in Table 14.

The micro-hardness predictions in the side-wall were very accurate in the *fully cooled* part and the heated portions of the three tailored parts. The micro-hardness was over-predicted in the cooled portion of the wall in the *single soft zone 400°C* and was under-predicted in the cooled portion of the wall in the *single soft zone 700°C* part.

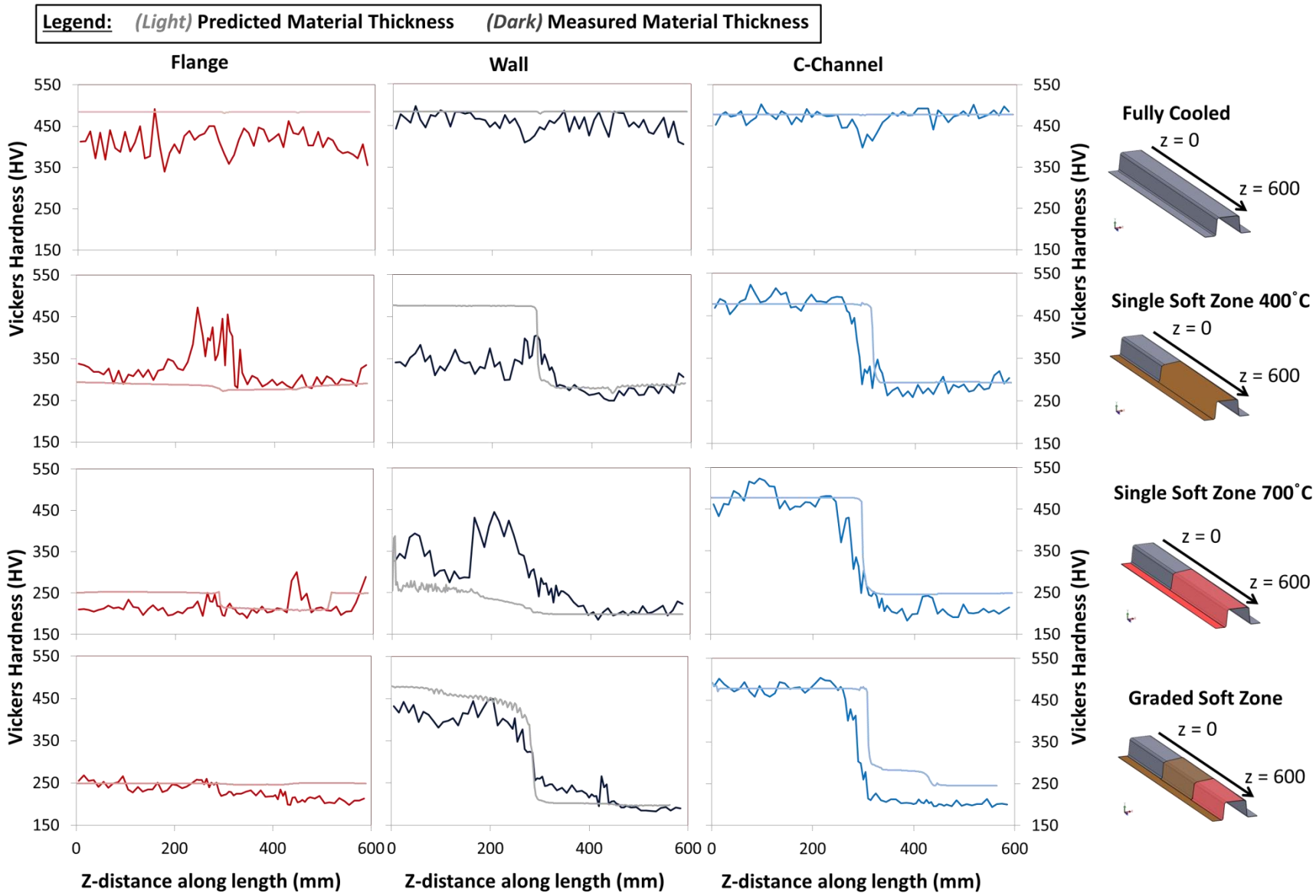

Figure 53. Measured (dark) and predicted (light) profiles of Vickers hardness along the axial direction of each part

Table 14. Percent difference between measured and predicted micro-hardness

	Flange		**Side-Wall**		**Top Section**	
	Cooled	Heated	Cooled	Heated	Cooled	Heated
Fully Cooled	15.9%	16.5%	4.7%	6.7%	1.4%	1.4%
Single Soft Zone 400˚C	16.7	12.5	31.2	2.9	0.4	4.3
Single Soft Zone 700˚C	15.6	1.7	32.7	12.0	5.3	13.1
Graded Soft Zone	1.2	13.9	12.8	8.1	2.4	25.4

The predicted and measured micro-hardness matched well for the top sections in the *fully cooled* and *single soft zone 400˚C* parts. The micro-hardness also matched well in the cooled portion of the top sections in the *single soft zone 700˚C* and *graded soft zone* parts. The micro-hardness in the heated portion of the top section in the *single soft zone 700˚C* and *graded soft* zone parts was over-predicted.

The predicted micro-hardness in the top section of the *graded soft zone* part contained three hardness zones. This as in contrast to the actual *graded soft zone* part which only contained two zones in its top section. The numerical model was able to achieve these two zones because the shimming issue discussed in section Description of Forming Tooling did not occur in the models. The predicted result indicates that it is possible to obtain three hardness zones along the top section of a part.

With the exception of the few noted examples, the THS models as well as the Åkerström model were able to predict the final micro-hardness in the as-formed parts within a reasonable degree of accuracy. This means that the THS models in this work were set up in a way that accurately reflected the actual THS process. The next chapter in this thesis will discuss the results obtained from the crash models used the resulting micro-hardness from the THS model as input.

5. Crash Experiments & Results

5.1 Dynamic Crush Experiments

5.1.1 Overall Trends in Force-Displacement and Energy Absorption

Figure 54 shows the average force-displacement curves and Figure 55 shows the average energy absorption obtained from the dynamic sled test experiments for each of the four crush rail configurations. The energy absorption curves were calculated assuming an initial energy absorption of zero and by integrating under the force-displacement curves using the trapezoid rule:

$$E^{(i)} = E^{(i-1)} + 0.5(F^{(i)} + F^{(i-1)})(d^{(i)} - d^{(i-1)}) \tag{9}$$

where E represents energy absorbed, F represents force, d represents sled displacement and the superscripts (i) and $(i+1)$ denote the current and previous time step respectively.

The vertical black line in the figures depicts the point at which the sled made contact with the honeycomb stacks, for reference. Three specimens were impact tested for each configuration. Based on Figure 55, the four configurations can be ranked in terms of energy absorption, from highest to lowest, as follows: *fully cooled*, *graded soft zone*, *single soft zone 700˚C* and *single soft zone 400˚C.*

The *fully cooled* specimens absorbed the highest amount of energy (25.8 kJ). Correspondingly, the crash sled displaced the least amount during these tests (292 mm). The *fully cooled* (martensitic) parts also experienced a significantly higher peak load (479 kN) than the other three crush rail configurations. The crush efficiency of the *fully cooled* specimens, defined as the average force divided by the maximum peak load, was 18.4%.

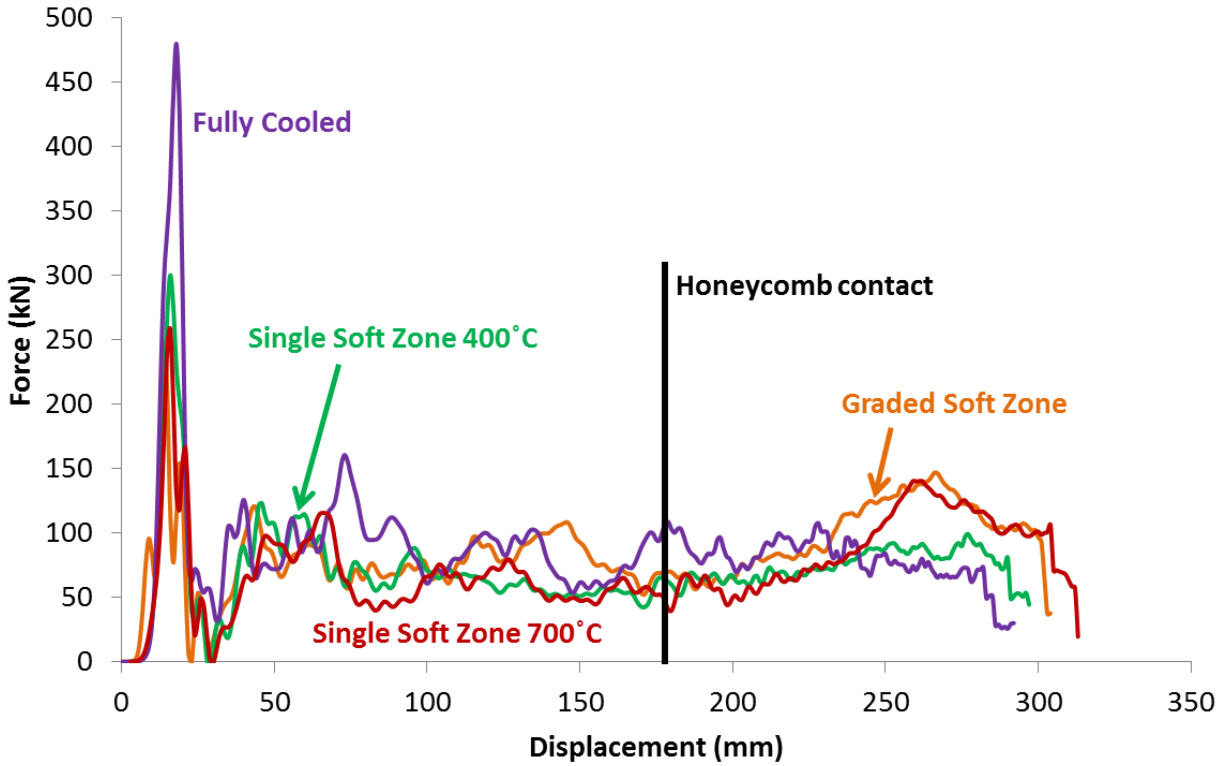

Figure 54. Dynamic force-displacement curves for each of the four types of parts

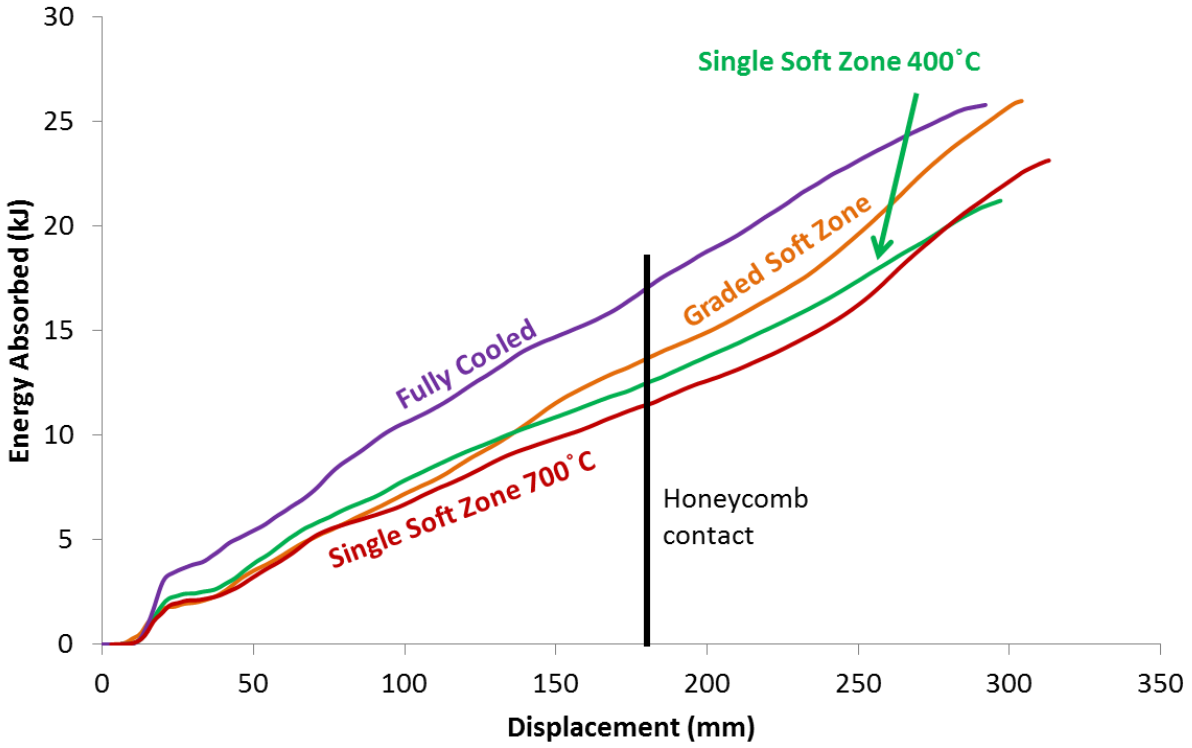

Figure 55. Dynamic energy absorption curves for each of the four types of parts

It should be noted that the fold initiator in the *fully cooled* specimens did not penetrate as deeply as it did in the remaining three crush rail configurations (as explained in section 2.5). The implication of this was that the *fully cooled* specimens were not subjected to as much strain hardening as the other three types of rails during dimple insertion. Therefore, while the observed crush efficiency of the *fully cooled* specimens was observed to be 18.4%, an equivalent dimple depth (which was not possible) in these specimens, when compared to the three tailored rail configurations, would have resulted in a lower peak load, which in turn would have led to a slightly higher crush efficiency.

The *fully cooled* specimens were followed by the *graded soft zone* specimens in terms of energy absorption at the same displacement point of 292 mm. The *graded soft zone* specimens absorbed 24.9 kJ at a displacement of 292 mm. At full displacement, however, they absorbed 26.0 kJ, which was higher than even the *fully cooled* specimens. The *graded soft zone* specimens displayed the best crush efficiency (34.4%) of the four crush rail configurations.

The fact that the *graded soft zone* specimens were able to absorb more energy than the *single soft zone* specimens was unexpected, since the hardness profile in the top section of *single soft zone* parts very closely resembled the top section of the *single soft zone 700˚C* part. This topic will be discussed in section 5.1.5.

The *single soft zone 700˚C* specimens exhibited the second lowest energy absorption (21.9 kJ at a displacement of 292 mm), followed by the *single soft zone 400˚C* specimens (20.9 kJ at a displacement of 292 mm). It should be noted that the *single soft zone 400˚C* specimens exhibited better energy absorption for most of the dynamic crush, except towards the end where they were surpassed by the *single soft zone 700˚C* specimens. The crush efficiency of the *single soft zone 400˚C* specimens was 28.8%, while the efficiency of the *single soft zone 700˚C* parts was 24.0%.

5.1.2 Dynamic Crush Response of the *Fully Cooled* Specimens

Figure 56 shows images taken during the dynamic impact experiment of a *fully cooled* specimen. The images show the pattern of deformation experienced by the specimen from beginning to end. The final deformed shapes of the three crushed *fully cooled* specimens are shown in Figure 57.

It is apparent from both Figure 56 and Figure 57 that all three *fully cooled* specimens experienced folding at the beginning of the dynamic impact. This would account for the high, average peak load observed for this high strength martensitic crush rail configuration. Subsequent to one or two folds, however, the specimens experienced extensive tearing and fracture. The failure pattern varied between each individual specimen. One crush specimen, pictured in the centre in Figure 57, split into two pieces during the crush. All three *fully cooled* specimens experienced spotweld failure.

The variation in failure in the *fully cooled* configuration caused a large amount of scatter in the force-displacement and energy absorption response for each of the three specimens tested. The force-displacement and energy absorption data is shown in Figure 58. The gray lines in the background indicate data from an individual crash test and the red lines indicate the average response.

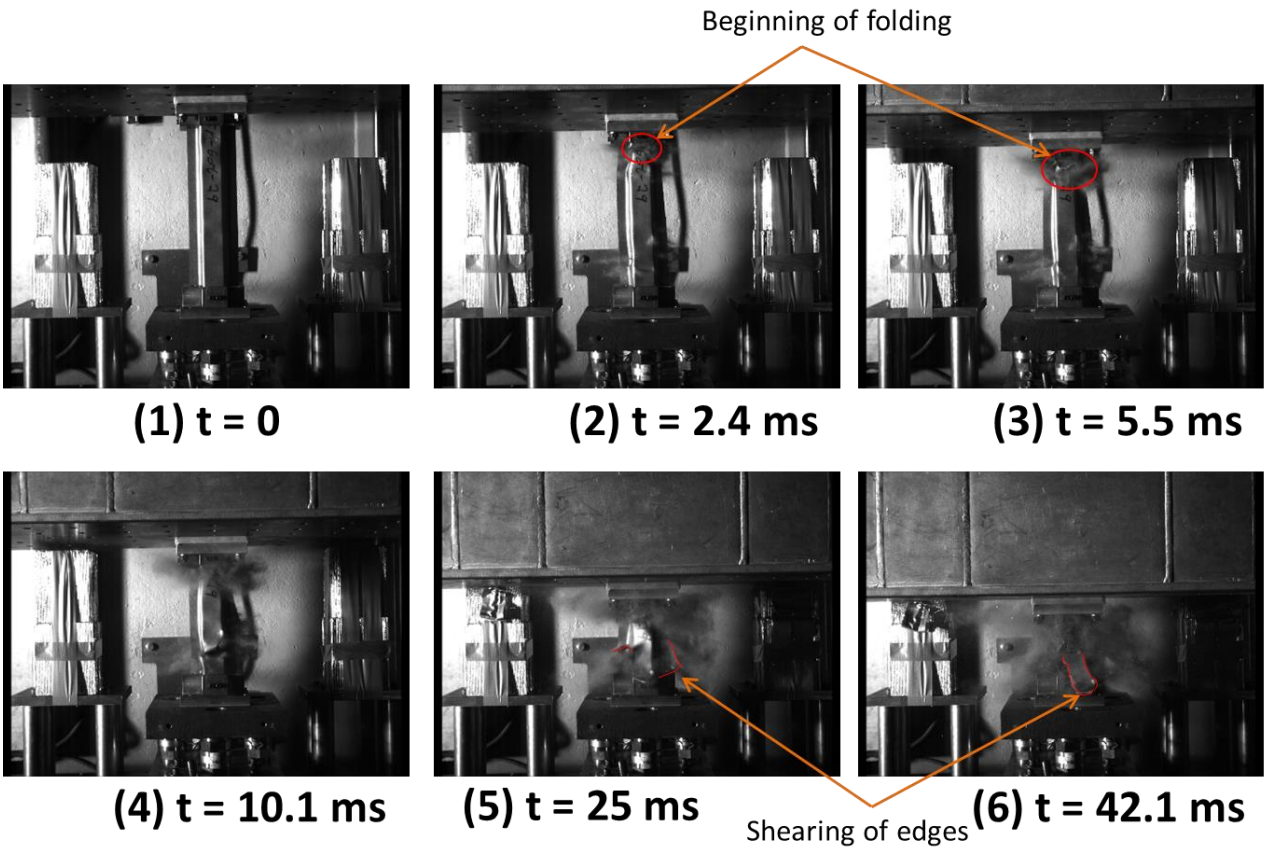

Figure 56. Deformation of a *fully cooled* specimen during a dynamic test.

Figure 58 shows that the loads experienced by each part are repeatable for approximately the first 50 mm of the crush, before they diverge. This consistent portion of the load-displacement curves corresponds to the formation of the first fold in the *fully cooled* specimens. The divergence that follows likely results from the onset of irregular cracking and shearing.

Figure 57. Final deformed shapes of the three crushed *fully cooled* specimens

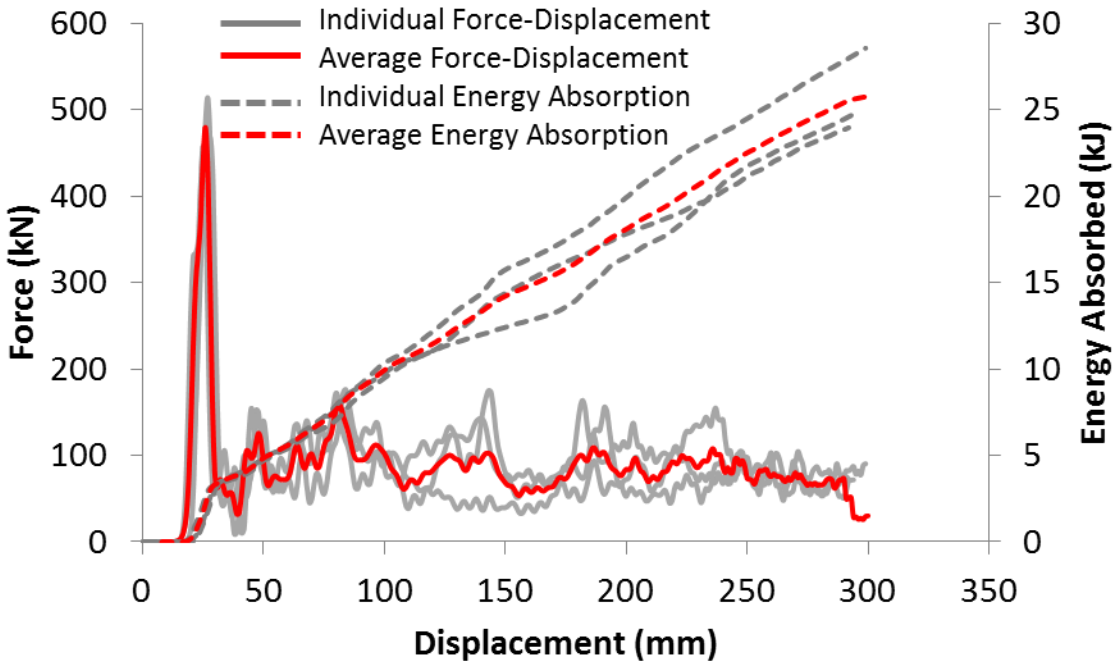

Figure 58. Force-displacement and energy absorption data for the *fully cooled* specimens

Overall, the *fully cooled* specimens had excellent energy absorption, but exhibited a large scatter in their crash response. Furthermore, the extent of failure observed in these specimens and their low crush efficiency is not desirable in an actual automotive part.

5.1.3 Dynamic Crush Response of the *Single Soft Zone 400˚C* Specimens

Still images showing the dynamic crush of a *single soft zone 400˚C* specimen can be seen in Figure 59. The final deformed shapes of all three crushed *single soft zone 400˚C* specimens are shown in Figure 60.

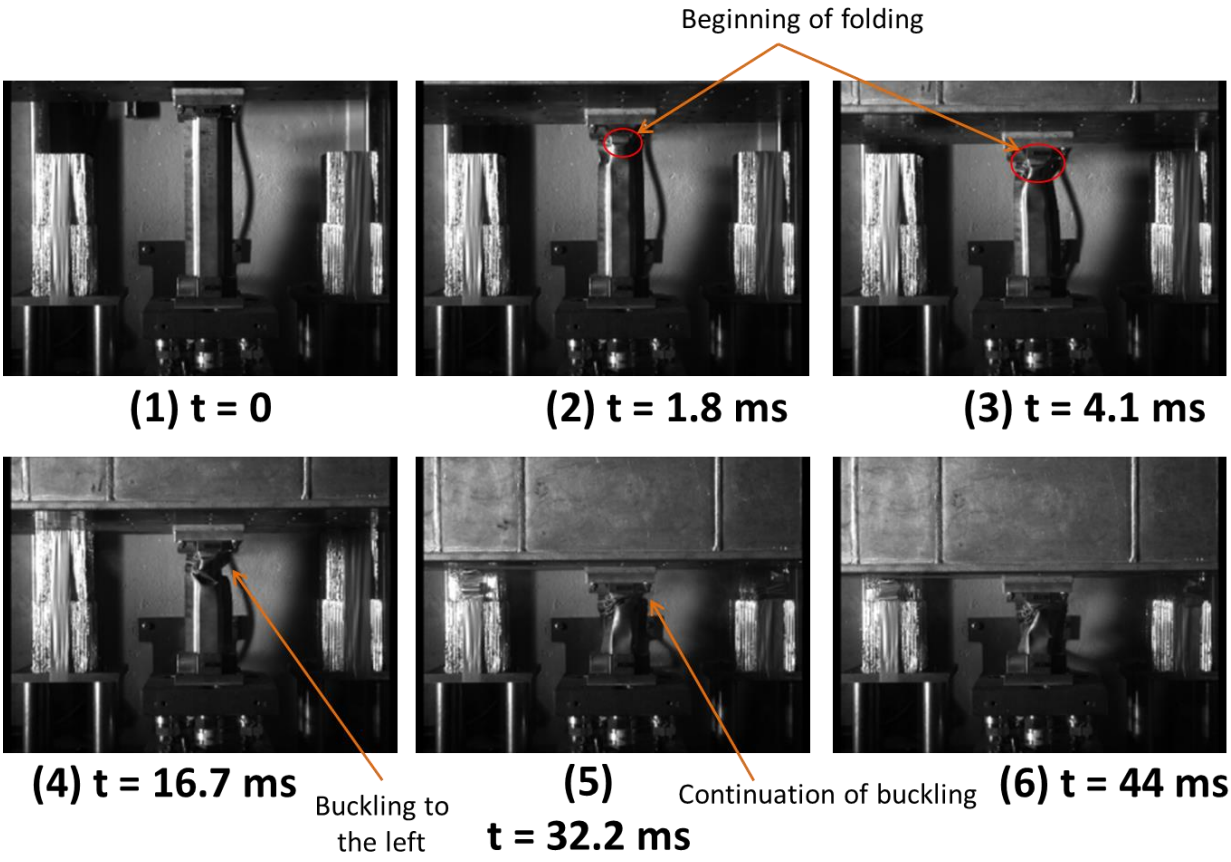

Figure 59. Deformation of a *single soft zone 400˚C* specimen during a dynamic test

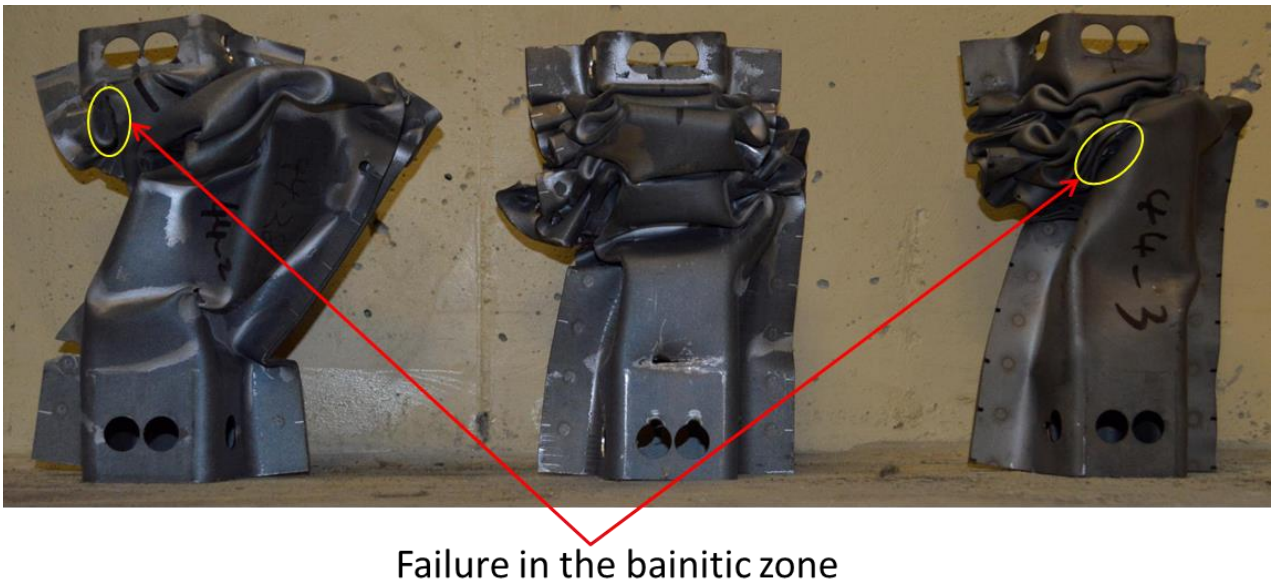

Figure 60. Final deformed shapes of the three crushed *single soft zone 400˚C* specimens

As made apparent by Figure 59 and Figure 60, the *single soft zone 400˚C* specimens experienced the formation of several folds during impact. Some crack propagation did occur in the soft zone of these specimens, as indicated in Figure 60. The failure experienced by the *single soft zone 400˚C* specimens, though not as extensive as the *fully cooled* parts, was still significant.

Bardelcik et al. [68] observed that tensile specimens of 270 HV hardness, which contained no ferrite, exhibited relatively low failure strains. The *single soft zone 400˚C* parts in this work exhibited a micro-hardness of 280 HV, and therefore, the more extensive failure experienced by these parts (relative to the *single soft zone 700˚C* and *graded soft zone* specimens, see below) is consistent with the results found in [68].

The *single soft zone 400˚C* specimens were also subject to buckling after the formation of three or four folds (as shown in Figure 59). The buckling most likely had a negative effect on the energy absorption characteristics in these specimens. The force-displacement and energy absorption data for the *single soft zone 400˚C* specimens is presented in Figure 61.

All three curves are very consistent for approximately the first 75 mm of crush, after which they diverge. The force and energy curves for one specimen diverge well below the curves for the other two specimens. The low energy absorption curve is the one that belonged to the specimen

pictured on the very left in Figure 60. The remaining two energy absorption curves remained fairly consistent until a displacement of approximately 225 mm after which they also diverged.

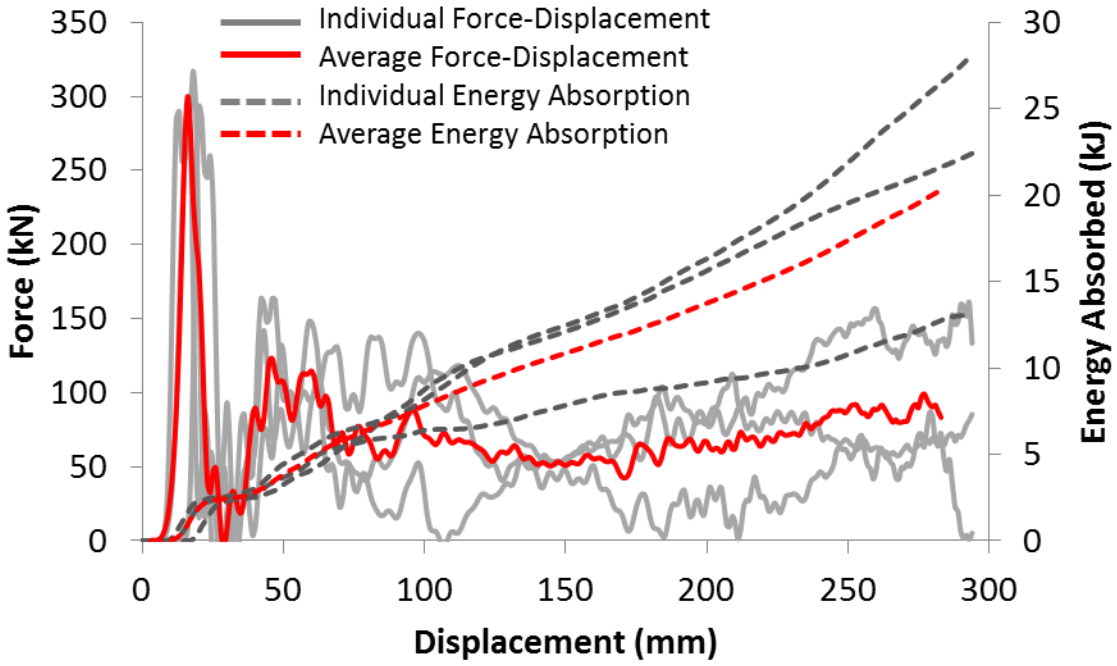

Figure 61. Force-displacement and energy absorption data for the *single soft zone 400˚C* specimens

Overall, the energy absorption of the *single soft zone 400˚C* specimens was hampered by their tendency to buckle during impact. These specimens did not experience nearly the same level of crack propagation as the *fully cooled* specimens. The small amounts of cracking, however, likely caused misalignment in the specimens that led to their buckling.

5.1.4 Dynamic Crush Response of the *Single Soft Zone 700˚C* Specimens

Still images showing the dynamic crush of a *single soft zone 700˚C* specimen can be seen in Figure 62. The final deformed shapes of all three crushed *single soft zone 700˚C* specimens are shown in Figure 63.

Two of the three *single soft zone 700˚C* specimens buckled, while one did not. In the *single soft zone 400˚C* crush rail configuration, the buckling was likely caused by the onset of cracking. However, a different deformation mode existed in the *single soft zone 700˚C* configuration.

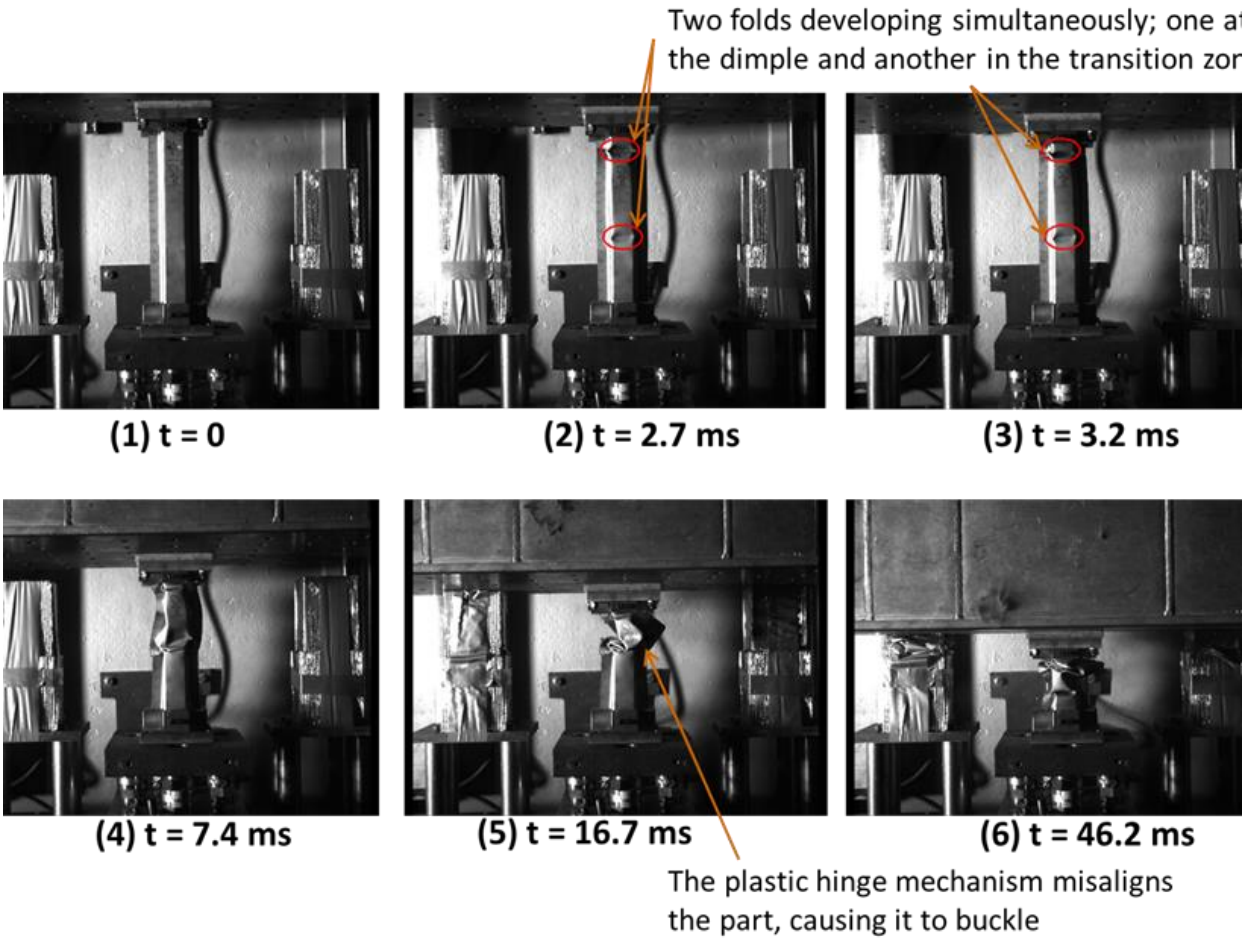

Figure 62. Deformation of a *single soft zone 700˚C* specimen during a dynamic test

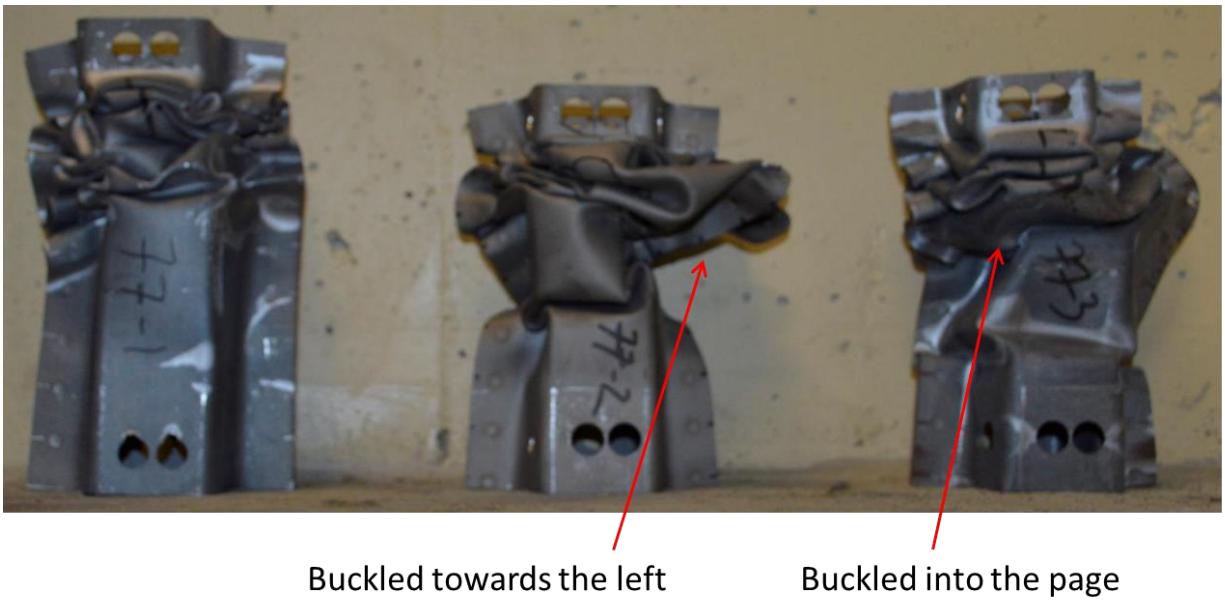

Figure 63. Final deformed shapes of the three crushed *single soft zone 700˚C* specimens

The discontinuity associated with the steep gradient in micro-hardness in the transition zone in these parts (as discussed in section 4.1.1) lead to the development of two folds in the specimen during impact: one at the location of the fold initiator and one at the transition zone (Figure 62, image 2). This response resulted in global buckling through formation of a "plastic hinge mechanism", as shown in Figure 62 (image 5).

The buckling occurred in two of the three specimens that were crushed. The third specimen (on the very left in Figure 63) folded axially. No visible signs of cracking were present in any of the *single soft zone 700˚C* specimens.

The force-displacement and energy absorption curves for the *single soft zone 700˚C* specimens are shown in Figure 64. During the first 150 mm of the crush, the three energy absorption curves displayed excellent repeatability, but diverged at the onset of buckling. The one specimen that did not buckle exhibited the highest energy absorption characteristics, as expected. Despite this variation in buckling behaviour, the *single soft zone 700˚C* specimens had much lower scatter than the *fully cooled* and *single soft zone 400˚C* specimens.

The consistency of the curves during the first half of impact offers promise that tailoring the properties of an axial crush member has a positive effect in its crash response. The *single soft zone 700˚C* specimens also did not appear to experience failure or crack initiation. The tendency of these parts to buckle, however, is not desirable since the buckling mode of deformation reduces energy absorption (as opposed to the folding mode).

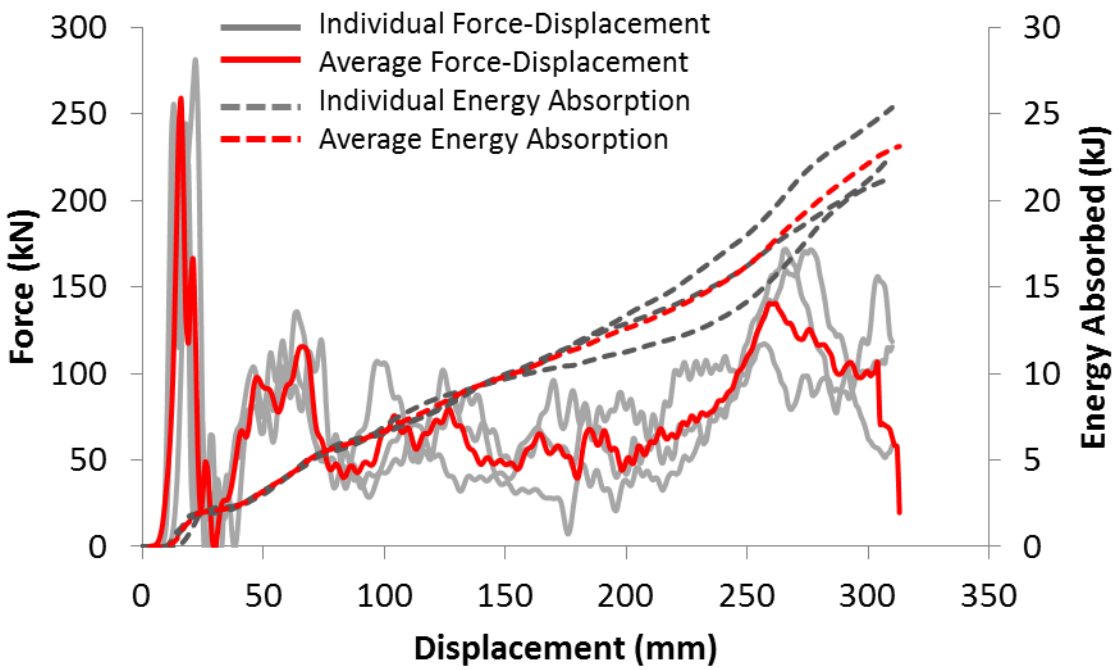

Figure 64. Force-displacement and energy absorption data for the *single soft zone 700˚C* specimens

5.1.5 Dynamic Crush Response of the *Graded Soft Zone* Specimens

Still images showing the dynamic crush of a *graded soft zone* specimen can be seen in Figure 65. The final deformed shapes of all three crushed *graded soft zone* specimens are shown in Figure 66.

None of the *graded soft zone* specimens experienced any buckling or visible signs of cracking. All three specimens folded in the axial direction. The energy absorption curves (shown in Figure 67) for these specimens were also very repeatable for the entire duration of the dynamic crush experiment. As is evident from the curves, the *graded soft zone* crush rail configuration exhibited the least amount of variation between its three tests, as compared to the other three configurations.

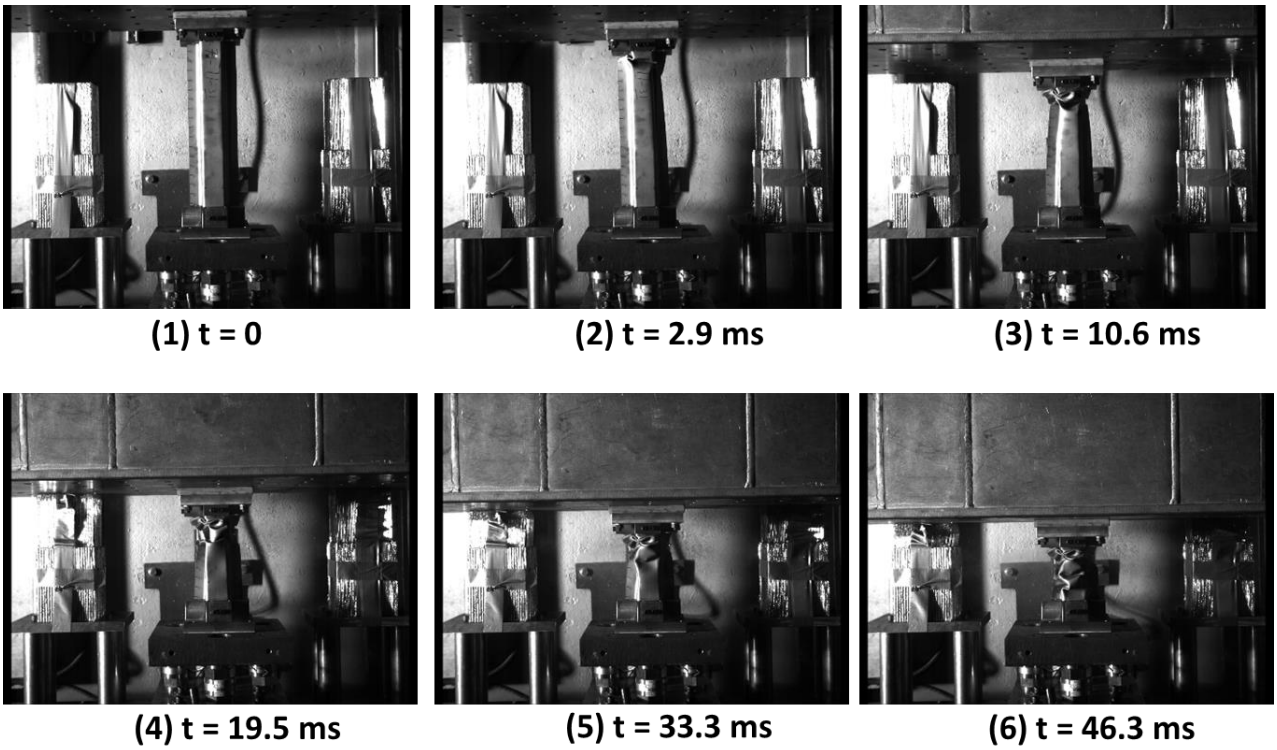

Figure 65. Deformation of a *graded soft zone* specimen during a dynamic test

Figure 66. Final deformed shapes of the three crushed *graded soft zone* specimens

It is interesting that the *graded soft zone* specimens would behave so differently from the *single soft zone 700°C* specimens, considering that the micro-hardness measurements conducted on them (which were presented in section 4.1.1) indicated that the top section in the *graded soft zone* part contained a very similar profile as the top section in the *single soft zone 700˚C* part.

Thus, it would be expected that the *graded soft zone* specimens behave in a manner very similar to the *single soft zone 700˚C* specimens. This was not the case, since none of the *graded soft zone* specimens experienced a plastic hinge mode of deformation.

The most plausible explanation for the discrepancy between the two types of configurations would be the fact that the side-wall in the *graded soft zone* part did contain three zones of hardness instead of two. Even though the gradient between the three hardness zones was not very steep, it appears to have inhibited the formation of a second, simultaneous fold at the transition zone between the cooled and heated portions of the *graded soft zone* specimens.

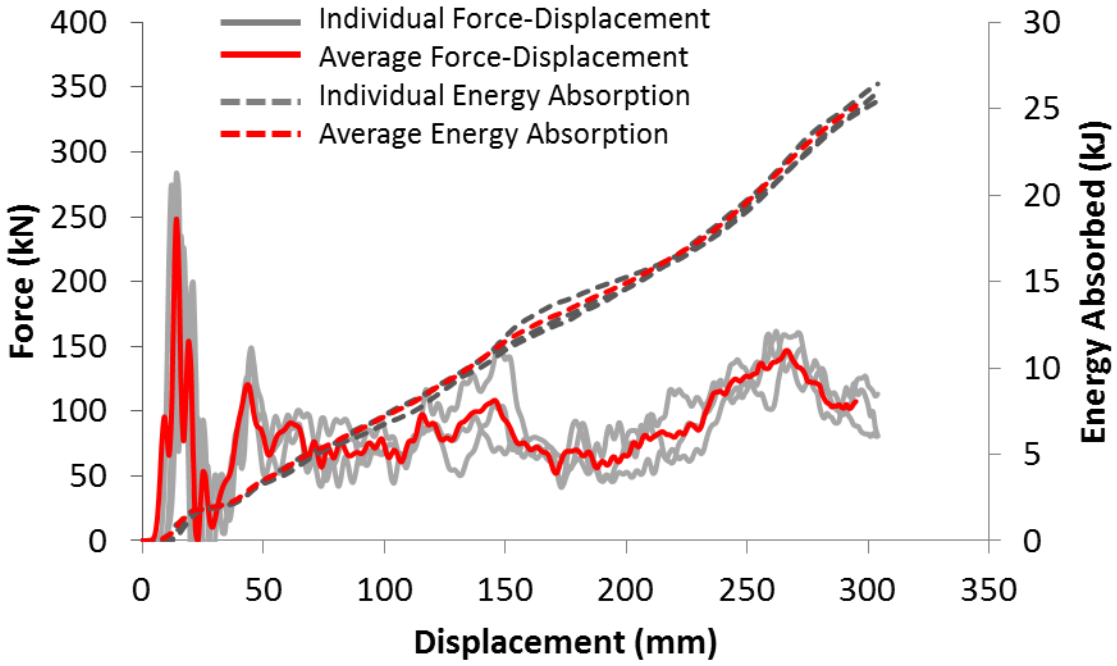

Figure 67. Force-displacement and energy absorption data for the *graded soft zone* specimens

Overall, the *graded soft zone* specimens exhibited the best dynamic crash response among the four types of configurations tested. The *graded soft zone* specimen matched the *fully cooled* specimens in terms of average energy absorption. They were not susceptible to buckling or crack formation, and they exhibited the least scatter in energy absorption, as can be seen in Figure 67.

5.2 Quasi-Static Experiments

5.2.1 Overall Trends in Force-Displacement and Energy Absorption

Just as with the dynamic sled experiments, three specimens were quasi-statically crushed from the *fully cooled*, *single soft zone 700˚C* and *graded soft zone* configurations. Due to a shortage of parts, only two specimens from the *single soft zone 400˚C* configuration were crushed. The average force-displacement curves for the four configurations are shown in Figure 68 and the average energy absorption curves are shown in Figure 69. The energy absorption curves were obtained using eq. (**9**).

Just as in the dynamic crash experiments, the highest energy absorption in the quasi-static experiments was observed by the *fully cooled* specimens (12.5 kJ), followed by the *graded soft zone* specimens (12.4 kJ). The *graded soft zone* specimens were followed by the *single soft zone 400˚C* specimens in energy absorption (11.6 kJ). Unlike in the dynamic experiments, the energy absorption in the *single soft zone 400˚C* specimens consistently remained above the *single soft zone 700˚C* specimens, which absorbed 8.3 kJ.

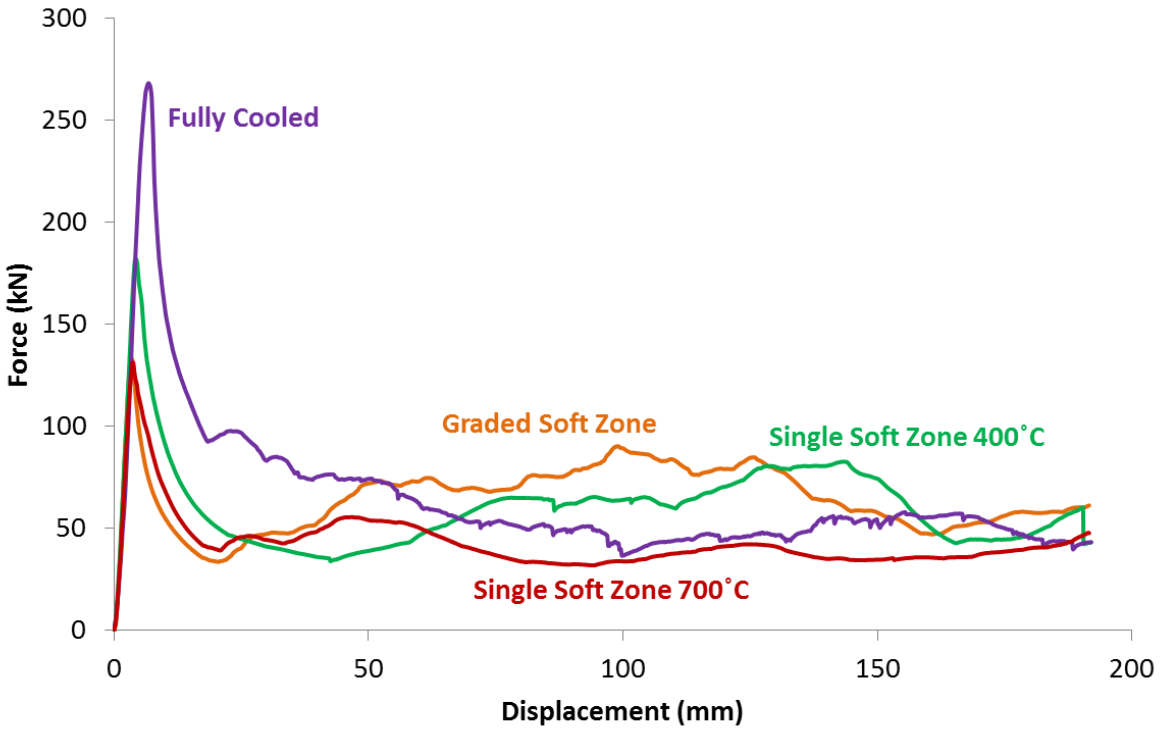

Figure 68. Quasi-Static force-displacement curves for each of the four types of parts

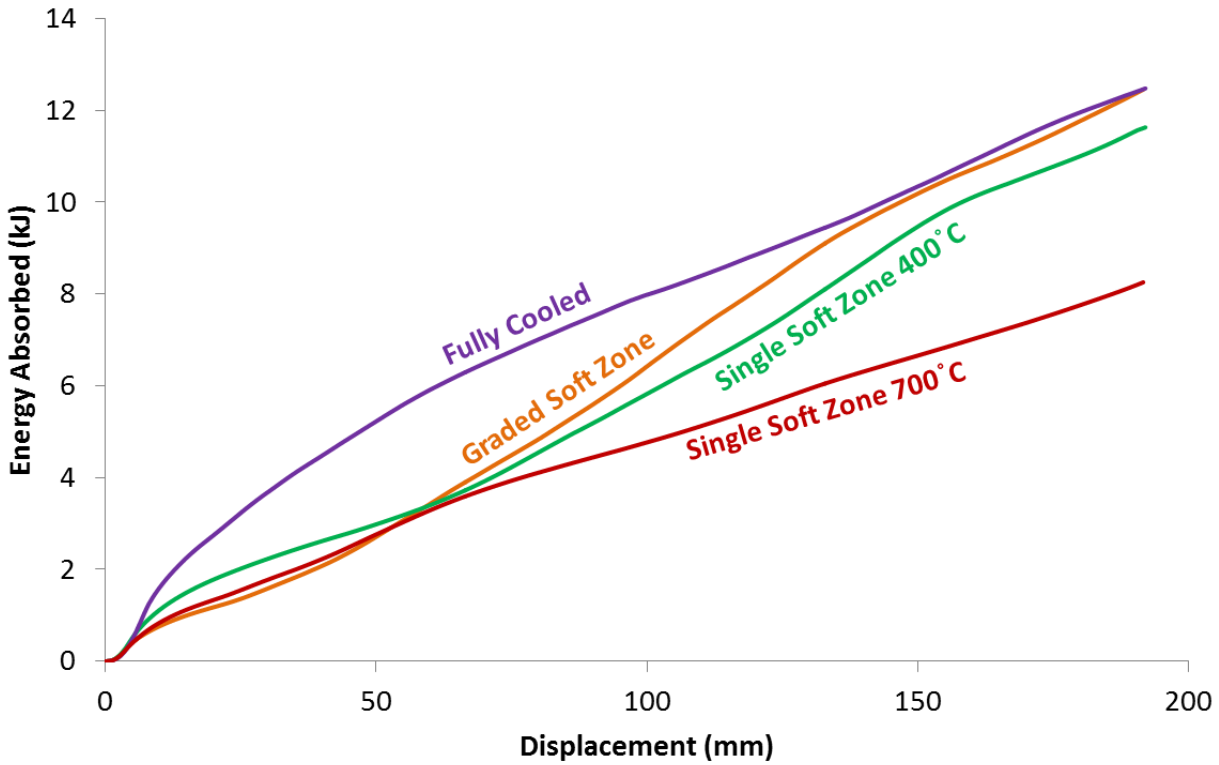

Figure 69. Quasi-Static energy absorption curves for each of the four types of parts

The crush efficiency of the *fully cooled* specimens was 24.2%, which was the lowest among the four configurations tested. Just as with the dynamic crush experiments, the peak load in the *fully cooled* specimens was slightly misrepresented due to the lower penetration of the fold initiator in these specimens. The *graded soft zone* specimens exhibited the highest crush efficiency of 48.8%. The crush efficiency of the two *single soft zone* configurations was almost identical: 33.2% for the *single soft zone 400˚C* specimens and 32.8% for the *single soft zone 700˚C* specimens.

A point of interest from Figure 69 is that the *graded soft zone* specimens exhibited very poor energy absorption at the start of the quasi-static experiment, when the specimen was crushing in its softest zone (i.e., the zone formed at 700˚C). It is not until a displacement of 75 mm that the energy absorption improves in these specimens.

Details on the *graded soft zone* specimens as well as the other three configuration will be discussed in section 5.2.2 to 5.2.5.

5.2.2 Quasi-Static Crush Response of the *Fully Cooled* Specimens

The *fully cooled* quasi-static experiments were not filmed due to the potential of the Nikon D3200 camera being damaged. As such, there are no still images showing the progression of deformation in these specimens during crush. The final deformed shapes of the three crushed *fully cooled* specimens are shown in Figure 70.

All three *fully cooled* specimens experienced a buckling mode of deformation, and all three also experienced cracking (labelled in Figure 70) and spotweld failure. Also, the deformation did not begin at the location of the fold initiator. Instead, the initial deformation locations were very random in these specimens. Consequentially, there was a very wide scatter in the force-displacement and energy absorption curves (as seen in Figure 71) in these specimens. One specimen, shown in the centre in Figure 70, exhibited exceptionally high energy absorption. The remaining specimens exhibited lower energy absorption

Figure 70. Final deformed shapes of the three crushed *fully cooled* specimens. Locations of cracking are outlined in red

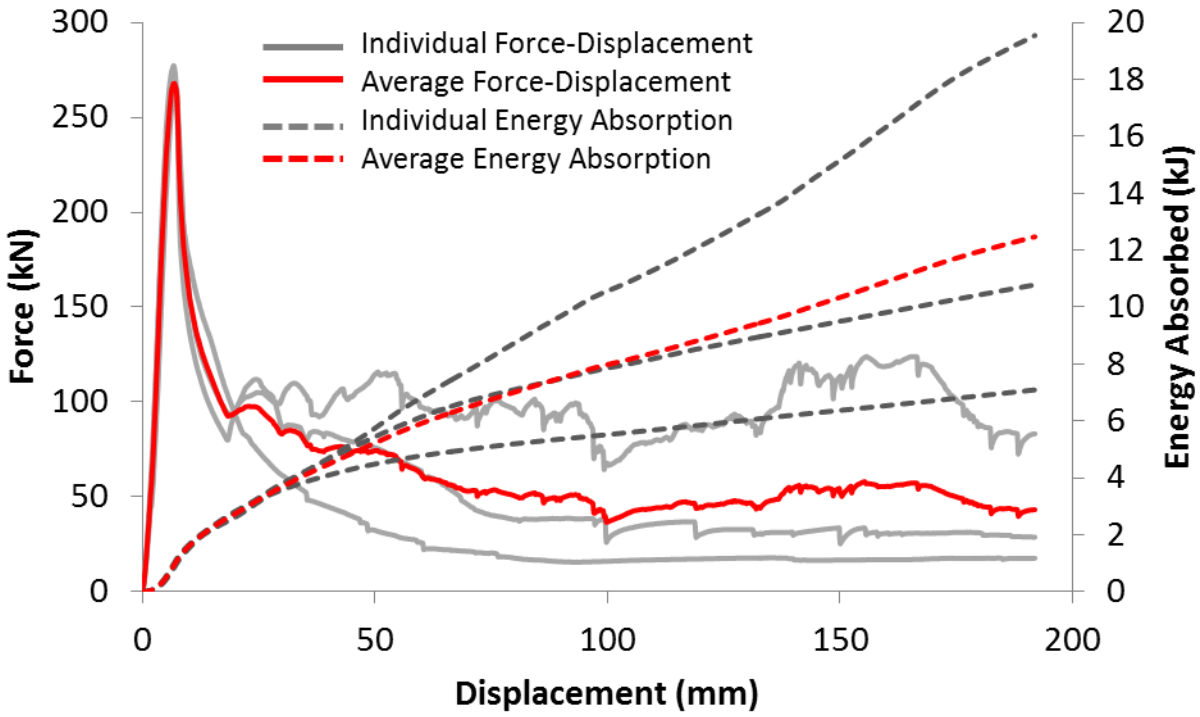

Figure 71. Force-displacement and energy absorption data for the *fully cooled* specimens

These results further validate the observations made in the dynamic sled tests. The variability in energy absorption, crack initiation and deformation modes is not a desirable property in automotive components. This means that the *fully cooled* configuration is not a very favourable one, despite the high micro-hardness values exhibited by these parts.

5.2.3 Quasi-Static Crush Response of the *Single Soft Zone 400˚C* Specimens

The progression of deformation during a *single soft zone 400˚C* quasi-static test is shown in Figure 72. The final deformed shapes of both crushed specimens are shown in Figure 73. The images in Figure 72 show that the *single soft zone 400˚C* specimens experienced buckling after the formation of the first fold. The buckling was caused by misalignment resulting from asymmetrical fold initiation.

As shown in Figure 73, both crushed specimens experienced some cracking in their soft zones. The force-displacement and energy absorption curves for these specimens are shown in Figure 74. The force and energy curves for the *single soft zone 400˚C* specimens were definitely more

repeatable than the *fully cooled* specimens. The average standard deviation between the two individual curves was 6.5%.

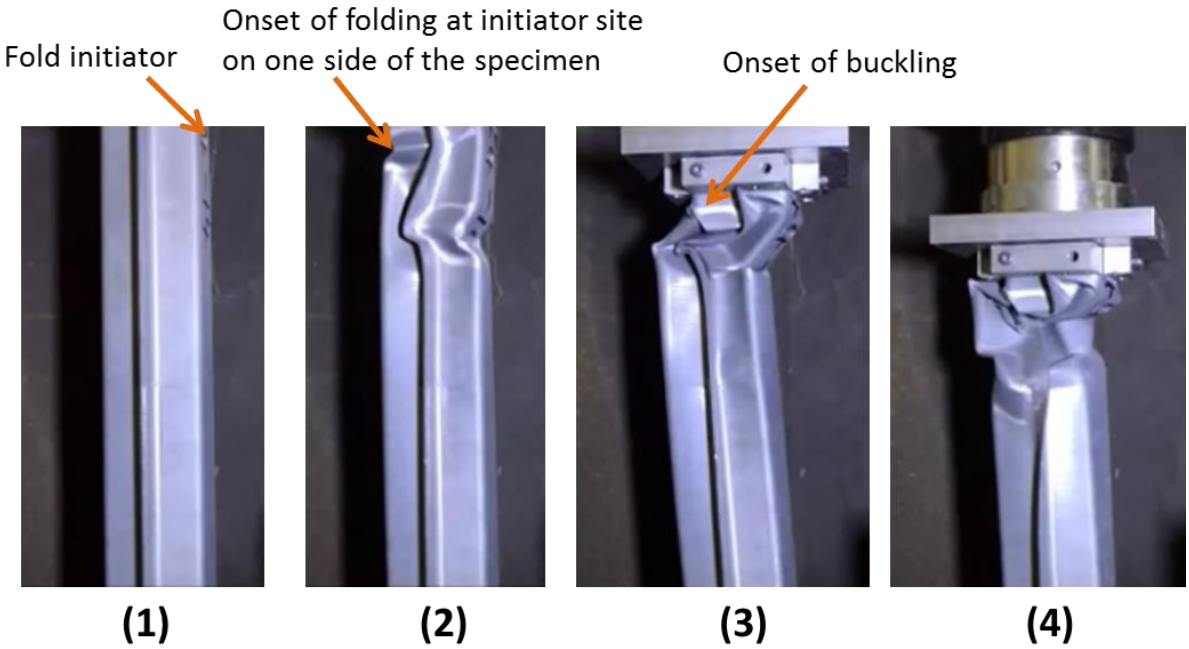

Figure 72. Deformation of a *single soft zone 400˚C* specimen during a quasi-static test

Figure 73. Final deformed shapes of the two crushed *single soft zone 400˚C* specimens. Locations of cracking are outlined in red

Just as with the *fully cooled* crush rail configuration, the trends observed in the quasi-static *single soft zone 400˚C* experiments are consistent with those observed in the dynamic sled experiments. The small amounts of cracking in the soft zone of the specimens and the tendency to buckle were observed in both the dynamic and quasi-static experiments.

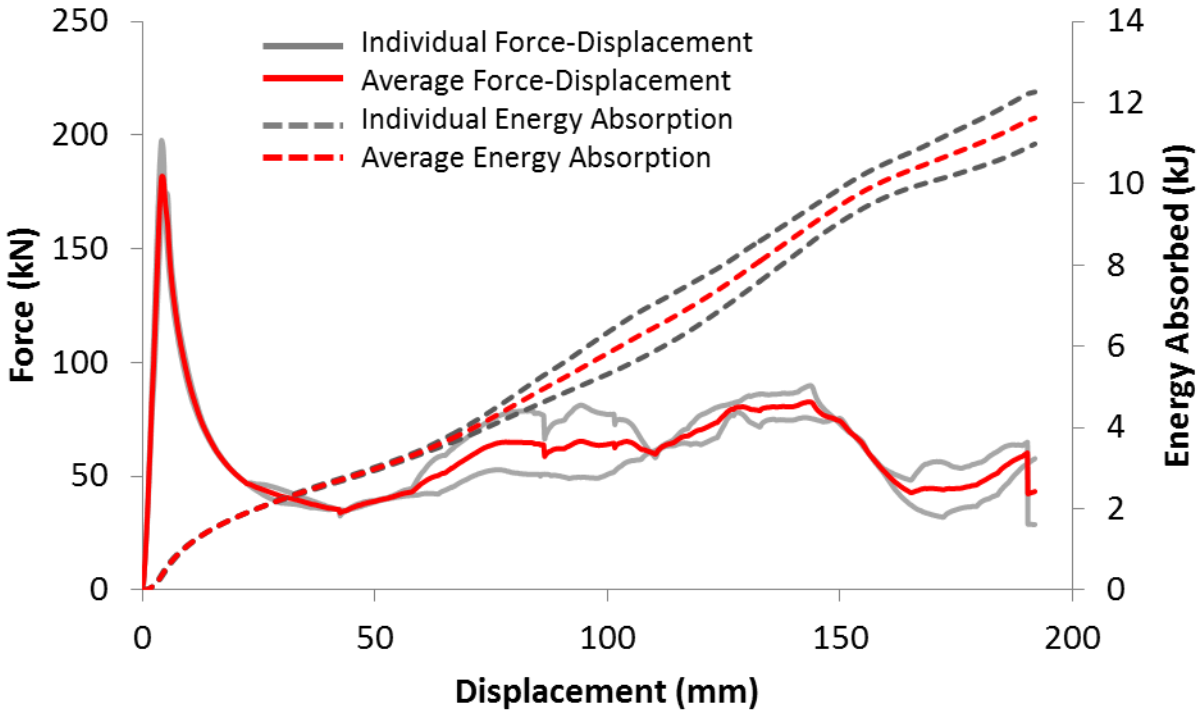

Figure 74. Force-displacement and energy absorption data for the *single soft zone 400˚C* specimens

5.2.4 Quasi-Static Crush Response of the *Single Soft Zone 700˚C* Specimens

The *single soft zone 700˚C* specimens exhibited a very unique response in the quasi-static experiments. In all three specimens that were crushed, deformation began at the transition zone instead of the site of the fold initiator.

Figure 75 shows the deformation in two of the crushed specimens: one specimen that entirely buckled and another specimen that folded then buckled. Figure 76 shows the final deformed shapes of all three crushed specimens. The specimens on the centre and right in Figure 76 correspond to the first and second specimens in Figure 75, respectively.

The first specimen in Figure 75, which is not shown in Figure 76, experienced no buckling, and deformed only via folding. However, instead of starting at the fold initiator and going down, the folding behavior actually began at the transition zone in this specimen as well. The folding subsequently travelled upwards.

The force-displacement and energy absorption curves for these specimens are shown in Figure 77. As evidenced in Figure 77, two of the three specimens exhibited very similar force and energy absorption responses. These two specimens are pictured on the left and right in Figure 76. The slight buckling experienced by the specimen on the right in Figure 76 did not seem to have significantly reduced its energy absorption.

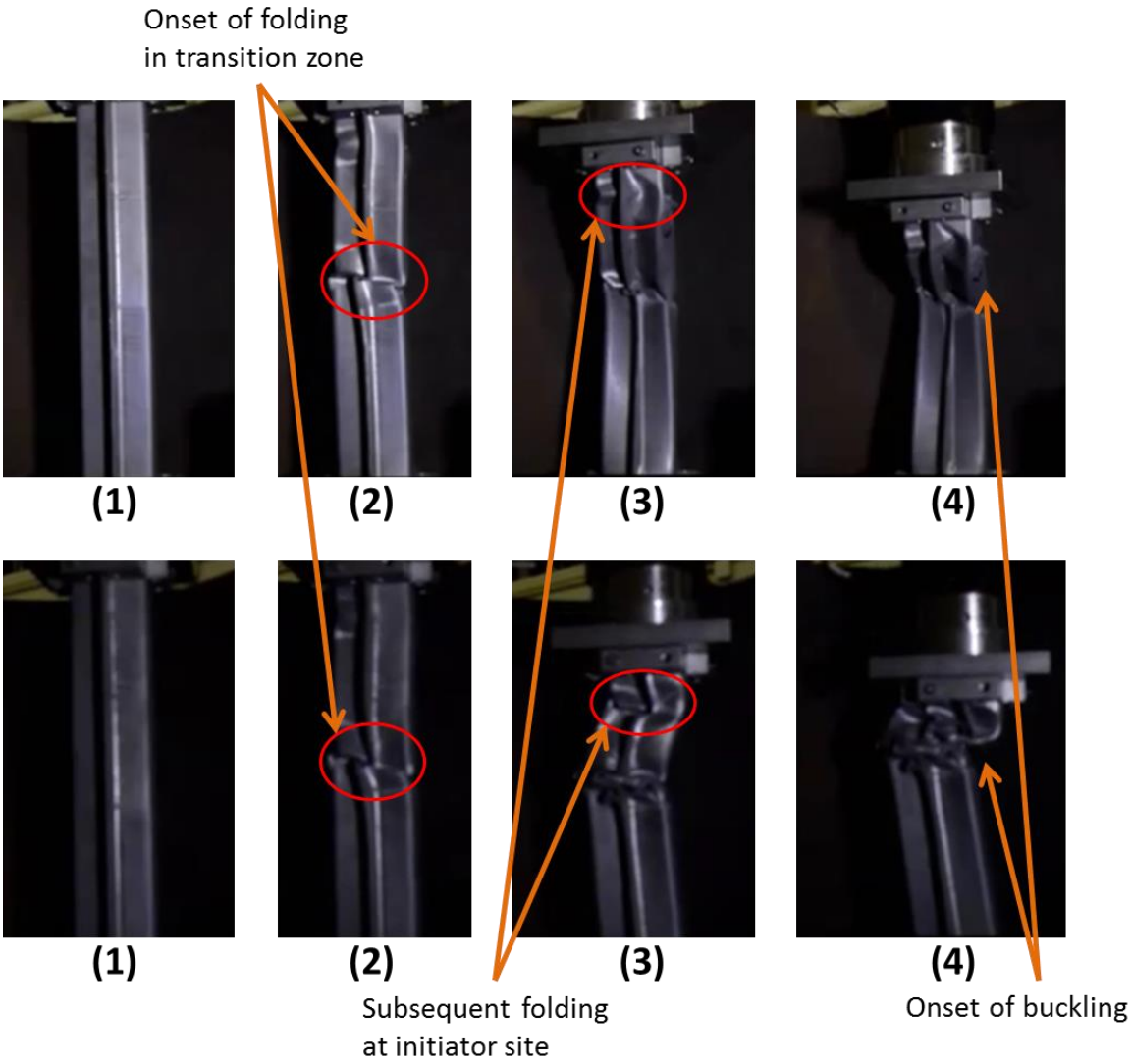

Figure 75. Deformation of two *single soft zone 700˚C* specimens during quasi-static tests

Figure 76. Final deformed shapes of the three crushed *single soft zone 700˚C* specimens

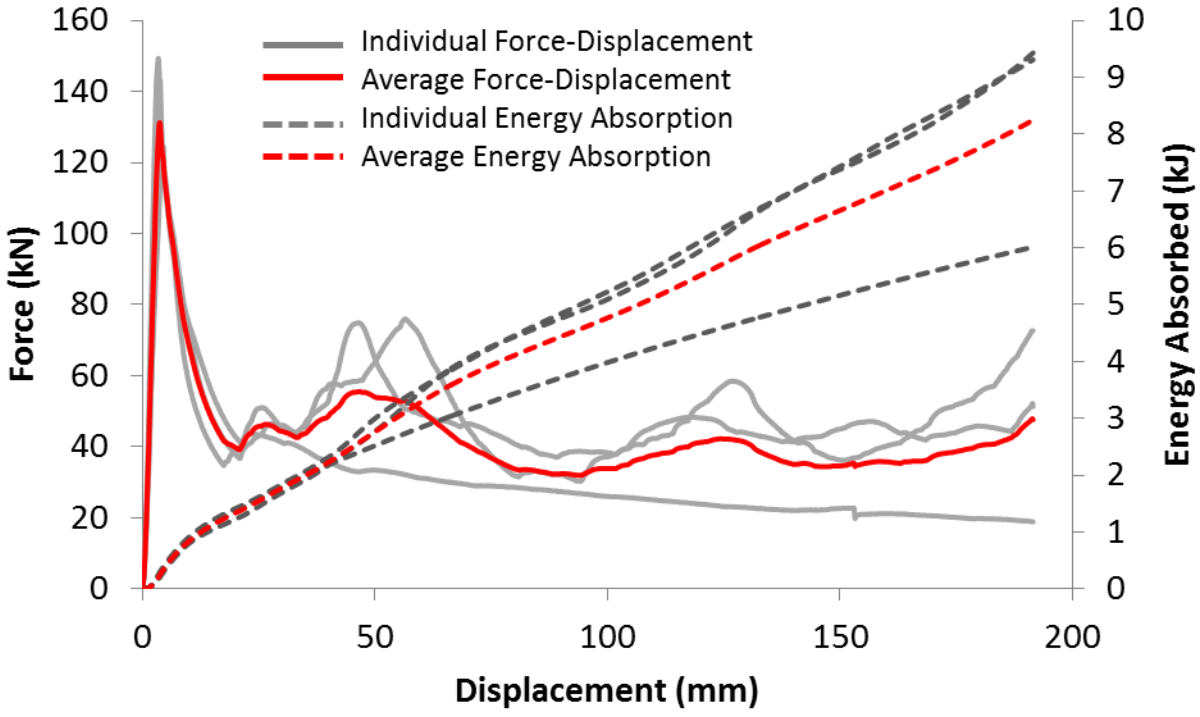

Figure 77. Force-displacement and energy absorption data for the *single soft zone 700˚C* specimens

In general, two of the three *single soft zone 700˚C* specimens displayed excellent repeatability in energy response and showed no visible signs of failure. However, the steep gradient in the top section of these specimens caused problems in the quasi-static experiments, just as it did in the dynamic sled experiments. These specimens also had the lowest quasi-static energy absorption among the four configurations that were tested.

5.2.5 Quasi-Static Crush Response of the *Graded Soft Zone* Specimens

Images showing the deformation pattern of two *graded soft zone* specimens are displayed in Figure 78. The final deformed shapes of the three crushed specimens are shown in Figure 79. The first and second specimens shown in Figure 78 correspond to the specimens on the left and centre in Figure 79, respectively.

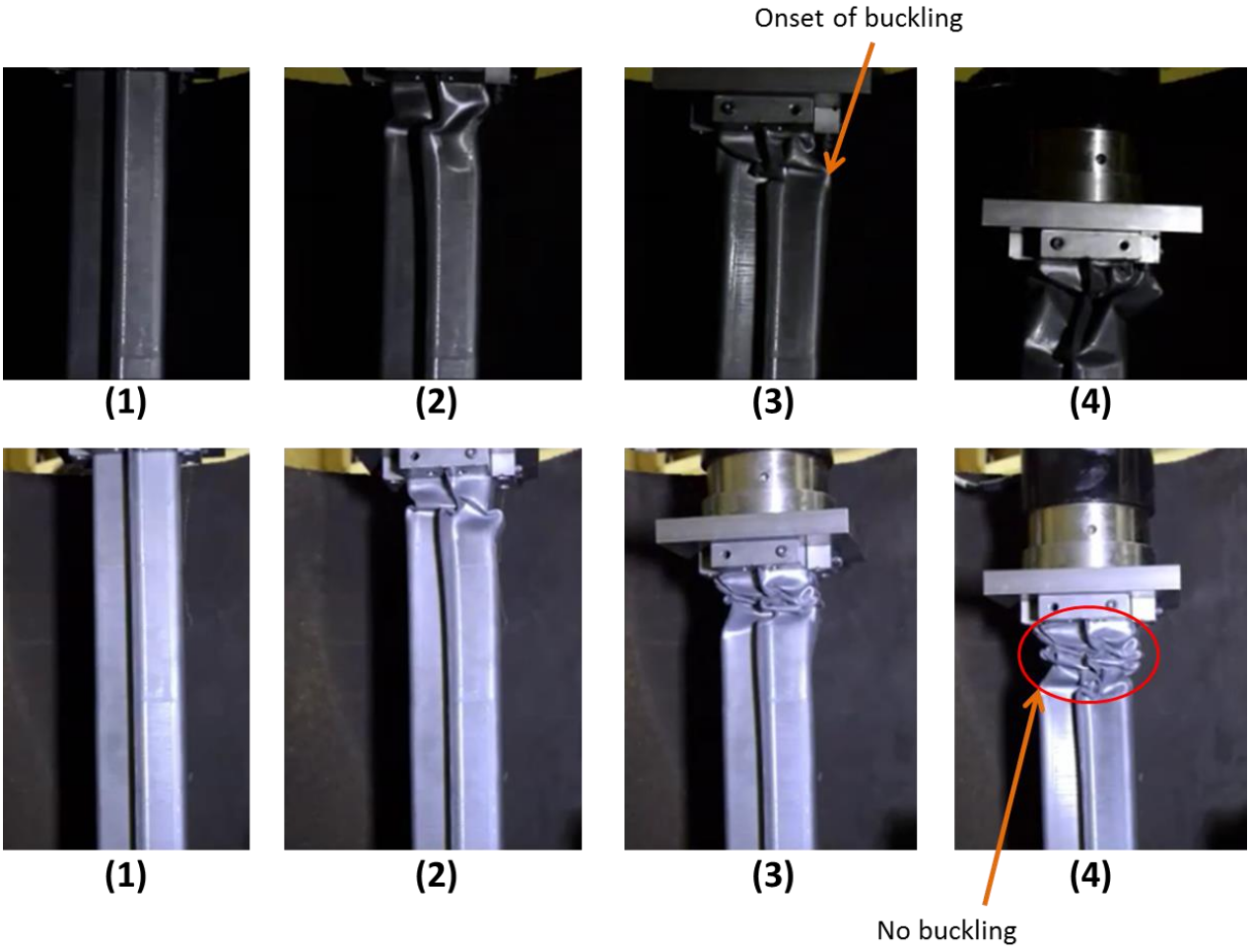

Figure 78. Deformation of two *graded soft zone* specimens during quasi-static tests

Figure 79. Final deformed shapes of the three crushed *graded soft zone* specimens. Locations of cracking are outlined in red.

As evidenced in both Figure 78 and Figure 79, one *graded soft zone* specimen experienced buckling during the quasi-static experiments. The remaining two specimens folded in their axial direction. The one specimen that did buckle also experienced some failure in its second soft zone (i.e., the zone formed at 400˚C).

The force-displacement and energy absorption curves for the *graded soft zone* specimens are shown in Figure 80. Overall, the energy absorption curves for these specimens were not as repeatable as they were in the dynamic sled experiments. The three curves are almost identical for the first 65 mm of crush. The curve corresponding to the specimen that buckled diverged after this point. The two remaining curves remained very consistent until a displacement of 140 mm after which the rate of increase of one curve decreased.

The fact that these specimens were the least susceptible to buckling is likely what gave them the second highest overall energy absorption (as discussed in section 5.2.1) among the four configurations of parts that were quasi-statically crushed. When experiencing deformation via a

pure folding mechanism, these specimens were also found to be very unlikely to crack. These observations are consistent with those determined from the dynamic sled experiments on the *graded soft zone* specimens.

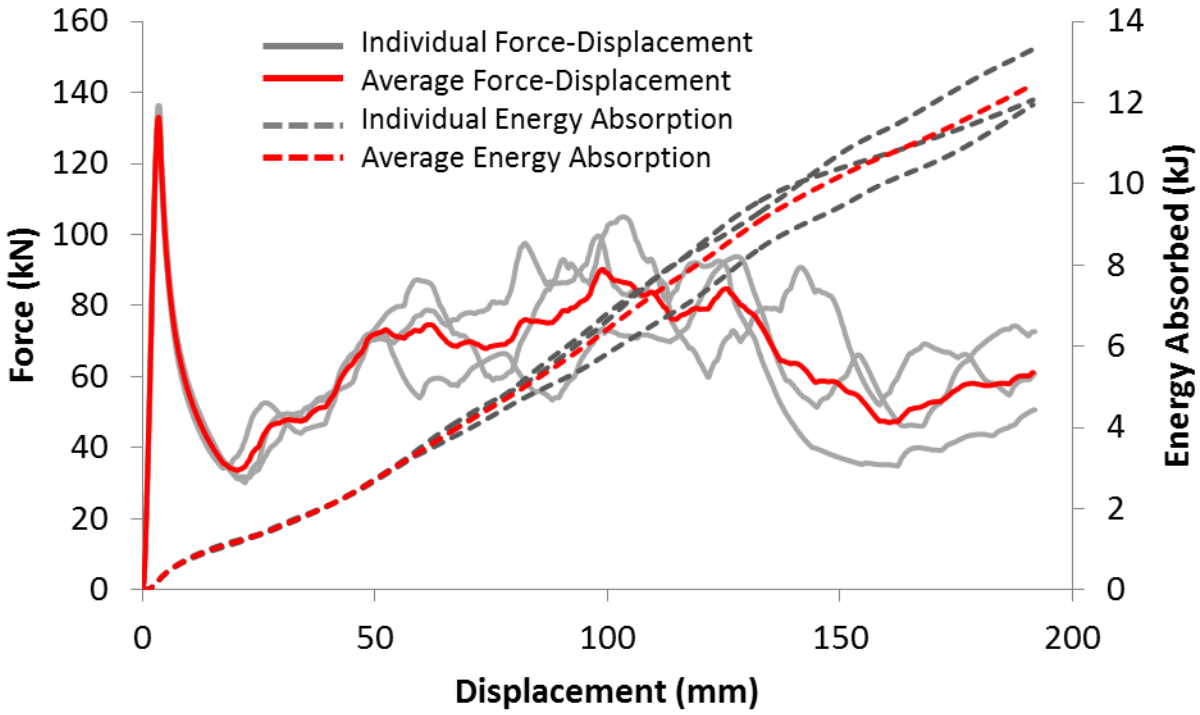

Figure 80. Force-displacement and energy absorption data for the *graded soft zone* specimens

5.3 Dynamic vs. Quasi-Static Crush Experiments: Comparison

The average energy absorption curves from both the dynamic and quasi-static experiments for all four configurations are shown in Figure 81. The solid lines represent the dynamic sled results while the dashed lines represent the quasi-static results.

All four crush rail configurations absorbed a higher amount of energy in the dynamic sled experiments than in the quasi-static experiments. Two main factors contributed to this phenomenon. First, the buckling was a more prevalent mode of failure in the quasi-static experiments than in the dynamic sled experiments. This likely reduced energy absorption in the specimens.

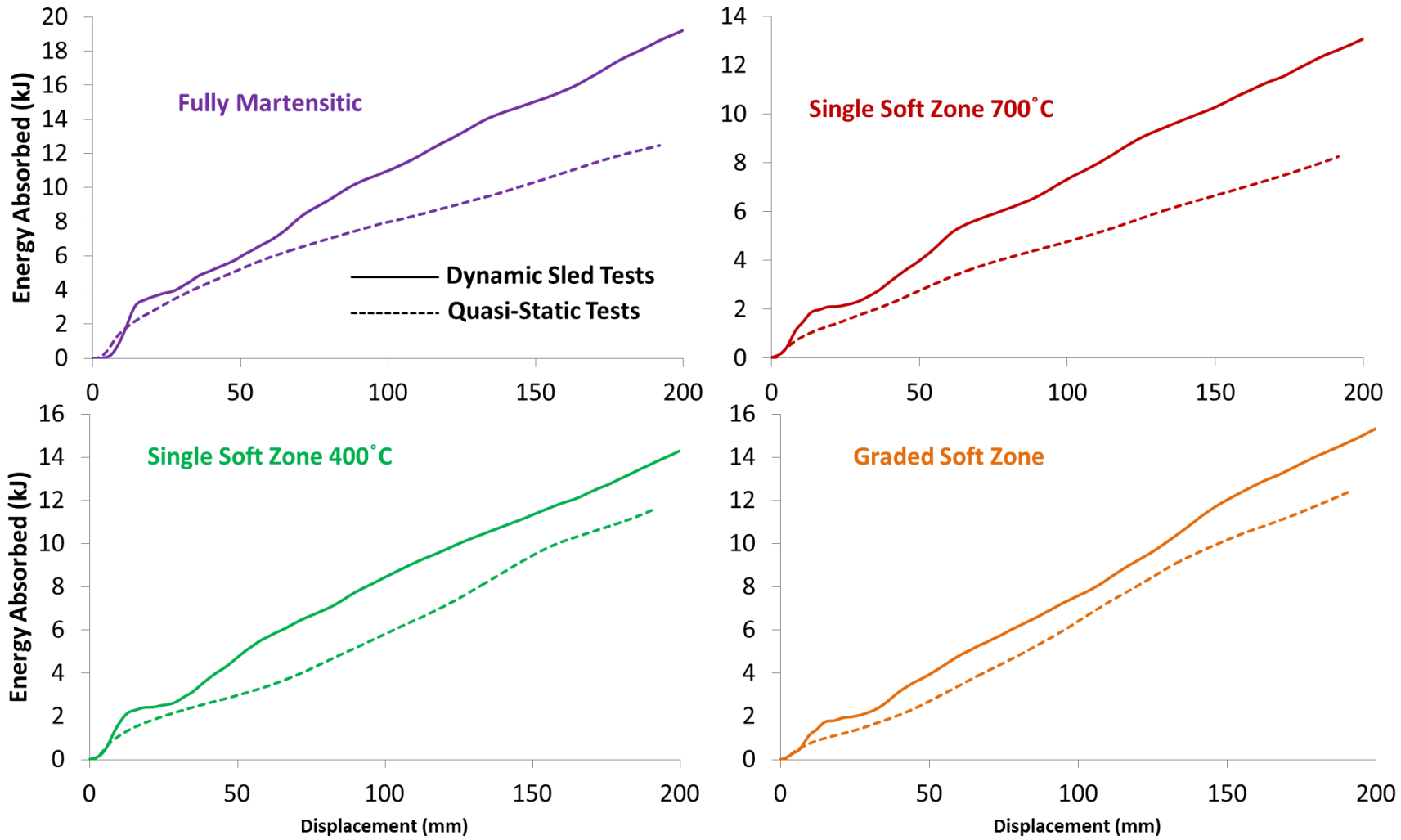

Figure 81. Comparison chart between the dynamic vs. quasi-static energy absorption curves for each configuration

Secondly, the higher energy absorption observed in the dynamic sled experiments may have be attributed to the positive strain rate sensitivity of as-formed Usibor® 1500P, as characterized by Bardelcik et al. [78]. Bardelcik et al. observed that between strain rates of $0.003s^{-1}$ and $960s^{-1}$, the true stress in a material increased by approximately 12% at an effective plastic strain of 20%. The higher stress observed at a higher strain rate by Bardelcik et al. is consistent with the results obtained in this work, where crush specimens exhibiting similar properties absorbed more energy dynamically than quasi-statically.

5.4 Dynamic Crush Models – Results and Comparison with Experiments

The energy absorption curves obtained from the dynamic crush models can be seen in Figure 82. For the purposes of comparison, the average energy absorption curves obtained from experiments are also shown. The numerical trends observed in the energy absorption were very similar to those observed experimentally. The *fully cooled* crush rail configuration demonstrated the highest energy absorption, followed by the *graded soft zone* configuration, then the *single soft zone 400˚C* configuration and finally the *single soft zone 700˚C* configuration.

The difference between the models and experiments for the *fully cooled* and *single soft zone 400˚C* specimens was very small (average percent difference was 7.0% and 6.3%, respectively). As explain in section 3.2.4, however, the crash models did not incorporate a failure criterion for the spotwelds. The lack of a spotweld failure criteria likely did not have consequences for the *single soft zone* and *graded soft zone* rails. The *fully cooled* crush, however, rails did experience significant spotweld failure in experiments. Therefore, the crash models for these types of parts were not complete.

Incorporating a failure would reduce the energy absorption curves for the *fully cooled* crush rail parts. The reduction would likely not be significant though, since the effect of tearing and rupturing in these specimens on the energy absorption curves is more extensive than the effect of spotweld failure.

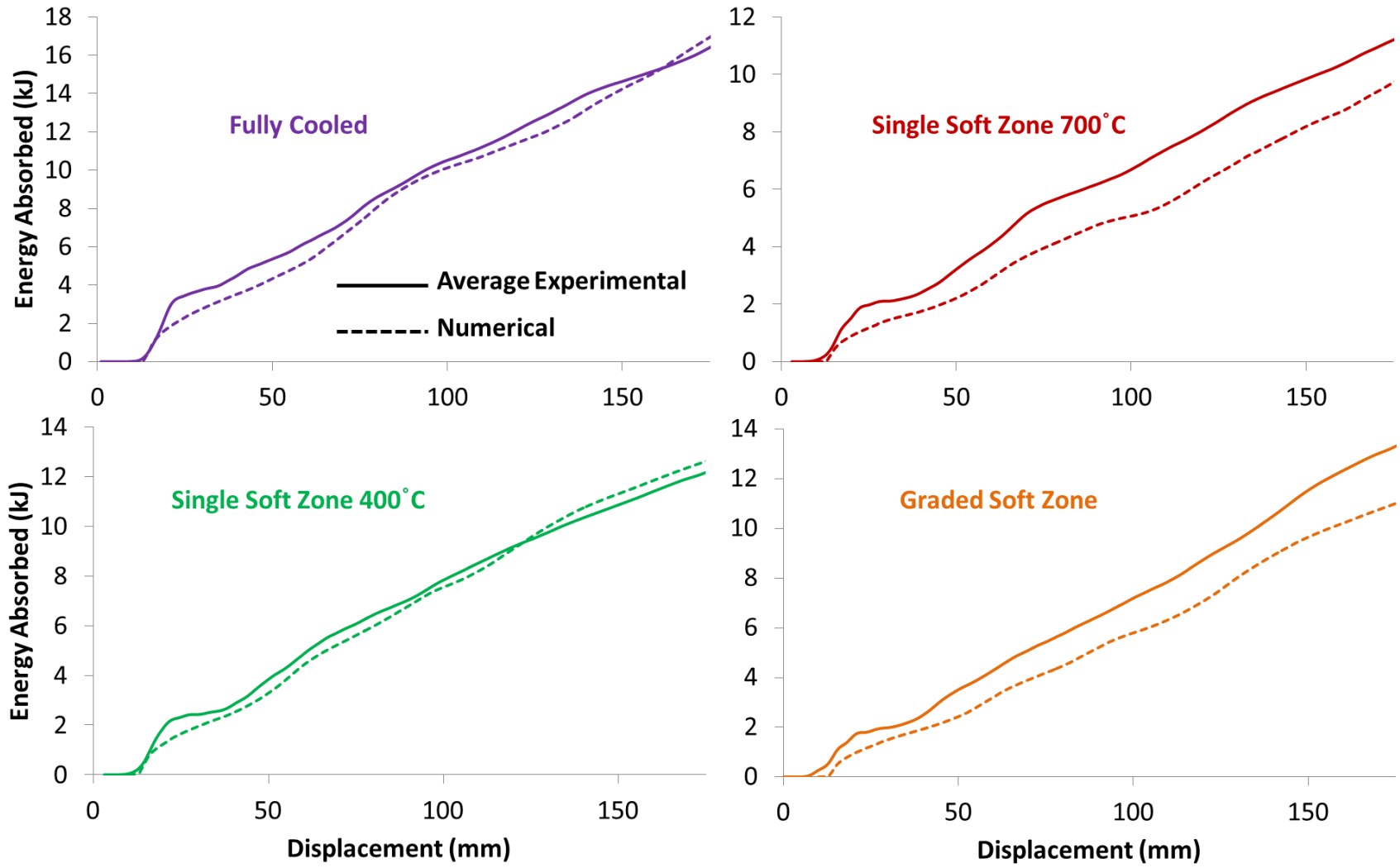

Figure 82. Comparison chart between the average experimental and numerical energy absorption curves for dynamic sled impact

The numerical prediction of the energy absorption was significantly lower than the observed experimental energy absorption for the *single soft zone 700˚C* and *graded soft zone* specimens (average percent difference was 20.7% and 18.0%, respectively). This can be explained by the large amounts of ferrite that the model has predicted for both types of parts that was not accounted for in the current version of the TCM constitutive model by Bardelcik et al. [68, 66].

The THS model predicted a phase composition containing nearly 80% ferrite (as shown in Figure 83) in many portions of the *single soft zone 700˚C* and *graded soft zone* parts. Neither the TCM nor TCM II models explained in section 1.5 were calibrated to account for such large amounts of ferrite and for such low values of micro-hardness. This meant that the flow stress curves obtained by the TCM constitutive description did not accurately reflect the stress-strain properties of these "softest" as-formed parts. This likely resulted in the higher error in predicted energy absorption in the crush rail configurations containing large amounts of ferrite. Nonetheless, the overall quantitative agreement between the model predictions of energy absorption with experiment is quite good.

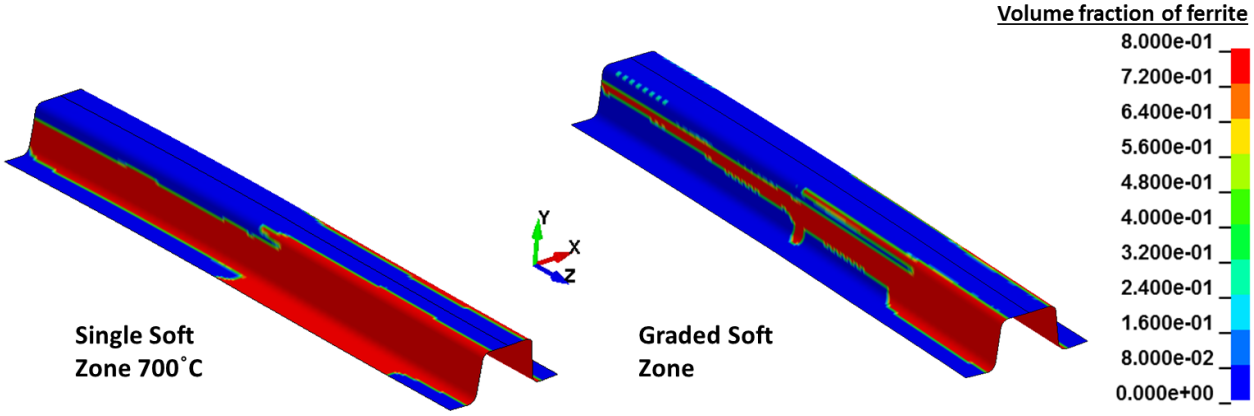

Figure 83. Volume fraction of ferrite predicted at the end of the THS model for the *single soft zone 700˚C* and *graded soft zone* parts

5.5 Quasi-Static Models – Results and Comparison with Experiments

The energy absorption curves obtained from the quasi-static models and experiments are shown in Figure 84. The numerical model for the *fully cooled* specimens predicted considerably higher energy absorption than what was observed in the quasi-static crush experiments. This was most likely caused by the buckling experienced by the *fully cooled* specimens during the quasi-static

experiments that the model was not able to capture. In many cases, there was significant pull-out of the quasi-static samples from the mounting bosses during buckling (section 5.2), whereas the model only considered a rigid mounting condition.

The energy absorption curves from the quasi-static models for the *single soft zone* specimens had good agreement with the average experimental curves. The good agreement between the experimental and numerical quasi-static energy absorption curves is consistent with that observed in the corresponding dynamic experiments and models.

For the *graded soft zone* crush rail configuration, the quasi-static model accurately predicted the energy absorption for the first 100 mm of the total stroke. For the remainder of the stroke, the model under-predicted the energy absorption.

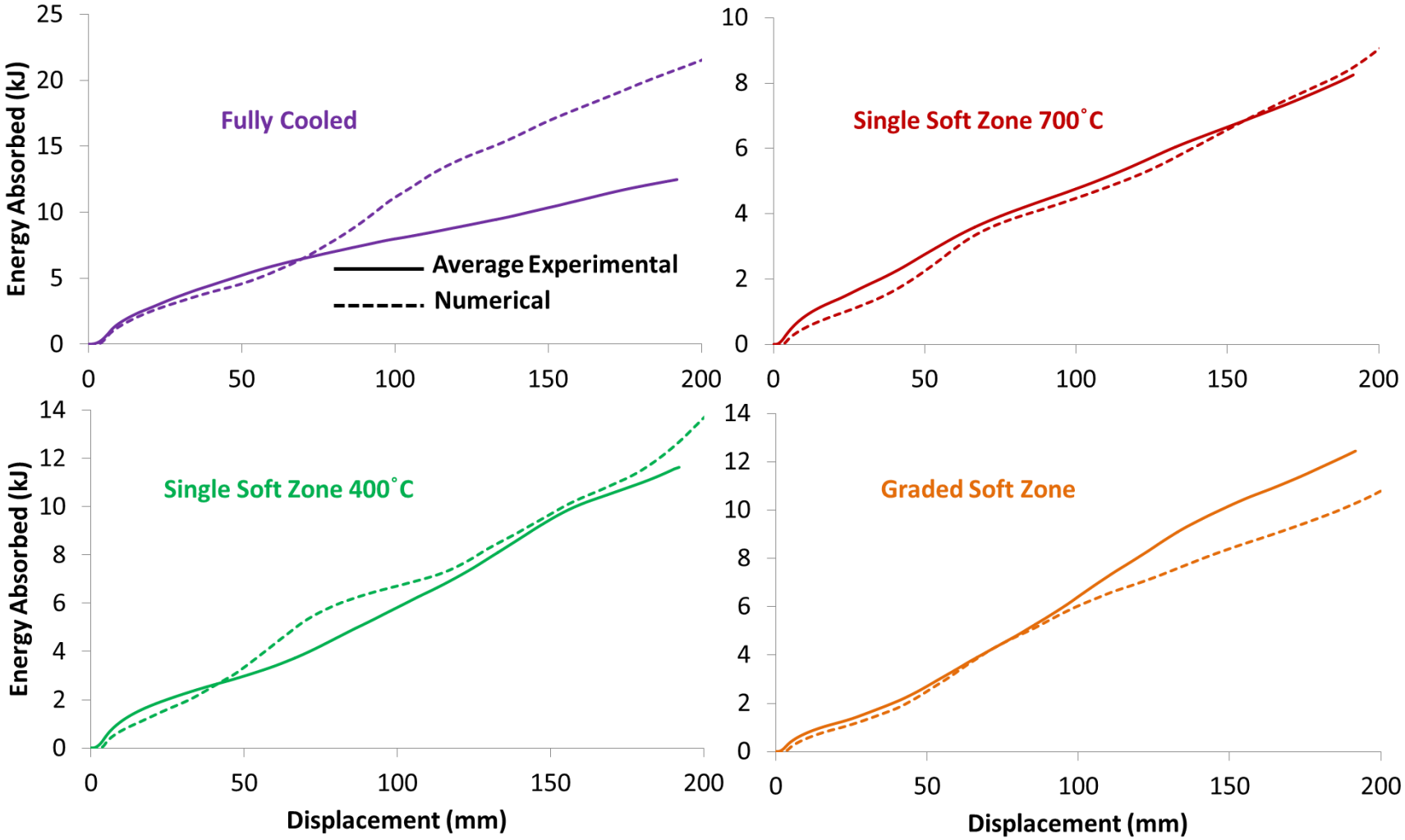

Figure 84. Comparison chart between the average experimental and numerical energy absorption curves for quasi-static crush

6. Conclusions and Recommendations

6.1 Conclusions

The THS process can produce hot stamped components with multiple zones of hardness (i.e., tailoring) without the need to post-temper the material. The ability to attain a tailored part without the need to post-temper offers tremendous potential benefits in terms of the total time it takes to produce a tailored part. The THS process also does not require any pre-processing of the material, as is needed in the tailor-welded technique.

The fact that the THS process can form and temper the properties of a part simultaneously offers several advantages in terms of cost and total turnaround time. Because of these advantages, the THS process can potentially be utilized in several applications, in addition to axial crush, which was the focus of this work.

The use of heater cartridges to elevate die temperature within various regions of the THS tooling is an effective method to locally control final part hardness. Overall, this work has shown that the THS technique can be used to produce axial crush members that contain tailored properties along their lengths. Hot stamped components formed in contact with a room temperature tooling surface exhibit a Vickers hardness of ~475 HV. Parts using a 400˚C tool exhibit ~280 HV, while hot stamping with a 700˚C tool temperature results in a local hardness of ~215 HV.

The numerical prediction of the Vickers hardness, using the Åkerström material model, was very accurate for zones that were formed at room temperature and those formed at 400˚C. However, there were discrepancies (approximately 15% difference) between the predicted and measured values of Vickers hardness in zones formed with a tool temperature of 700˚C. This discrepancy can be attributed to the current implementation of the Åkerström model within LS-Dyna. The current implementation does not have an option to enter a hardness vs. temperature curve for ferrite, like it does for martensite and bainite.

Likewise, the current TCM I and TCM II material models due to Bardelcik et al. [68, 66] not calibrated for tailored components resulting from slow cooling rates with high ferrite levels. As

such, the predicted energy absorption was roughly 15% below that measured for the *single soft zone 700˚C* and *graded soft zone* parts.

Based on the crash experimental results, it can be concluded that tailoring the hardness profile of an axial crush member offers several advantages compared to non-tailored, *fully cooled* specimens. While the *fully cooled* specimens exhibited the highest average energy absorption, they experienced extensive amounts of failure and crack propagation. This crack propagation led to unpredictable and highly-variant force-displacement and energy absorption characteristics, none of which are desirable.

In contrast to the fully martensitic components, all of the tailored parts displayed better repeatability in their crash responses. Between the three tailored categories of parts that were tested in this work, the *graded soft zone* parts displayed the best crash performance. They were found to have the highest energy absorption of the tailored components as shown in Figure 55, and the most consistent behavior as well, as shown in Figure 67. The energy absorption of the *graded soft zone* was almost equal to or slightly higher than the *fully cooled* specimens.

Another advantage offered by the *graded soft zone* parts was that they were the least prone to buckling in both the dynamic and quasi-static tests.

6.2 Recommendations

The Åkerström model as well as the TCM and TCM II models should be calibrated to more accurately predict the Vickers hardness and flow stress properties of parts that exhibit values of Vickers hardness less than 240 HV.

The shimming method used for the partitioned tooling for the *graded soft zone* parts should be modified to ensure consistent contact within the work piece along the full length of the component. It would also be beneficial to have this same accommodation for the side-walls in each zone, instead of just the top section.

A thermal imaging camera should be used to obtain the actual temperature distribution in the tooling. This would serve as a validation tool against the numerical models, in addition to the

micro-hardness and material thickness measurements that were conducted in this work. Metallurgical characterization of as-formed parts should be performed to determine their actual phase composition. The actual temperature in the blank when it enters the tooling should also be measured using thermocouples.

To improve on the crash models, a GISSMO failure surface where the failure strain curve is a function of micro-hardness should also be implemented. This would allow crack propagation in the *fully cooled* specimens to be more accurately predicted. It would also allow for the prediction of failure in the soft zones of the *single soft zone 400˚C* specimens.

An angled offset dynamic crash experiment, in which the crush specimen is impacted at a certain angle instead of axially, could also be employed to see if the tailored properties in an axial rail provide advantages in bending. This work is currently underway at Honda R&D Americas.

Finally, conducting a combined experimental/numerical study on the THS and crash of a real-world component would be beneficial. The components formed in this work contained very simple geometries, which served as a baseline in investigating and predicting crash behavior of THS components. After having conducted this study, the next logical step would to investigate a more complex part that more accurately represented a component in an automobile.

References

[1] A. Tekkaya and H. Karbasian, "A review on hot stamping," *Journal of Materials Processing Technology,* vol. 210, no. 15, pp. 2103-2118, 2010.

[2] K. Mori and Y. Okuda, "Tailor die quenching in hot stamping for producing ultra-high strength steel formed parts having strength distribution," *CIRP Annals - Manufacturing Technology,* vol. 59, no. 1, pp. 291-294, 2010.

[3] M. Maikranz-Valentin, U. Weidig, U. Schoof, H. Becker and K. Steinhoff, "Components with optimised properties due to advanced thermo-mechanical process strategies in hot sheet metal forming," *Steel Research International,* vol. 79, no. 2, pp. 92-97, 2008.

[4] P. Hein and J. Wilsius, "Status and innovation trends in hot stamping of USIBOR 1500P," *Steel Research International,* vol. 79, no. 2, pp. 85-91, 2008.

[5] M. Naderi, M. Ketabchi, M. Abbasi and W. Bleck, "Analysis of microstructure and mechanical properties of different high strength carbon steels after hot stamping," *Journal of Materials Processing Technology,* vol. 211, no. 6, pp. 1117-1125, 2011.

[6] M. A. Ahmetoglu, D. Brouwers, L. Shulkin, L. Taupin, G. Kinzel and T. Altan, "Deep drawing of round cups from tailor-welded blanks," *Journal of Material Processing Technology,* vol. 53, no. 3-4, pp. 684-694, 1995.

[7] W. Waddell, S. Jackson and E. Wallach, "The Influence of the Weld Structure on the Formability of Laser Welded Tailored Blanks," in *International Body Engineering Conference & Exposition*, Detroit, MI, USA, 1998.

[8] T. Meinders, A. van den berg and J. Huetink, "Deep drawing simulations of Tailored Blanks and experimental verification," *Journal of Materials Processing Technology 1,* vol. 103, no. 1, pp. 65-73, 2000.

[9] B. Kinsey, Z. Liu and J. Cao, "A novel forming technology for tailor-welded blanks," *Journal of Materials Processing Technology,* vol. 99, no. 1, pp. 145-153, 2000.

[10] T. Labudde and W. Bleck, "Formability characterisation of press hardened steels," in *Proceedings of hot sheet metal forming of high performance steel*, Luleå, Sweden, 2009.

[11] R. Kolleck, R. Veit, M. Merklein, J. Lechler and M. Geiger, "Investigation on induction heating for hot stamping of boron alloyed steels," *CIRP Annals - Manufacturing Technology,* vol. 58, no. 1, pp. 275-278, 2009.

[12] H. Liu, X. Jin, H. Dong and J. Shi, "Martensitic microstructural transformations from the hot stamping, quenching and partitioning process," *Materials Characterization,* vol. 62, no. 2, pp. 223-227, 2011.

[13] T. Stöhr, J. Lechler and M. Merklein, "Investigations on different strategies for influencing the microstructural properties with respect to partial hot stamping," in *2nd International Conference on Hot Sheet Metal Forming of HighPerformance Steel*, Luleå, Sweden, 2009.

[14] T. Svec and M. Merklein, "Tailored Tempering - Heat Transfer and Resulting Properties in Dependency of Tool Temperatures," in *3rd International Conference on Hot Sheet Metal Forming of HighPerformance Steel*, Kassel, Germany, 2011.

[15] R. Perez-Santiago, E. Billur, A. Ademaj, C. Sarmiento, R. Berlanga and T. Altan, "Hot Stamping of a B-Pillar with Tailored Properties: Experiments and Preliminary Simulation Results," in *4th International Conference on*

Hot Sheet Metal Forming of HighPerformance Steel, Lulea, Sweden, 2013.

[16] A. Erman Tekkaya, H. Karbasian, W. Homberg and K. Matthias, "Thermo-mechanical coupled simulation of hot stamping components for process design," *Production Engineering - Research and Development,* vol. 1, pp. 85-89, 2007.

[17] H. Hoffmann, H. So and H. Steinbeiss, "Design of Hot Stamping Tools with Cooling System," *Annals of the CIRP,* vol. 56, no. 1, pp. 269-272, 2007.

[18] K. Mori, S. Maki and Y. Tanaka, "Warm and Hot Stamping of Ultra High Tensile Strength Steel Sheets Using Resistance Heating," *CIRP Annals - Manufacturing Technology,* vol. 54, no. 1, pp. 209-212, 2007.

[19] R. Erhardt and J. Böke, "Industrial application of hot forming press simulation," in *1st International Conference on Hot Sheet Metal Forming of High-Performance*, Steel, Kassel, Germany, 2008.

[20] H. Choi, B. Kim, K. Nam, Y. Ha, S. Cha and C. Kang, "Development of Hot Stamped Center Pillar Using Form Die," *International Journal ofAutomotive Technology,* vol. 12, no. 6, pp. 887-894, 2011.

[21] A. Yanigada and A. Azishima, "Evaluation of coefficients of friction in hot stamping by hot flat drawing test," *CIRP Annals - Manufacturing Technology,* vol. 58, no. 1, pp. 247-250, 2009.

[22] Y. Dahan, Y. Chastel, P. Duroux, P. Hein, E. Massoni and J. Wilsius, "Formability Investigation for the Hot Stamping Process," in *International Deep Drawing Research Group (IDDRG)*, Porto, Portugal, 2006.

[23] P. Bariani, S. Bruschi, A. Ghiotti and A. Turetta, "Testing formability in the hot stamping of HSS," *CIRP Annals - Manufacturing Technology,* vol. 57, no. 1, pp. 265-268, 2008.

[24] K. Kusumi, N. Nomura, S. Yamamoto and M. Suehiro, "Draw-Bending Formability of Steel Sheets in Hot Stamping Process," in *3rd International Conference on Hot Sheet Metal Forming of HighPerformance Steel*, Kassel, Germany, 2011.

[25] M. Geiger, M. Merklein and J. Lechler, "Determination of tribological conditions within hot stamping," *Production Engineering*, vol. 2, no. 3, pp. 269-276, 2008.

[26] J. Banik, F. Lenze, S. Sikora and R. Laurenz, "Tailored Properties - A Pivotal Question for Hot Forming," in *3rd International Conference on Hot Sheet Metal Forming of HighPerformance Steel*, Kassel, Germany, 2011.

[27] J. Wilsius, B. Tavernier and D. Abou-Khalil, "Experimental and Numerical Investigation of Various Hot Stamped B-Pillar Concepts Based on Usibor 1500P," in *3rd International Conference on Hot Sheet Metal Forming of HighPerformance Steel*, Kassel, Germany, 2011.

[28] R. George, A. Bardelcik and M. Worswick, "Hot forming of boron steels using heated and cooled tooling for tailored properties," *J. Mat. Proc. Tech.*, vol. 212, no. 11, pp. 2386-2399, 2012.

[29] D. Berglund, K. Amundsson and L. Hellgren, "Hot Stamped Components with Soft Zones-Simulation and Validation of Material Properties and Product Performance," in *1st International Conference on Hot Sheet Metal Forming of HighPerformance Steel*, Kassel, Germany, 2008.

[30] T. Eller, L. Greve, M. Andres, M. Medricky, A. Hatscher, V. Meinders and A. van den Boogaard, "Plasticity and fracture modeling of quench-hardenable boron steel with tailored properties," *Journal of Materials Processing Technology,* vol. 214, no. 6, pp. 1211-1227, 2014.

[31] K. Omer, A. Bardelcik, R. George, D. Detwiler, N. Adam and M. Worswick, "Development of a Hot Stamped Axial Crush Member with Tailored Properties," in *IDDRG 2014 - Conference Proceedings*, Paris, France,

2014.

[32] Y. Prajogo, K. Omer, A. Bardelcik, R. George, M. Worswick, N. Adam and D. Detwiler, "Development of a Hot Stamped Side Impact Beam and Axial Crush Member with Tailored Properties – Numerical Models," in *4th International Conference on Hot Sheet Metal Forming of High-Performance Steel*, Luleå, Sweden, 2013.

[33] K. Sato, T. Inazumi, A. Yoshitake and S. Liu, "Effect of material properties of advanced high strength steels on bending crash performance of hat-shaped structure," *Int. J. Imp. Eng.*, vol. 54, no. 1, pp. 1-10, 2013.

[34] B. Macek, "Optimization Side Crash Performance Using a Hot-Stamped B-Pillar," 8 March 2006. [Online]. Available: http://www.sasft.org/~/media/Files/Autosteel/Great%20Designs%20in%20Steel/GDIS%202006/15%20-%20Optimization%20Side%20Crash%20Performance%20Using%20a%20Hot-Stamped%20B-Pillar.pdf. [Accessed 15 April 2014].

[35] A. Bardelcik, K. Ghavam, G. George and M. J. Worswick, "An Impact Model of a Hot Stamped Lab-Scale B-Pillar with Tailored Properties," in *3rd International Conference on Hot Sheet Metal Forming of HighPerformance Steel*, Kassel, Germany, 2011.

[36] D. Múnera, L. Lacassin and F. Pinard, "Very and Ultra High Strength Steels based Tailored Blanks: a step further towards vehicle crash performances improvement," *Revue de Métallurgie*, vol. 104, no. 12, pp. 613-624, 2007.

[37] M. Tan and N. Sharifan, "Adhesively Bonded Steel Structures," *Masters Thesis*, vol. Chalmers University of Technology, 2011.

[38] N. Ma, P. Hu and Z. Zhang, "Research on Tailored Microstructure Meterial in Hot Forming and its Application," in *3rd International Conference on Hot Sheet Metal Forming of High-Performance Steel*, Kassel, Germany, 2011.

[39] V. Tarigopula, M. Langseth, O. Hopperstad and A. Clausen, "Axial crushing of thin-walled high-strength steel sections," *Int. J. Imp. Eng.*, vol. 32, no. 5, pp. 847-882, 2006.

[40] P. Hosseini-Tehrani and E. Asadi, "Effects of new materials on the crashworthiness of S-rails," *J. Material: Design and Applications*, vol. 222, no. 1, pp. 37-43, 2008.

[41] O. Portillo and R. Eduardo, "Impact Performance of Advanced High Strength Steel Thin-Walled Columns," in *Proceedings of the World Congress on Engineering*, London, U.K., 2008.

[42] H. Sun, P. Hu, N. Ma, G. Shen, B. Liu and D. Zhou, "Application of Hot Forming High Strength Steel Parts on Car Body in Side Impact," *Chinese Journal of Mechanical Engineering*, vol. 23, pp. 1-6, 2010.

[43] A. Tekkaya, H. Karbasian, W. Homberg and M. Kleiner, "Thermo-mechanical coupled simulation of hot stamping components for process design," *Production Engineering*, vol. 1, no. 1, pp. 85-89, 2007.

[44] K. Kassem-Manthey, H. Speiss and K. Wolf, "A new approach for a coupled thermal-mechanical simulation of hot stamping process," in *1st International Conference on Hot Sheet Metal Forming of High-Performance Steel*, Kassel, Germany, 2008.

[45] H. Bok, M. Lee, E. Pavlina, F. Barlat and H. Kim, "Comparative study of the prediction of microstructure and mechanical properties for a hot-stamped B-pillar reinforcing part," *Int. J. Mat. Sci.*, vol. 53, no. 9, pp. 744-752, 2011.

[46] P. Åkerström and M. Oldenburg, "Austenite Decomposition During Press Hardening of a Boron Steel - Computer Simulation and Test," *J. Mat. Proc. Tech.,* vol. 174, pp. 399-406, 2006.

[47] A. Shapiro, "Using LS-DYNA to model hot sheet metal stamping," in *1st International Conference on Hot Sheet Metal Forming of High-Performance Steel*, Kassel, Germany, 2008.

[48] M. Oldenburg and G. Lindkvist, "Tool thermal cycle design for manufacturing of components with tailored material properties," in *3rd International Conference on Hot Sheet Metal Forming of High-Performance Steel*, Kassel, Germany, 2011.

[49] E. Caron, K. Daun and M. Wells, "Heat Transfer Coefficient Characterization during Hot Forming Die Quenching of Boron Steel Blanks," in *4th International Conference on Hot Sheet Metal Forming of HighPerformance Steel*, Luleå, Sweden, 2013.

[50] P. Salomonsson, M. Oldenburg, P. Akerstrom and G. Bergman, "Experimental and numerical evaluation of heat-transfer coefficient in press hardening," *Steel Research International,* vol. 80, no. 11, pp. 841-845, 2008.

[51] O. Salomonsson and M. Oldenburg, "Investigation of heat transfer in the press hardening process," in *2nd International Conference on Hot Sheet Metal Forming of High-Performance Steel*, Luleå, Sweden, 2009.

[52] E. Caron, K. Daun and M. Wells, "Experimental heat transfer coefficient measurements during hot forming die quenching of boron steel at high temperatures," *International Journal of Heat and Mass Transfer,* vol. 71, pp. 396-404, 2014.

[53] I. Shvets, "Contact Heat Transfer Between Plane Metal Surfaces," *Int. Chem. Eng.,* vol. 4, no. 4, p. 621, 1964.

[54] Li & Shellers, in *Proceedings of 2nd International Conference Modelling of Metal Rolling Processes*, London, U.K., 1996.

[55] M. Riera, M. Coussirat, A. Guardo, I. Valls and D. Casellas, "Simulation of hot stamping processes," in *1st International Conference on Hot Sheet Metal Forming of High-Performance Steel*, Kassel, Germany, 2008.

[56] P. Åkerström, "Modelling and Simulation of Hot Stamping," *Doctoral Thesis,* vol. Luleå University of Technology, 2006.

[57] P. Maynier, J. Dollet and P. Bastien, "Hardenability Concepts with Applications to Steels," New York City, AIME, 1978, pp. 518-544.

[58] P. Maynier, B. Jungmann and J. Dollet, Creusot-loire system for the prediction of the mechanical properties of low alloy steel products in: D.V. Doane and J.S. Kirkaldy, Hardenability Concepts with Applications to Steel, Warrendale, PA: AIME, 1978.

[59] H. Bhadeshia, Bainite in Steels, London, U.K.: The Institute of Materials, 1992.

[60] R. Honeycombe and H. Bhardeshia, Steels - Microstructure and Properties, Burlington, MA, U.S.A.: Edvard Arnold, 1981.

[61] T. Olsson, "An LS-DYNA Material Model for Simulations of Hot Stamping Processes of Ultra High Strength Steels," in *Proceedings of the 7th European LS-DYNA Conference*, Salzburg, Austria, 2009.

[62] P. Åkerström, G. Bergman and M. Oldenburg, "Numerical Implementation of a Constitutive Model for Simulation of Hot Stamping," *Modelling and Simulation in Materials Science and Engineering,* vol. 15, pp. 105-119, 2007.

[63] M. Li, D. Niebuhr, L. Meekisho and D. Atteridge, "A computational model for the prediction of steel hardenability," *Metallurgical and Materials Transactions,* vol. 29B, no. 3, pp. 661-672, 1998.

[64] Livermore Software Technology Corporation (LSTC), "LS-DYNA® KEYWORD USER'S MANUAL Volume II - Material Models," Livermore Software Technology Corporation (LSTC), 03/29/2014.

[65] B. Williams, "A Study of the Axial Crush Response of Hydroformed Aluminum Alloy Tubes (Ph.D Thesis)," University of Waterloo, Waterloo, 2007.

[66] A. Bardelcik, M. Worswick, S. Winkler and M. Wells, "Strain Rate Sensitive Constitutive Model for Quenched Boron Steel with Tailored Properties," *Int. J. Imp. Eng.,* vol. 50, pp. 49-62, 2012.

[67] E. Voce, *J. Inst. Met.,* vol. 74, pp. 537-562, 1948.

[68] A. Bardelcik, M. Worswick and M. Wells, "The influence of martensite, bainite and ferrite on the as-quenched constitutive response of simultaneously quenched and deformed boron steel – Experiments and model," *Materials and Design,* vol. 55, pp. 509-525, 2014.

[69] ZRCI Refractory Composites, "REFRACTORY BOARD TYPES ZIRCAL-18, ZIRCAL-45 AND ZIRCAL-95," July 2005. [Online]. Available: http://www.zrci.com/zrci301.pdf. [Accessed 24 June 2014].

[70] Plascore, "Plascore CrushLite," 2012. [Online]. Available: http://www.plascore.com/pdf/Plascore_CrushLite.pdf. [Accessed 27 June 2014].

[71] F. Beer, E. Johnstron, J. DeWolf and D. Mazurek, "Mechanics of Materials, 6th ed.," New York, N.Y., McGraw Hill, 2012, p. Appendix B.

[72] Y. Touloukian, Thermophysical Properties of Matter, IFI/Plenum, 1970.

[73] R. George, A. Bardelcik and M. Worswick, "Improving the Prediction of the Bainite and Ferrite Phase Transformation during Hot Stamping Simulations using LS-DYNA," in *Proceedings of hot sheet metal forming of high performance steel*, Luleå, Sweden, 2013.

[74] P. Maynier, B. Jungmann and J. Dollet, Creusot-loire system for the prediction of the mechanical properties of low alloy steel products in: D.V. Doane and J.S. Kirkaldy, Hardenability Concepts with Applications to Steel, Warrendale, PA: AIME, 1978.

[75] LSTC, Shapiro, A., *Private Correspondance via E-mail*, October 2013.

[76] R. George, "Hot Forming of Boron Steels with Tailored Mechanical Properties: Experiments and Numerical Simulations," in *Masters Thesis*, University of Waterloo, Waterloo, Canada, 2011.

[77] L. Ten Kortenaar, A. Bardelcik, M. Worswick and N. Detwiler, The Effects of Stress Triaxiality on the Failure Response of Boron Steel Quenched to a Martensitic and Bainitic Material Condition, Lulea, Sweden: Proceedings of the 4th Hot Sheet Metal Forming of High-Performance Steel, 2013.

[78] A. Bardelcik, C. Salisbury, S. Winkler, M. Wells and M. Worswick, "Effect of cooling rate on the high strain rate properties of boron steel," *Int. J. Impact Eng.,* vol. 37, no. 6, pp. 694-702, 2010.

[79] H. Bok, M. Lee, H. Kim and M. Moon, "Thermo-Mechanical Finite Element Analysis Incorporating the Temperature Dependent Stress-Strain Response of Low Alloy Steel for Practical Application to the Hot Stamped Part," *Met. Mater. Int.,* vol. 16, no. 2, pp. 185-195, 2010.

[80] H. Liu, Z. Xing, J. Bao and B. Song, "Investigation of the Hot-Stamping Process for Advanced High-Strength Steel Sheet by Numerical Simulation," *J. Mat. Eng. and Perf.*, vol. 19, no. 3, pp. 325-334, 2010.

[81] B. Zhu, Y. Zhang, J. Li, H. Wang and Z. Ye, "Simulation research of hot stamping and phase transition of automotive high strength steel," *Material Research Innovations*, vol. 15, no. 1, pp. S426-S430, 2011.

[82] Z. Xing, J. Bao and Y. Yang, "Numerical simulation of hot stamping of quenchable boron steel," *Materials Science and Engineering: A*, vol. 499, no. 1-2, pp. 28-31, 2009.

[83] I. Neubauer, K. Hübner and T. Wicke, "Thermo-mechanically coupled analysis: the next step in sheet metal forming simulation," in *1st International Conference on Hot Sheet Metal Forming of High-Performance Steel*, Kassel, Germany, 2008.

[84] S. Ertürk, M. Sester, M. Selig, P. Feuser and K. Roll, "A Thermo-Mechanical-Metallurgical FE Approach for Simulation of Tailored Tempering," in *3rd International Conference on Hot Sheet Metal Forming of High-Performance Steel*, Kassel, Germany, 2011.

[85] G. Camacho and M. Ortiz, "Adaptive lagrangian modelling of ballistic penetration of metallic targets," *Int. J. Comp. Meth. Appl. Mech. Eng.*, vol. 142, no. 3-4, pp. 269-301, 1997.

[86] M. Merklein and J. Lechler, "Investigation of the thermo-mechanical properties of hot stamping steels," *J. Mat. Proc. Tech.*, vol. 177, no. 1-3, pp. 452-455, 2006.